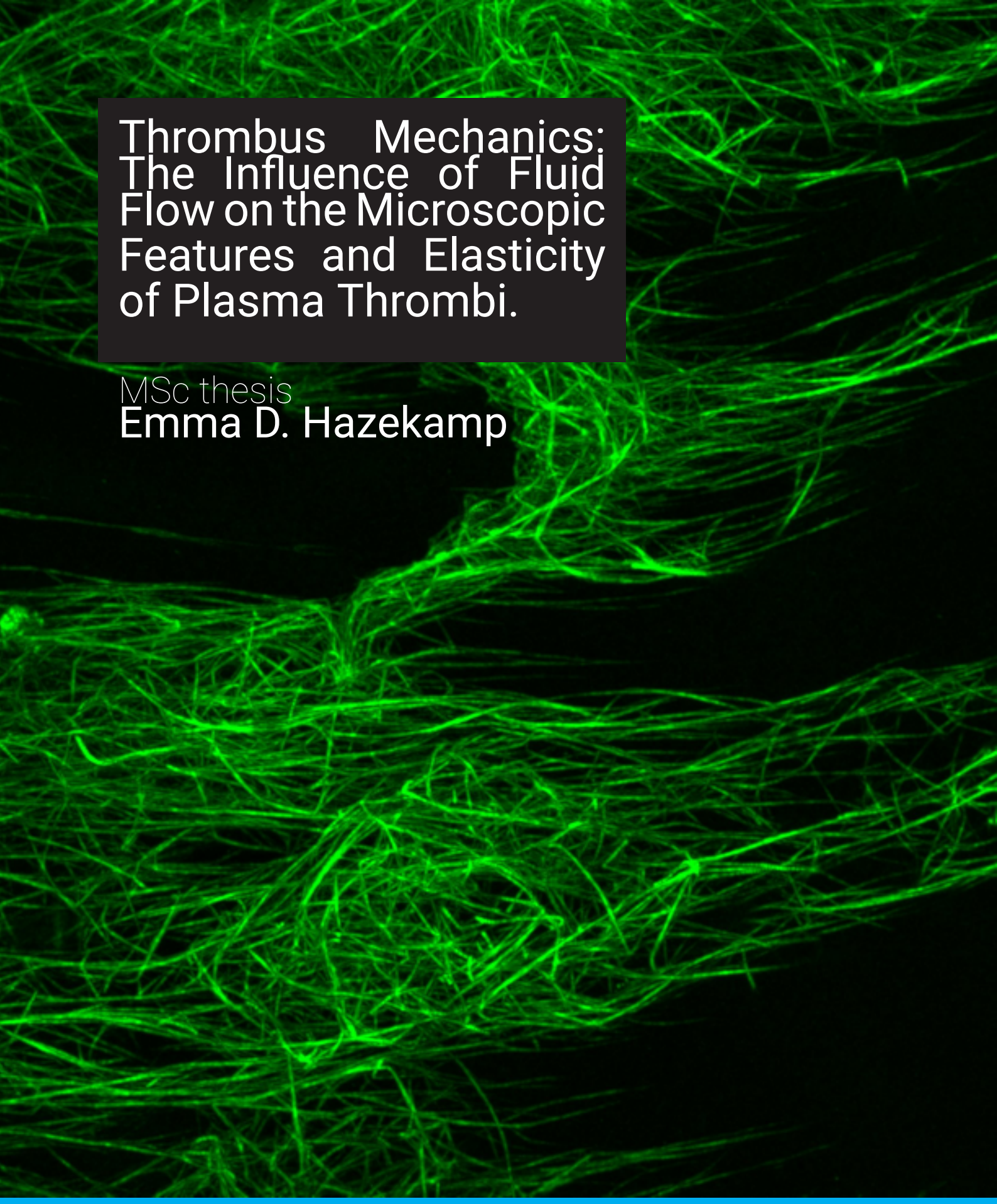

Thrombus Mechanics: The Influence of Fluid Flow on the Microscopic Features and Elasticity of Plasma Thrombi.

MSc thesis

Emma D. Hazekamp

TU Delft

Erasmus MC

Thrombus Mechanics: The Influence of Fluid Flow on the Microscopic Features and Elasticity of Plasma Thrombi.

by

Emma D. Hazekamp

to obtain the degree of Master of Science in Biomedical Engineering
at the Delft University of Technology, to be defended publicly on the 7, October, 2022 at 15:00.

Student number:	4629221	
Project duration:	January 3, 2022 – October 7, 2022	
Daily supervisors:	ir. J.M.H. Cruts	Erasmus MC
	ir. H. Eyisoylu	Erasmus MC
Supervisor:	dr. ir. F.J.H. Gijsen	TU Delft and Erasmus MC
Thesis committee:	dr. ir. F.J.H. Gijsen	TU Delft and Erasmus MC
	dr. M.J. Mirzaali	TU Delft

TU Delft

Erasmus MC

Acknowledgements

This master thesis report would not have been possible without the support of many people. Firstly, I would like to thank the Biomedical Engineering group of the Cardiology department at the Erasmus Medical Centre for their hospitality over the last few months. After a year of studying at home, it was a relief to be back in the lab, to be able to have small chats and discussions and to no longer have to work in the same room as where I sleep. Secondly, I would like to thank Janneke Cruts, who coached me during this project. You have given me valuable guidance in report writing and advised me on how to approach such a large research project. Thirdly, I would like to thank Hande Eyisoylu, who supported me with a lot of experimental work during the final stage of the thesis. Both of us working on the final experiments gave me immediate feedback as well as quick discussions during our time in the lab. Fourthly, I would like to thank Frank Gijsen, for really pushing me to ask the why question, but also for giving critical feedback on my methods and results.

Furthermore, I would like to thank Ryanne Arisz, Rachel Cahalane, Kim van Gaalen and Martijn de Gruiter for providing me with various tips and tricks during the experimental phase of my thesis. Additionally, my thanks go out to Geert Springeling who fabricated the tapered flow chamber and to Dustin Laur who helped immensely with SEM imaging.

Finally, a special thanks goes out to all the department's students, my parents, my brother and my boyfriend, who have supported me during the thesis.

Emma D. Hazekamp
Rotterdam, October 2022.

Abstract

Abstract- Perfusion impairment of vessels by thrombus formation is the top global cause of death. Depending on the location and disease pathology, thrombus composition varies, affecting treatment response and making identification of thrombus composition and its mechanical response sought after. The features of a fibrin network, which functions as the adhesive, have shown to influence thrombus strength, viscoelasticity, permeability and resilience to fibrinolysis. In previous studies, these features were analysed on fibrin gels made under static conditions, while in vivo thrombi are formed under flow. Therefore, the aim of this thesis is to form plasma thrombi in both the presence and absence of flow and evaluate the differences in the microstructure and mechanical properties.

Methods- Plasma thrombi in the presence and absence of flow were formed inside the Chandler loop. Recitrated platelet free plasma (PFP), pooled from three healthy volunteers, was to the Chandler loop tubings and spun at 0, 10 and 30 RPM to create shear rates of roughly 0 (static thrombus), 100 and 300 s^{-1} (flow thrombi). Six thrombi were formed for each shear rate, of which two were prepared for Scanning Electron Microscopy (SEM) imaging to determine the diameter of fibrin fibers. The other four thrombi were cut into three disks and were used for Confocal Laser Scanning Microscopy (CLSM), unconfined compression testing and micro-indentation. With CLSM, the fiber density and pore size of the network were quantified and with unconfined compression testing and micro-indentation the global and local stiffness' of the thrombi, respectively. The global stiffness of the thrombi was measured at low (20-40%) and high strains (75-80%).

Results- Increased diameters were found for flow thrombi compared to static thrombi ($p < 0.001$ and $p < 0.001$). Furthermore, density increased $p=0.017$ and $p=0.007$) and pore size decreased ($p < 0.001$ and $p < 0.001$) for flow thrombi compared to static thrombi. Compression testing showed an increased stiffness for thrombi formed at 30 RPM compared to 0 and 10 RPM (20-40%, $p = 0.008$ and $p < 0.001$; 75-80%, $p = 0.015$ and $p < 0.001$). Lastly, only at high strains a significant stiffness increase was found between the 0 and 10 RPM ($p=0.025$).

Conclusions- The fiber diameter increased in the presence of flow compared to thrombi formed in the absence of flow. Furthermore, the density increased and the pore size decreased for flow thrombi compared to static thrombi. Lastly, the stiffness of the plasma thrombi was increased for the thrombi formed at 30 RPM compared to 0 and 10 RPM.

Contents

List of abbreviations

A

ADP adenosine diphosphate.

C

CLSM Confocal Laser Scanning Microscopy.

E

ECM extra cellular matrix.

EDM Euclidean distance map.

F

FIB-SEM Focussed Ion Beam Scanning Electron Microscopy.

H

HDMS hexamethyldisilazane.

P

PFP platelet free plasma.

PRP platelet rich plasma.

PVC poly vinyl chloride.

R

RBCs red blood cells.

RPM revolutions per minute.

S

SEM Scanning Electron Microscopy.

T

TF Tissue factor.

TxA2 Thromboxane A2.

V

VWF Von Willebrand factor.

W

WB whole blood.

WBCs while blood cells.

1 Introduction

The top two global causes of death, as reported by the World Health Organisation, are ischaemic heart disease (or myocardial infarction) and stroke [1]. Both are caused by a thrombus or thromboembolism inside a blood vessel, which impedes the blood flow and therefore the oxygen supply [2]. Normally, the haemostasis process functions as a defensive reaction to prevent blood loss. It can be described in two steps: 1) the formation of a platelet plug (primary haemostasis) and 2) coagulation (secondary haemostasis) [3, 4]. Platelet plug formation is triggered when platelets are exposed to the extracellular matrix (ECM) of an injured vessel [5–7]. By binding to collagen or Von Willebrand factor (VWF) the platelets are activated, which causes them to swell, form spiked processes (lamellipodia) and release agonists like adenosine diphosphate (ADP), serotonin and Thromboxane A2 (TxA2) [4, 5, 8]. By releasing these agonists additional platelets are recruited and the platelet plug is formed [9, 10].

Coagulation (step 2) reinforces the platelet plug with fibrin fibers [3, 6]. The assembly of fibrin threads is a multistep process involving many procoagulants or clotting factors, called the coagulation cascade (Figure 1.1). It consists of the intrinsic and extrinsic pathway [8]. The former has all the components present inside the bloodstream, is slower and is triggered by platelet activation [3, 11]. The latter is faster and is triggered by an external factor, Tissue factor (TF), which is present in the sub-endothelial tissue (i.e. the extra cellular matrix) [4, 11, 12]. Both pathways converge at factor X, which complexes with calcium ions and factor V to form prothrombin activator [3, 12]. The prothrombin activator converts prothrombin into thrombin, which in turn will cleave fibrinogen into fibrin monomers that polymerize into fibrin and form fibrin threads [3, 4, 12, 13]. Then, Factor XIII, also known as fibrin stabilising factor, cross-links the fibrin strands to further stabilise the clot [3, 4, 12].

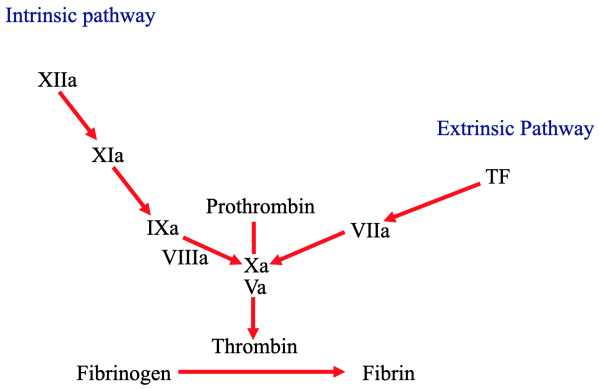

Figure 1.1: A simplified schematic of the coagulation cascade. It shows the intrinsic and the extrinsic pathway, which converges into the common pathway at factor X. Adopted from [14].

Though coagulation is an important aspect to prevent blood loss, anticoagulation is important to prevent undesirable thrombosis. To keep the clotting limited to the injured site and prevent clotting of the whole circulatory system inhibition processes are in place. Examples are the continuous flow of blood, the production of activation inhibitors for platelets and thrombin, the production of plasminogen activator by the injured

tissue and the tissue factor pathway inhibitor [4, 11]. Even though haemostasis is a strictly regulated process, undesirable thrombosis can happen. Three components critical to the development of thrombosis are described by Virchow's triad: hypercoagulability, stasis and endothelial injury [15, 16].

The three main components of thrombi are red blood cells (RBCs), platelets and fibrin [17]. Depending on the location and disease pathology of the thrombus, different trends in thrombus composition were observed [17, 18]. Thrombus formation can take place in both arteries and veins and is titled arterial thrombosis and venous thrombosis, respectively. Arterial thrombi, in for example myocardial infarction, have an outer layer consisting mainly of fibrin and platelets [18, 19]. This outer layer gives the thrombus a white appearance, though in the middle of the thrombus tightly packed polyhedral RBCs can be found [17, 19, 20]. Venous thrombi have little platelets and consist mainly of RBCs and fibrin, colouring them red [17, 19]. Though when large histology studies were done to evaluate compositional features of ischaemic stroke thrombi, the percentage of platelet-rich or RBC-rich area inside the retrieved thrombi varied considerably from person to person (Figure 1.2) [21, 22]. The compositional differences between thrombi affect the mechanical properties and thereby the success of thrombus removal [23]. As the heterogeneity between thrombi affects their response to treatment, identification of thrombus composition beforehand will improve thrombosis treatment [24].

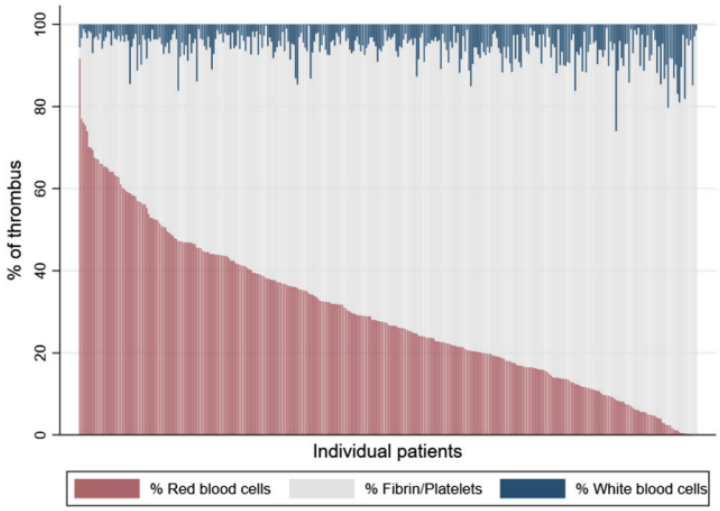

Figure 1.2: Overview of the composition of thrombi removed from patients with acute ischemic stroke. Adopted from [22].

Platelets, RBCs and fibrin all have an effect on the final composition and thus the mechanical properties of the thrombus. The features of the fibrin network, which functions as the adhesive between all components, have shown to influence thrombus strength, viscoelasticity, permeability and resilience to fibrinolysis [25]. Fiber diameter, fiber branching, fiber alignment and network density and porosity are such features that influence the mechanical properties of the thrombus [26–28]. Thrombi with thin, densely packed networks and many branching points result in a stiffer network, while networks with thick fibers are less stiff and more permeable [26, 27]. Furthermore, thrombus permeability decreases with higher fibrinogen and thrombin concentrations [26, 29]. The analysis of these features was done on fibrin gels made under static conditions, while in vivo thrombi are formed under flow. Known are the effects of fluid flow on the alignment of the fibrin fibers in the direction of the flow, though more research is required on the effects of flow on the microscopic features of the network [28].

1.1. Aim of the study

The aim of the thesis is to explore and answer the following research question: How does flow influence the micro-structure (i.e fiber thickness, pore size and fibrin density) of a fibrin thrombus and how is that reflected in the mechanical properties of the thrombus? Two devices, which can be used to form thrombi under flow in vitro, are the Chandler loop and microfluidic devices [30]. The former induces flow by spinning a tube filled with blood while the latter perfuses blood with a pump. Both methods will be explained, explored and assessed on their ability to form mechanically testable plasma thrombi under flow.

2

Materials and methods

To answer the research question two techniques, namely the Chandler loop and the tapered flow chamber, will be explored. Both support thrombus formation in the presence of flow. The former induces a flow profile by spinning a tube filled with fluid while the latter perfuses blood through a rectangular duct. The Chandler loop, being a rudimentary and simple method, can form thrombi that resemble thrombi extracted from stroke patients [30, 31]. Yet the fluid flow is difficult to control during thrombus formation. The fluid flow in the tapered flow chamber can be controlled more accurately, though the operation is more difficult. Just like the Chandler loop, has the microfluidic flow chamber been used to form thrombi with whole blood (WB) [32, 33]. Below the working mechanism of the Chandler loop will be explained, as well as all the steps taken to quantify the micro-structure of the fibrin network and the mechanical properties of the thrombus. The design of and the experiments done with the tapered flow chamber are included in Appendix A, as it is still in its preliminary stage.

2.1. Chandler loop

The Chandler loop is a simple method to create flowing thrombi in vitro [34]. It consists of poly vinyl chloride (PVC) tubings (inside diameter of 0.3 cm), which are rotated to induce a flow inside. Histologic analyses in previous research have shown that the Chandler loop thrombi are structurally the same as in vivo thrombi [35, 36]. Depending on the rotational speed of the Chandler loop, different shear rates can be simulated. The Chandler loop used for the experiments (Figure 2.1a) has a diameter of 10.7 cm and is rotating around an angle of 45°. The Chandler loop has a range of 10-40 revolutions per minute (RPM), of which 10 RPM and 30 RPM will be used to form thrombi in the presence of flow. 0 RPM thrombi will be made in the same tubes around the Chandler loop but without spinning of the loop. The thrombi were formed by adding 956 μm citrated platelet free plasma (PFP) pooled from three individuals, 15.7 μm fibrinogen labelled Alexafluor 488 (0.025 mg/ml) and 20 μm $CaCl_2$ (850 nM) in the Chandler loop tubes. The pooled PFP was obtained by spinning each person's WB at 2500g for 10 minutes separately. The plasma layer was taken off, which was then spun again at 2500g for 10 minutes to make sure all the platelets are removed from the plasma. After the second spin the plasma was pooled into a single stock. A step-wise protocol for the preparation of the Chandler loop thrombi can be found in Appendix B.1. During the experiments the plasma fills the lower half of the tubing, while the tubing is spun by the loop. The movement of the tubing will create a wall shear stress on the plasma and induce a flow pattern. The velocity profile (Equation 2.1) and shear rate (Equation 2.2) in the tubing can be found by solving the conservation of momentum equation, as shown by Gardner [30].

$$v(z) = \frac{\pi R}{15\,a^2}\,\omega\,(r^2 - \frac{a^2}{2}) \tag{2.1}$$

$$\gamma = \frac{4\,\pi\,R\,\omega}{45\,a}, \tag{2.2}$$

in which the radius of the loop (R) and the tubing radius (a) are given in m, the radial coordinate measured from the centre line (r) in radians, the rotational speed (ω) of the loop in revolutions per minute (RPM) and the shear rate (γ) in s^{-1}. The flow inside the tubing moves opposite to the rotation of the tubes and has a

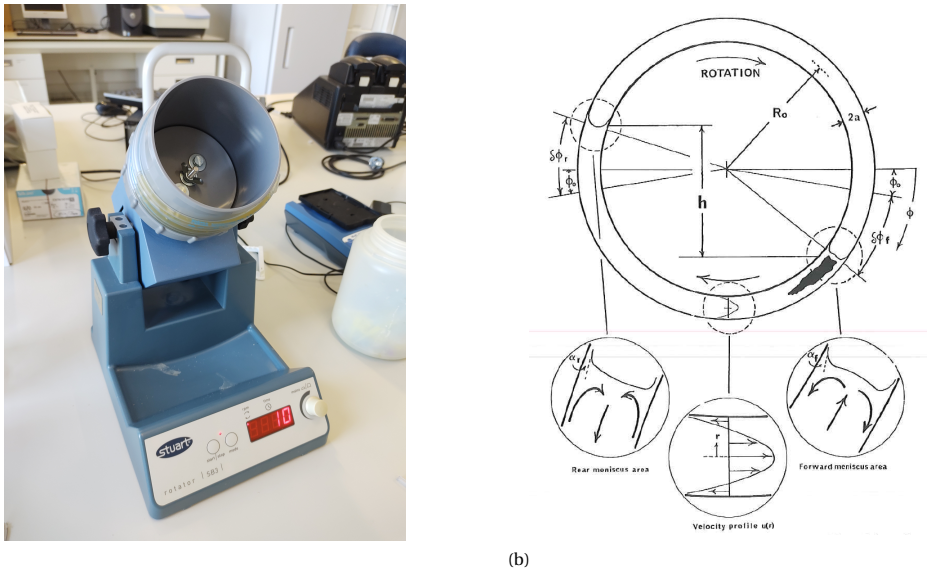

(a) (b)

Figure 2.1: a) The Chandler loop is shown, which was used to make thrombi at low (10 RPM) and high (30 RPM) shear rates. b) Schematic of the Chandler loop, highlighting the velocity profile and the forward and backward meniscus in the loop. Adopted from [30].

parabolic profile (Figure 2.1b). The menisci at the start and end of the fluid are stagnation points, though different in nature. The rotational speeds of 0, 10 and 30 RPM correspond with shear rates of roughly 0, 100 and 300 s^{-1} which allows for modelling of stationary thrombi, venous thrombi and the lower range of large arterial thrombi [37, 38].

Six thrombi were made for each of the three rotating speeds of the Chandler loop. During thrombus formation, a stopwatch was used to roughly estimate the clotting onset time of the thrombi and make sure that clotting started in the presence of flow. Two samples of each shear rate were dehydrated and used for Scanning Electron Microscopy (SEM) imaging. The remaining four samples were processed for compression testing and confocal imaging. They were cut into three pieces, of which the outer two pieces were used for compression testing, while the middle piece was kept for confocal imaging (Figure 2.2). The cutting of the three slices was done in the middle of the thrombus, excluding the thrombus head and tail. This gave a total of 4 samples of each shear rate for confocal and eight samples of each shear rate for compression testing. A summary of the number of samples for each shear rate can be found in Table 2.1. Compression testing and confocal imaging were done between 24-48 hours after thrombus formation. The thrombi for SEM imaging were dehydrated after 48 hours.

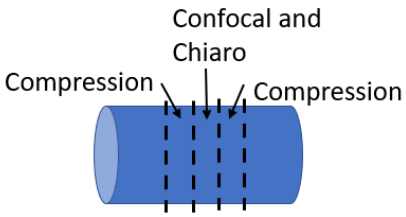

Figure 2.2: The thrombi were sliced into three pieces. The 10 and 30 RPM in pieces of 2 mm and the 0 RPM in pieces of 1 mm. The middle piece is imaged in the confocal microscope and used for micro-indentation, while the two outer pieces are used for compression testing.

2.2. Mechanical testing

To assess the mechanical properties of the thrombi both macroscopic unconfined compression testing and microscopic indentation were explored. The unconfined compression test will give bulk stiffness values, while with mico-indentation the heterogeneity of samples' stiffness can be measured. Both techniques will be discussed in depth below.

Table 2.1: Summary of the number of samples used for each shear rate of the Chandler loop.

	0 RPM	10 RPM	30 RPM
Nr. of Chandler loop samples	6	6	6
Nr. of SEM samples	2	2	2
Nr. of Confocal and Chiaro samples	4	4	4
Nr. of Compression samples	8	8	8

2.2.1. Unconfined compression testing

Unconfined compression testing, which is a relatively easy-to-use method to evaluate the strength and stiffness of thrombi, was used for the identification of the thrombus' mechanical properties. During an unconfined compression test, the sample is compressed between a solid surface and a compression plate (Figure 2.3a and Figure 2.3b). During the compression, the sample can expand radially without hindrance. The mechanical tester used during the experiments was custom-made for unconfined compression testing of thrombi by Boodt et al. [39]. The samples were compressed by displacing a 2.5 N load cell (Jr. Miniature S-Beam Load Cell, model LSB200, Futek) with an aluminium compression plate on a thrombus. The thrombus was placed on the compression tester stage, which was inside a temperature-controlled basin (37°C) filled with HEPES buffer. The samples were compressed for 10 consecutive cycles with a contraction and retraction speed of 0.1 mm/s. They were compressed to 80% of their initial height, which was 1 mm for the 0 RPM samples and 2 mm for the 10 and 30 RPM samples. The difference in height between the 0 RPM and the 10 and 30 RPM was due to the smaller size of the 0 RPM thrombi, which did not reach a height of 2 mm. Before compression, the cross-sectional area of the sample was imaged by placing the thrombus in a petri-dish filled with HEPES buffer (Figure 2.3c). Below the dish a ruler was placed and an image with both the ruler and thrombus in view was taken. With ImageJ the surface area of the thrombus was extracted. The ruler was used to establish the pixel-to-length ratio and with the freehand selection tool the surface area of the sample was computed. With the cross-sectional area known the load data was converted to nominal stress, as shown by Equation 2.3:

$$\sigma = \frac{P}{A_0}, \tag{2.3}$$

in which P is the recorded load (N) by the load cell and A the cross-sectional area (m^2) of the sample before compression. With the start and end positions and the speed of compression known the time data could be converted to engineering strain data, which is the relative deformation of the sample (Equation 2.4).

$$\epsilon = \frac{l - l_0}{l_0}, \tag{2.4}$$

in which l is the sample height (m) and l_0 the starting height of the sample (m). In both the calculation of the nominal stress and the engineering strain, the length and diameter of the sample are assumed to remain constant during the experiment.

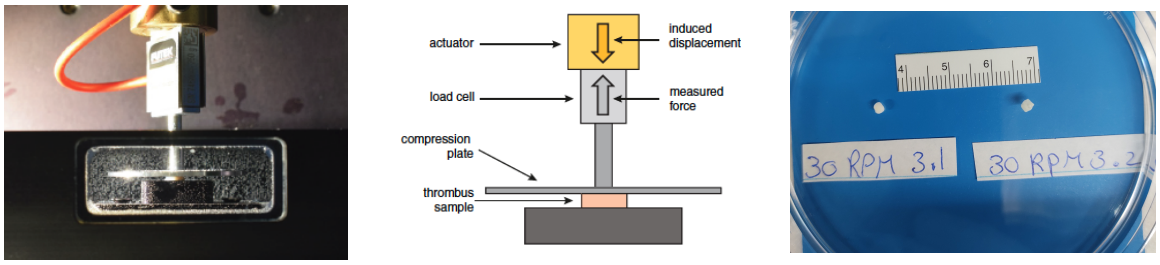

(a) (b) (c)

Figure 2.3: a) Unconfined compression test of a thrombus in a temperature-controlled buffer basin. Adopted from [39]. b) Schematic of the unconfined compression tester. By displacing the compression plate, which is connected to a load cell, the force applied by the thrombus on the plate was recorded. Adopted from [39]. c) Example image used for the recording of the surface area of the thrombi. The ruler was used to establish the pixel-to-length ratio of the image and with the freehand selection tool in ImageJ, the surface area was computed.

Compression of the samples was recorded for 10 consecutive cycles. The tangent modulus was calculated for the first 20-40% and the final 75-80% strain of the first loading cycle by curve fitting of a linear equation. The first 20-40% was chosen to represent the first linear elastic response of the material while the final 75-80% of the curve represents the stiffening of the material due to high strains. Furthermore, due to the viscoelastic behaviour of the thrombi, the loading and unloading during compression are time-dependent and energy can be lost during a cycle [40]. The viscous energy or hysteresis energy, which is the area between the loading and unloading curve of the stress-strain data, was computed. This measures the dissipation of the energy during each consecutive compression. The Matlab codes used for data processing can be found in Appendix D.1.

2.2.2. Micro-indentation

Micro-indenters are compact instruments for mechanical testing of the micro- to macro-scale [41, 42]. The micro-indenter consists of a probe and an interferometer. The probe is an optical fiber inside a borosilicate glass ferrule and a cantilever with a spherical tip (Figure 2.4a) at the end of the probe. Laser light from the interferometer is trapped in the optical fiber by a refractive index difference (i.e. light-bending ability of a medium) between the fiber core and a glass ferrule, creating a Farby-Perot cavity [41, 43]. At the end of the fiber the refractive index changes due to the introduction of a new interface and part of the light is reflected back into the fiber (Figure 2.4b). Then when the light reaches the cantilever the light is reflected into the fiber as well [44]. The interference (i.e. multiple electromagnetic waveforms forming a resultant wave, which has a reinforced or cancelled amplitude) of the returning waveforms is detected by a photodiode in the interferometer. When the cantilever is displaced during indentation, the interference of both returning signals changes due to a decrease in gap size between the cantilever and the fiber end. This change in interference allows for precise measuring of the cantilever deflection.

(a) (b)

Figure 2.4: a) Microscopic image of the probe. Adopted from [45]. b) Schematic view of the light emission paths through the fiber at the front of the probe. The incoming light is reflected back into the fiber at the fiber end and at the cantilever surface. Adopted from [44].

The load applied (F) on the sample during indentation depends on the stiffness of the cantilever and the cantilever deflection:

$$F = k \cdot D, \tag{2.5}$$

in which k is the cantilever stiffness (N/m) and D the cantilever deflection (m) [42, 46]. Furthermore, the indentation depth (D_i) can be obtained by subtracting the cantilever deflection (D) from the displacement of the probe (D_f), shown in Equation 2.6:

$$D_i = D_f - D, \tag{2.6}$$

As the contact point of the tip of the cantilever is spherical, the contact area of the tip with the sample is dependent on contact depth. The contact depth can be computed with Equation 2.7:

$$h_c = \frac{h_{max} + h_r}{2}, \tag{2.7}$$

in which the h_c is the contact depth (m), the h_{max} the maximum indentation depth and the h_r the residual indentation depth. Both the contact depth and the maximum indentation depth are shown in Figure 2.5a [46, 47]. The final indentation depth is the depth at which the sample is unloaded. Then with the contact depth and the Pythagorean theorem (Equation 2.8 and Figure 2.5b), the radius of the contact circle (Equation 2.9) can be determined [46–48].

$$r^2 = (R - h_c)^2 + a^2, \tag{2.8}$$

$$a = \sqrt{2\,R\,h_c - h_c^2}, \tag{2.9}$$

in which R is the sphere radius (m), h_c the contact depth (m) and a the radius of the contact circle (m) [46, 47]. The quadratic term in the square root can be neglected for a contact depth significantly smaller than the radius of the indenter [46]. With the radius of the contact circle known, the indentation area can be calculated with A = πa^2.

The mechanical behaviour of fibrin networks can be described as visco-elastic, as energy is dissipated during load application. As the visco-elastic network is indented with a spherical probe, the Hertzian contact model can be used to calculate the contact stress of the indented sample with Equation 2.10:

$$P = \frac{3F}{2\pi A}, \tag{2.10}$$

in which P is the contact stress (Pa), F the recorded load (N) and A the contact area of the probe (m^2) [42, 43]. Noted is that the Hertz model only applies to fully elastic contacts with small indentation depths (as compared to the indenter radius) and no adhesive forces [42]. Furthermore, the maximum indentation depth should not exceed 5-10% of the sample thickness to prevent sensing the substrate beneath the sample [43].

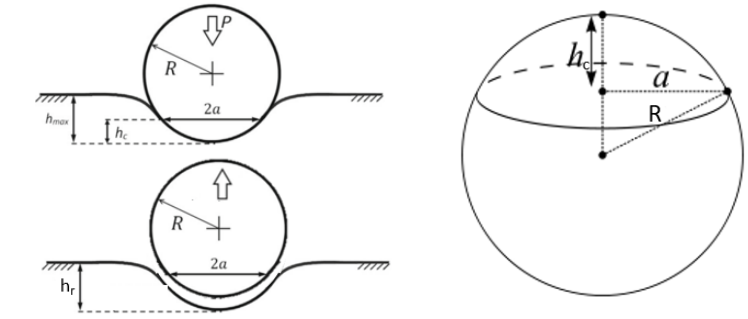

(a) (b)

Figure 2.5: a) Schematic view of the indentation of a rigid sphere in an elastic material. The top scheme shows the indentation at maximum indentation, while the bottom scheme shows the moment the indenter loses contact with the sample during unloading. Adapted from [46]. b) Visualisation of the Pythagorean Theorem inside the cap of a sphere. Adapted from [49].

The thrombi were indented with the Chiaro micro-indenter at TU Delft. The chosen probe had a radius tip of 103 μm and a cantilever stiffness of 0.40 N/m. A tip radius of 103 μm is sufficiently large to prevent measuring between fibrin fibers, as the average pore size found in literature is between 2-7 μm [50, 51]. The samples were glued on the bottom of the petri-dish with two-component glue to make sure that the samples did not move during indentation. The samples were measured in air instead of in buffer, as the buffer dislodged the glued samples. The probe was calibrated on the bottom of the glass petri-dish prior to the measurements. Then the surface of the sample was found with the "find surface tool". After a waiting period of 5 minutes, an indentation was done by displacing the tip 15 μm in 10 seconds. Then the probe is held in place for five seconds, after which the probe unloads the sample with the same velocity. To compute the tangent modulus, the contact stress (Equation 2.10) and engineering strain (Equation 2.4) are used. Preliminary experiments showed that finding the surface of the samples was difficult and all measurements taken were started with the tip already in contact with the sample. For these cases, h_c was taken as h_{max} to compute the cross-sectional area of the indentation. The Matlab code used for data processing can be found in Appendix D.1

2.3. Imaging

To evaluate the structural features of the fibrin network of the thrombi, two imaging methods were used: Confocal Laser Scanning Microscopy (CLSM) and Scanning Electron Microscopy (SEM). To visualise living structures with a CLSM a fluorescent dye is attached to a structure of interest and illuminated by a light source (i.e. laser). The photons emitted by light are absorbed by the dye, which gives an electron enough energy to leave the ground state (Figure 2.6a) and go to a higher energy state (e.g. S1 or S2) [52]. An electron in a higher energy state is very unstable and it relaxes towards the ground state by emitting a photon [52]. The

emitted photon is lower in energy due to the vibrational relaxation in its new energy state [52]. The confocal laser scanning microscope (Figure 2.6b) detects the photon emitted by the sample. It filters out-of-plane rays with a pinhole to remove noise from out-of-focus parts of the sample that are illuminated as well [53]. The laser is swept over the sample with mirrors, allowing a large field of view in the x-y plane [53]. To create three-dimensional images the focus point is altered and for each focus point an x-y scan is made (often called a z-stack). Important to note is that high laser power can damage the sample (i.e. photobleaching) and that thick samples are difficult to image due to scattering of the light [53]. For imaging during the experiments, a Leica CLSM was used. Different settings were used for the static thrombi and the thrombi formed in the presence of flow in the Chandler loop. For the static thrombi formed inside the tubing for the Chandler loop, z-stacks were made in the confocal microscope with a 40x immersion lens and the 488 nm laser (4%; gain: 1115). A zoom of 2 was applied, which resulted in images of 193x193 μm with 2048x2048 pixels. As these settings were unsuitable (i.e. network features not distinguishable) for the thrombi formed in the presence of flow, z-stacks were made with a 63x immersion lens and the 488 nm laser (80%; gain: 679). A zoom of 2 was applied, which resulted in images of 123x123 μm with 2048x2048 pixels. The image speed was set at 200 Hz for all images.

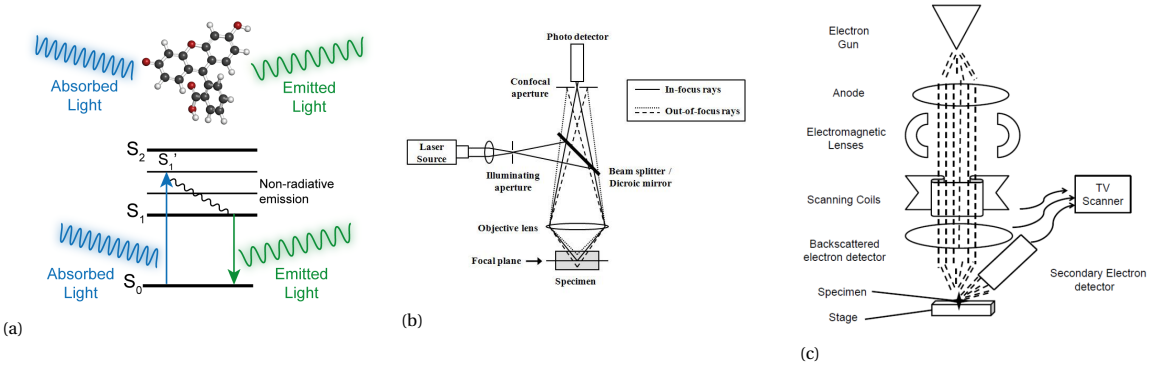

Figure 2.6: a) Jablonski diagram, which shows that when a fluorescent dye absorbs a photon, an electron is excited from the ground state. When the electron relaxes it emits a photon with lower energy. Adopted from [54]. b) Schematic of a confocal microscope. Adopted from [55]. c) Schematic of a Scanning Electron Microscope. Adopted from [56].

While confocal is an appropriate measuring method for surface area coverage and pore size, the resolution of the confocal microscope is not sufficient to measure the fibrin fiber diameter. SEM is able to get an appropriate resolution to extract the diameter of fibrin fibers. Instead of imaging with light, an electron beam is focused on the sample [57]. After electron generation, they are passed through a series of lenses and apertures to produce a focussed electron beam [58]. This beam can be controlled by scanning coils, which allow for scanning of the surface of the sample. When the electrons hit the sample, secondary back-scattering electrons are created which are collected by a detector. With the back-scattered electrons the morphology of the surface of the sample can be captured [59]. As the imaging takes place in a vacuum to prevent back-scattering of electrons on other molecules than the sample, the sample needs to be dehydrated before imaging. As dehydration alters and collapses the network the confocal microscope is used for the surface area measurements and pore size measurements instead. To prepare the Chandler loop thrombi for SEM imaging, they were washed in cacodylate buffer, fixed with glutaraldehyde, dehydrated in ethanol, dried with hexamethyldisilazane (HDMS) and sputter-coated with gold. A full description of the protocol can be found in Appendix C. The SEM images were taken at the ImPhys centre at TU Delft, on a Focussed Ion Beam Scanning Electron Microscopy (FIB-SEM). The backscattered ions were detected with an Everhart-Thornley detector at a high voltage of 10 kV, with a tilt of 0.0°, a dwell time of 3 μs and a working distance of 4.46 mm. The final images were 20.8x14.8 μm with 3072x2188 pixels.

2.4. Image analysis

The acquired images, with both confocal and SEM imaging, were processed to extract the fiber surface area, the pore sizes in the fiber network and the fiber thickness. The processing steps taken are elaborated below.

2.4.1. Area

Fiber density of the fibrin network is quantified using the percentage of surface area coverage of the fibrin fibers in the taken image (Figure 2.7). The first step in the extraction of the percentage of surface area coverage of the fibrin fibers is duplication of the image stack. By duplicating the stack, the original stack is kept and stays unaltered, while the duplicate can be processed. The duplicate is treated with a Gaussian blur (σ = 2), which functions as a low pass filter and decreases the noise in the duplicate image. With the Otsu threshold, which is one of the auto-threshold methods provided by ImageJ, the duplicate image is converted to a binary image. The Otsu threshold was chosen after visual testing all the provided auto-thresholds by ImageJ, in which Otsu filtered background from fibers the best. This resulted in an image in which the fibers are coloured black and the background white. Then the original image stack and the processed duplicate stack are combined by the image calculator, with operation AND. This will return a stack with the values of the original image, but only if the second image has a non-zero value as well, effectively removing all the background noise without altering the intensity of the imaged fibers. On this new set, a threshold of 1 to 255 is used to measure the area of the fibers of each slice in the stack with analyse particles function in ImageJ. The values 1 to 255 are chosen as all the non-zero pixels remaining in the image are fibers and are thus part of the surface area coverage. Particles analysed were set to be at least 5 pixels large and could be shaped as perfect circles or elongated polygons (i.e circularity = 0.0-1.00). ImageJ returns the percentage of surface area per stack slice, which is saved in a .csv format. The macro written for the surface area measurements can be found in Appendix D.2.

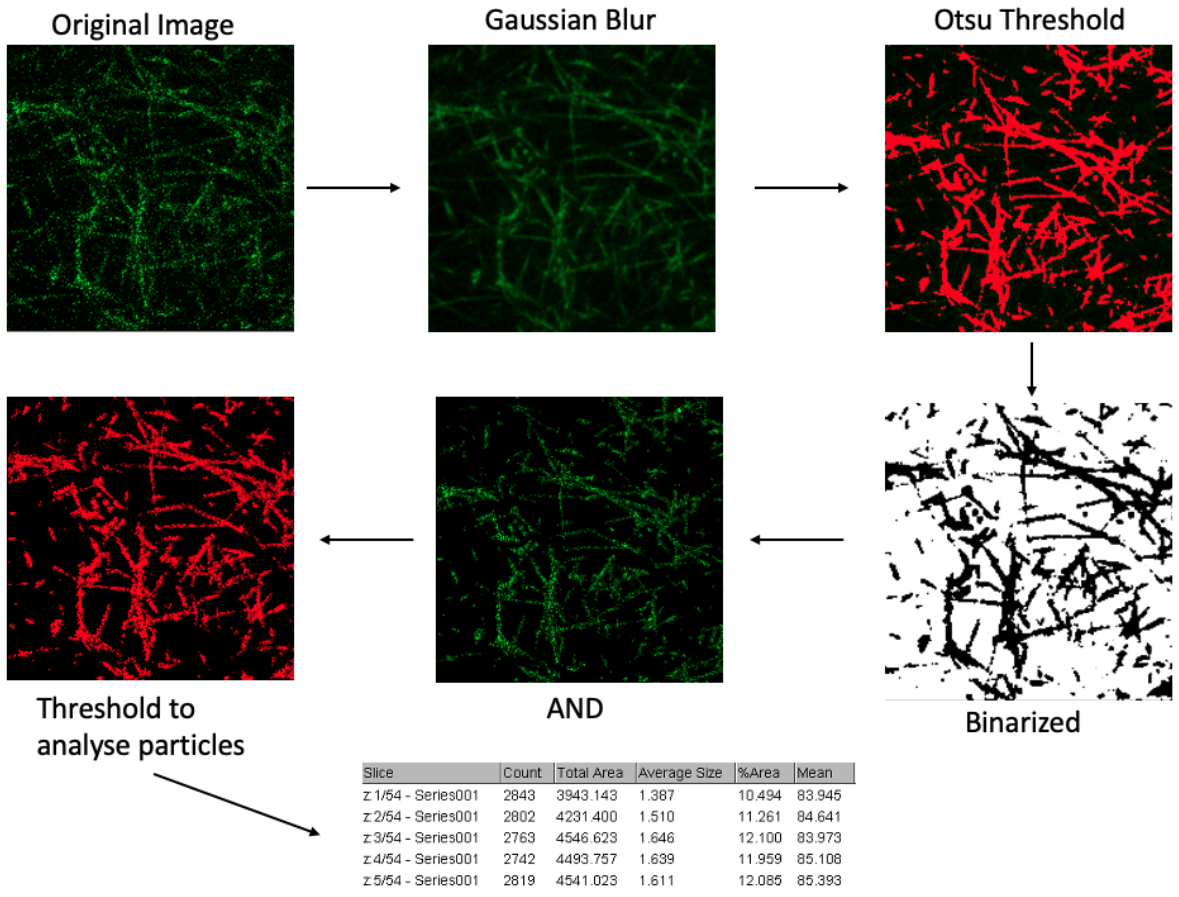

Figure 2.7: The image analysis steps taken in ImageJ to extract the percentage of surface area coverage of the fibrin fibers per image. A duplicate of the original image is treated with a Gaussian blur, then thresholded with Otsu and converted to a binary image. The original image and the binary duplicate are added with the image calculator operator AND, which removes all the background noise in the image but retains the original fiber intensity. Then the image is thresholded and the surface coverage of the fibers is extracted.

2.4.2. Pore size

Pore size distributions inside networks give information on the rheology and diffusive transport of a network. Most pore size analyses are done with SEM imaging. To image thrombi with SEM, the samples need to be dehydrated, thereby collapsing the fibrin network. Molteni et al. and Münster et al. have shown that pore size can be extracted from 2D confocal images [60, 61]. By further developing the code provided by Münster et al., the size of the pores in fibrin networks in confocal images could be extracted. The analysis starts with converting the image (background noise has been removed with ImageJ, as discussed above) to a binary image. This makes sure that all the pixels that are part of a fiber are given a 1, while the pixels that are not part of a fiber a 0. Euclidean distance map (EDM) of the image is calculated, which returns the distance to the nearest non-zero pixel (i.e. fiber pixel) for each pixel in the image. The local maxima in the EDM, which are pixels whose surrounding eight pixels are lower in value, represent the coordinates and the radius of a circle, whose edges border fibers. To prevent boundary effects, all circles that extent outside the border of the image are removed [61]. Furthermore, all bubbles with a radius smaller than three were removed, as manual observation of the images showed that smaller bubbles were beyond the pixel resolution. To apply the including and discarding criteria proposed by Molteni et al. the circles were sorted from largest to smallest [60]. The largest circle in the list was accepted as the first included circle in the included list. Then the next circle in the sorted list (i.e large to small) would be compared to all circles in the included list (i.e will be growing with each addition) and added to the included circle list if the following criterion is true: if the centre of the smaller circle lies inside one of the larger circles of the included list the circles are largely overlapping and the smaller circle is not included. This criterion is true when the distance between the centres of the circle is smaller than the maximum between the two circles' radii. This filtering method filters out largely overlapping circles (Figure 2.8). In Appendix C.3 a comparison between two inclusion and discarding methods can be reviewed and in Appendix D.3 the code written for the pore size analysis can be found.

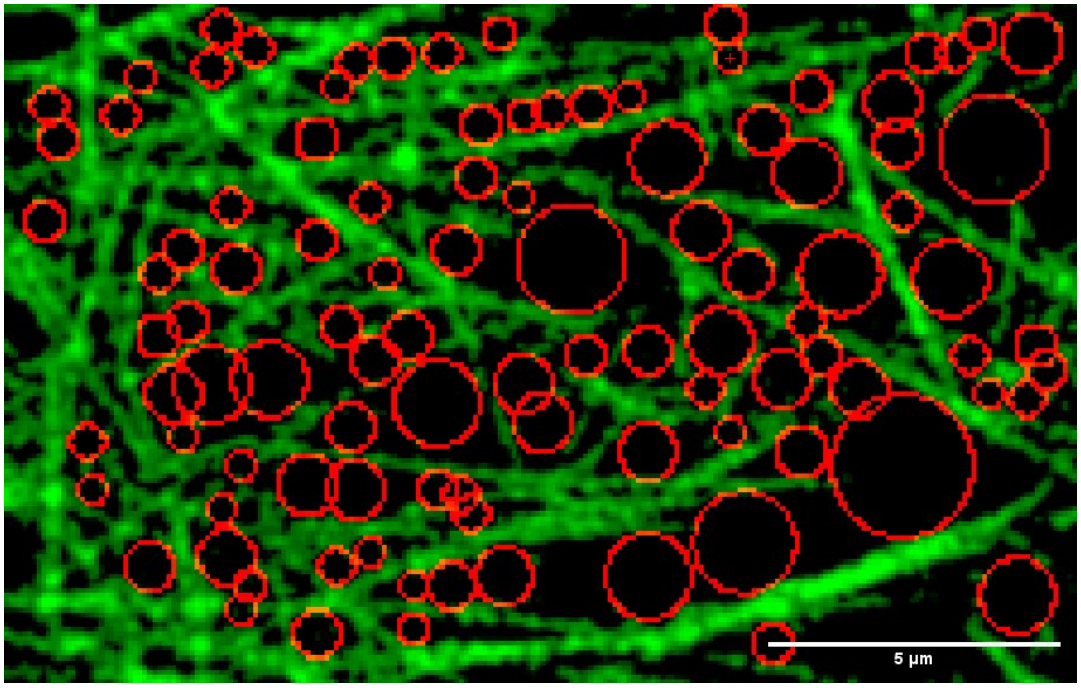

Figure 2.8: Circles found in a fibrin network after the inclusion and discarding criterion from Molteni et al. [60]. The circles are allowed to overlap as long as the centres of the circles are outside of the other circle.

2.4.3. Fiber thickness

The third and last micro-structure parameter analysed in this thesis is the fiber diameter. The SEM images are analysed with DiameterJ, which is a plug-in for the open-source image analysis program ImageJ (Figure 2.9). It was designed for a porous nano-fiber scaffold and validated on synthetic images and electrospun polymeric nanofibers [62]. Furthermore, it has been previously used to extract the diameters of fibrin networks [27, 63]. The diameter analysis was done on SEM images with a horizontal field width of 20.7 μm,

which corresponds to a pixels size of 7 nm. The DiameterJ plugin offers 24 segmentation algorithms to convert the images to binary representations which are based on either global, local, machine learning or edge detection methods. After segmentation, DiameterJ provided a montage of all the segmentations to visually check the appropriateness of all the segmentations. Segmentation method S3 (i.e. Statistical Region Merging of order three) was used to analyse both the static and flow thrombi. Then to calculate the fiber diameter, DiameterJ uses a thinning algorithm to find the fiber centre lines and an EDM to find the distance between a fiber pixel and its nearest non-fiber pixel [62]. The distance map is then linearly transformed to greyscale values, obtaining a greyscale image. Then the fiber centerlines are laid on top of the greyscale image. Next, the greyscale value of each intersection was found and radius values within the range of the greyscale value were subtracted out from the centerline to remove the intersections. The remaining greyscale values were obtained and multiplied by two and converted to diameter values (μm).

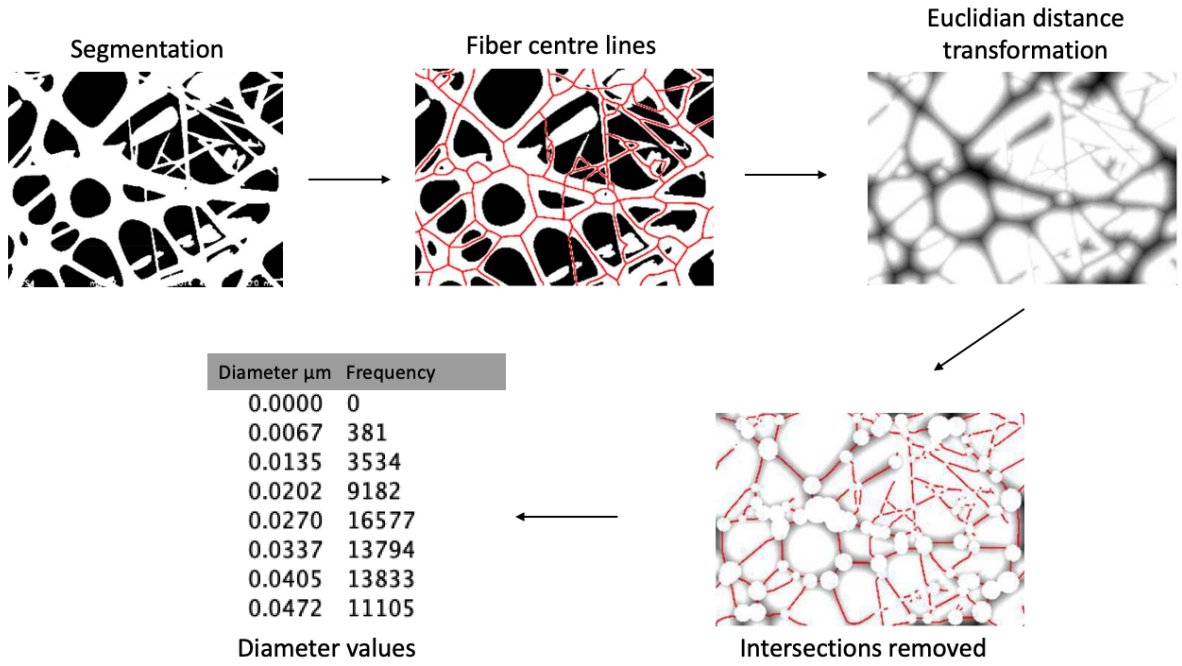

Figure 2.9: Image analysis steps taken by DiamterJ to calculate fiber diameters. After segmentation of the image, the fiber centre lines are obtained. Furthermore, the image is transformed into a greyscale Euclidian distance map. Then by overlaying the centre lines and the greyscale Euclidian distance map, the fiber intersections were removed. From the remaining fiber centre lines, the diameter of the fibers was calculated.

2.5. Statistics

To test the variability and significance of the experiment, multiple Kruskal-Wallis tests were performed. The Kruskal-Wallis will test whether the data medians of the three conditions (i.e. 0 RPM, 10 RPM and 30 RPM) are significantly different from one-another. When significant the Dunn post hoc test will show which of the specific groups differed. The test was performed with the statistical programme Jasp.

3

Results

3.1. Chandler loop

The thrombi formed in the Chandler loop at 0 RPM (n=6), 10 RPM (n=6) and 30 RPM (n=6), showed differences in appearance (Figure 3.1). Clotting started between 20 and 30 minutes after starting the Chandler loop and thus the formation of the thrombi was in the presence of flow. The static thrombi (0 RPM) are long, opaque, snake-like structures with plasma still residing inside the network. During the formation of the thrombi at 10 RPM the plasma first started to get cloudy due to the formation of fibrin fibers, which then would accumulate at the forward meniscus in the loop (Figure 2.1b) and form a thrombus. Shortly after the accumulation of the fibrin, all 10 RPM thrombi got stuck at the seal of the tubing and remained stuck for the rest of the spin. The head of the thrombi (i.e at the forward meniscus in the loop) looked denser and was no longer translucent, while the tail of the thrombus was opaque and resembled the thrombi formed under static conditions. Immediately after the thrombi were removed from the Chandler loop, visual differences between the 0, 10 and 30 RPM thrombi could be seen. The thrombi formed at 30 RPM were smaller and seemed denser and sturdier than the thrombi formed at 0 and 10 RPM. When the thrombi were cut in disks, the 30 RPM thrombi were easier to handle and easier to cut in three disks, while cutting off the 0 and 10 RPM could disfigure the disk due to their fragility and deformability. A summary of the appearance and sturdiness of the thrombi can be found in Table 3.1.

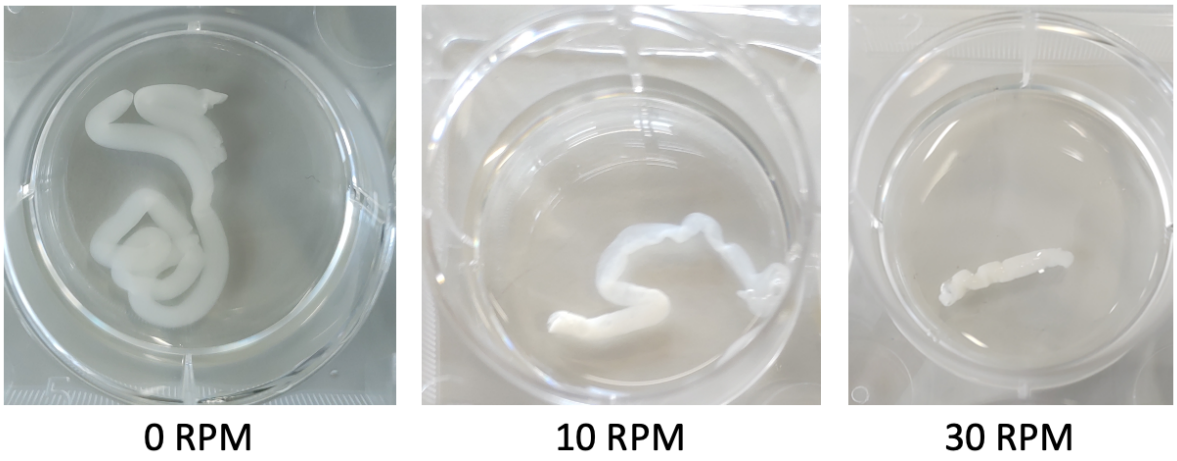

Figure 3.1: Thrombi formed in the Chandler loop at 0, 10 and 30 RPM. The static clots (0 RPM) were long and more opaque than the thrombi formed in the presence of flow (10 and 30 RPM). Both the 10 and 30 RPM thrombi were denser and smaller in size compared to the 0 RPM thrombi. The 10 RPM thrombi had a dense head resembling the 30 RPM thrombi and a large tail resembling the thrombi formed at 0 RPM.

Table 3.1: Thrombus appearance for thrombi formed at 0, 10 and 30 RPM. Additionally, the differences in sturdiness have been recorded.

Rotation speed (RPM)	Appearance	Sturdiness
0	Long opaque snake-like structures	Very soft and hard to cut
10	White head with a long opaque tail	Soft and moderately easy to cut
30	Small white thrombi	Sturdy and easy to cut

3.1.1. Thrombi morphology

As discussed before, the thrombi formed at 0, 10 and 30 RPM were different in appearance. During SEM imaging, a difference in homogeneity between the static (0 RPM) and flow thrombi (10 and 30 RPM) was seen (Figure 3.2). Both the 0 and 10 RPM thrombi have a horizontal field width of 104 μm, while the 30 RPM has a horizontal field width of 200 μm. Firstly, the rightmost image is an example of a typical 0 RPM thrombus. The fibrous network is random in nature and very uniform. All 0 RPM SEM images showed the same uniform randomness, making the images very similar and indistinguishable. Secondly, the middle image, which is an example of a thrombus formed in the presence of flow, is very different from the 0 RPM thrombus. Having the same horizontal field width the fibers of the thrombus formed in the presence of flow are smaller and denser compared to the 0 RPM thrombus. Furthermore, the alignment of the fibers is no longer random in the flow thrombus. Multiple regions with different alignment directions can be found. The red arrows show the difference in alignment direction with the thrombus. All 10 and 30 RPM thrombi, which were the thrombi formed under flow, showed these patch-like regions with different fiber alignment orientations. Besides having fiber alignment the 10 and 30 RPM thrombi have a relief, while the 0 RPM thrombi are flat. The orange frame in the middle image highlights the differences in relief found in the flow thrombi. Finally, the image on the right shows another flow thrombus. In this image, two regions, separated by the dashed blue line, with a difference

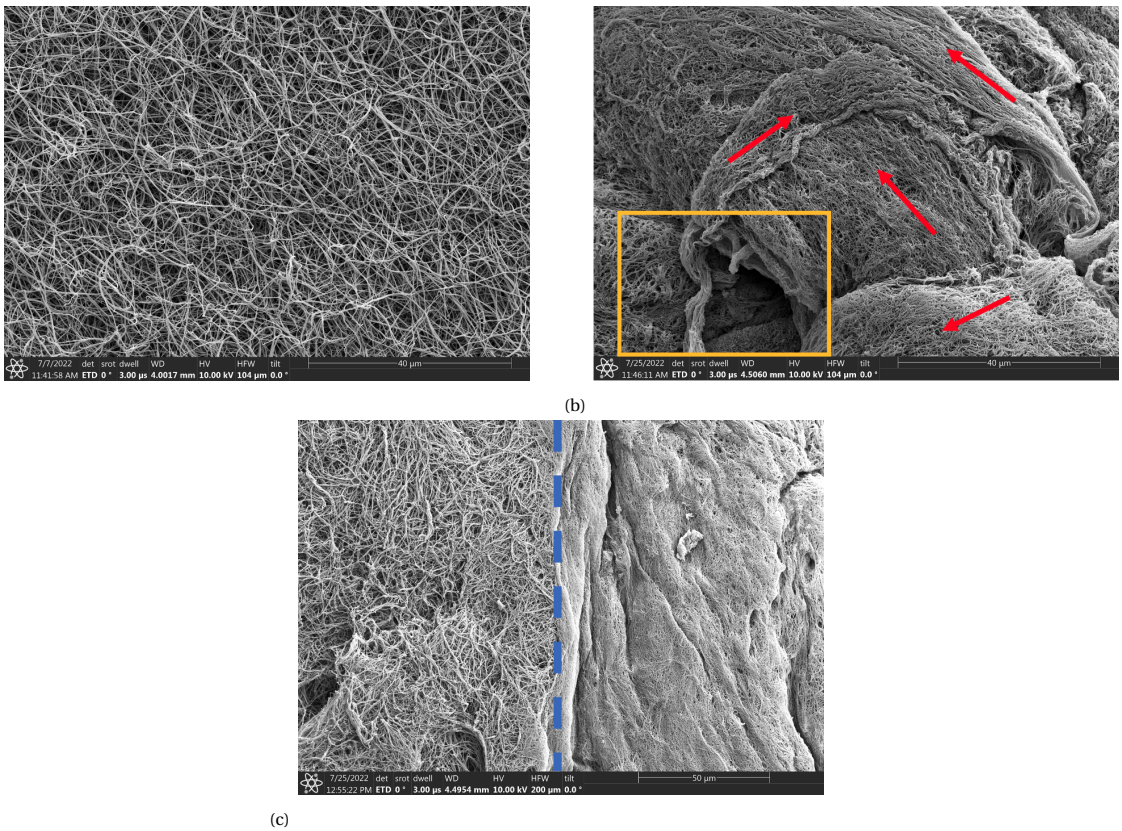

(a) (b) (c)

Figure 3.2: a) An example of a typical 0 RPM thrombus, with a uniform randomly aligned network. The image has a horizontal field width of 104 μm. b) An example of a thrombus formed in the presence of flow. The red arrows show the alignment differences in a single thrombus. The orange frame highlights the differences in relief found in the flow thrombi. The image has a horizontal field width of 104 μm. c) Another example of a thrombus formed in the presence of flow. The dashed blue line separates two regions with differences in fiber diameter and fiber density. The image has a horizontal field width of 200 μm.

in fiber density and diameter can be seen. While the 0 RPM thrombus was very uniform, the flow thrombi showed a difference in fiber diameter and fiber density between different parts of the thrombus.

3.1.2. Fiber diameter

Two samples of the six thrombi made for each shear rate were prepared for and imaged with SEM. Of each thrombi 5 images were taken at random positions on the sample surface. Visually, it was observed that the 10 and 30 RPM thrombi showed decreased fiber diameter compared to the 0 RPM thrombi (Figure 3.3). Additionally, the density of the fibers seems to be increased for the 10 and 30 RPM thrombi compared to the 0 RPM thrombi, which will later be quantified with the confocal images. Furthermore, the fibers in flow thrombi can coalesce into thicker fibers, which is very prominent in the top right image of Figure 3.3, while less conspicuous in the other examples of flow thrombi. Finally, the alignment of the fibers of the flow thrombi appear to be in different directions. As discussed in Section 3.1.1 the alignment in flow thrombi can differ depending on which region of the thrombus is imaged and thus the direction of the alignment seen in the images cannot be linked to the direction of flow even though all the images are taken in the same orientation.

After quantification of the fiber diameters by DiameterJ, the 10 and 30 RPM thrombi showed a similar distribution, which is more narrow than the diameter distribution of the 0 RPM thrombi (Figure 3.4a). The bulk of the fiber diameters are between 0 and 600 nm, after 600 nm some larger fibres are found, but their number is negligible compared to the bulk of the fiber diameters that are between 0 and 600 nm. The mean fiber diameters found are 94 ± 1.7 nm, 51 ± 4.1 nm and 54 ± 4.0 nm for 0 RPM, 10 RPM and 30 RPM, respectively (Figure 3.4b). The fiber diameter decreases for the thrombi formed in the presence of flow. There is a statistical difference between the 0 RPM and the 10 and 30 RPM groups ($p < 0.001$ and $p < 0.001$), while no statistical difference was found between 10 and 30 RPM ($p=0.223$).

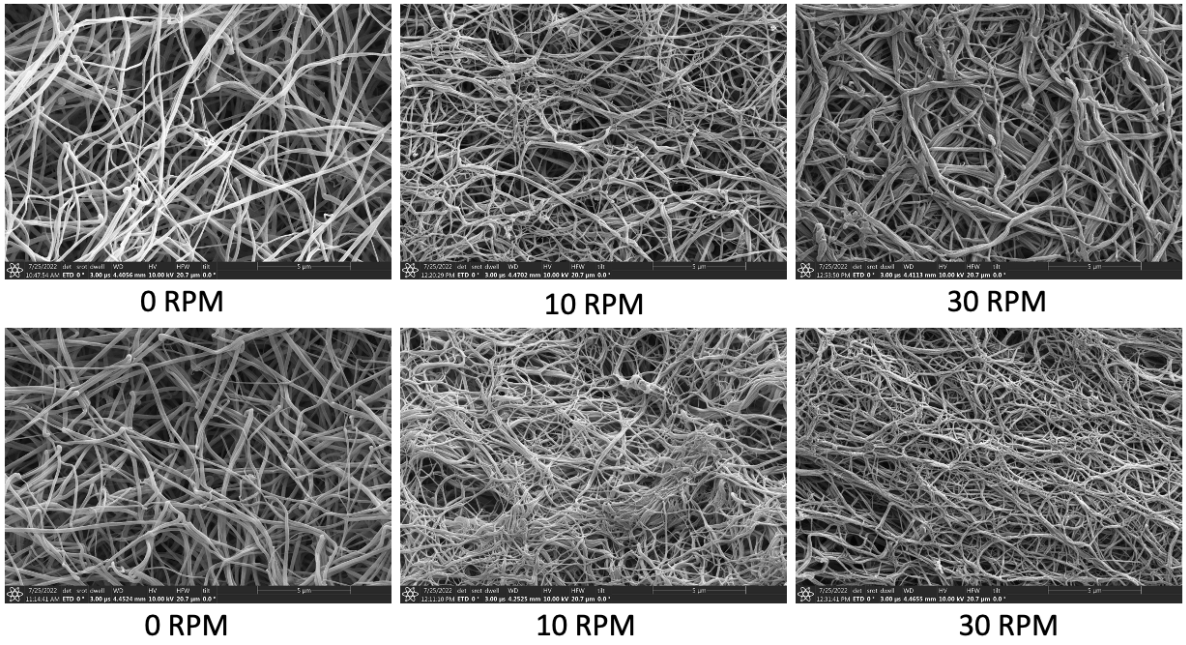

Figure 3.3: SEM images of the thrombi formed in the Chandler loop at 0, 10 and 30 RPM. Two sets of images of each condition are shown all having the same horizontal field width of 50 μm and showing visual differences between the three shear rates. The thrombi formed in the presence of flow show fiber alignment, though this is not linked to the direction of flow.

3.1.3. Area

The middle slice of the midsection of the thrombus, as explained in Section 2.1, was used for confocal imaging. Each condition (i.e 0, 10 and 30 RPM) had four thrombi imaged and of each thrombi, five z-stacks of 11 μm were taken. Imaging the 10 and 30 RPM thrombi was more challenging than imaging the 0 RPM thrombi. Even though settings were adjusted (Section 2.3), it resulted in hazier images for both 10 and 30 RPM thrombi and a decreased number of z-stacks of the 30 RPM thrombi. Instead of having four thrombi with five z-stacks, only three thrombi were imaged with either two or a single z-stack. Visually, it was observed that the 10 and 30

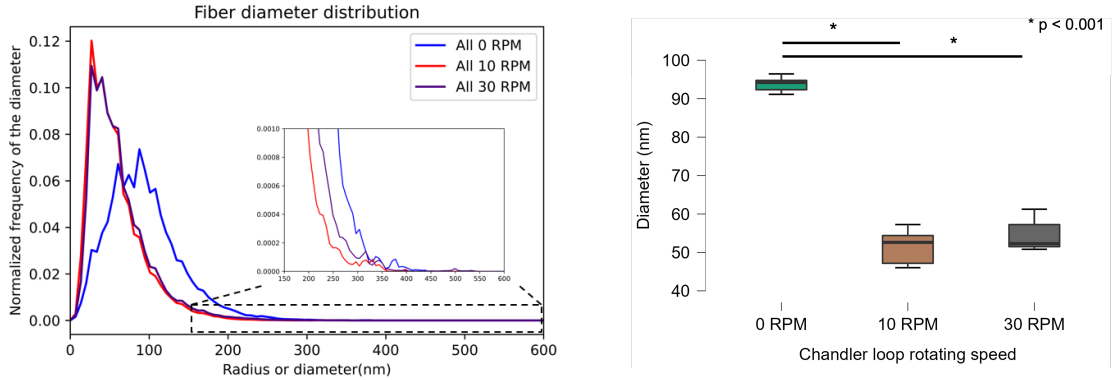

(a) (b)

Figure 3.4: a) The frequency of diameter occurrence of the fibers. The 10 and 30 RPM thrombi show a similar distribution, which is more narrow than the diameter distribution of the 0 RPM thrombi. b) Boxplot of the fiber diameter found in the thrombi. The mean fiber diameters found are 94 ± 1.7 nm, 51 ± 4.1 nm and 54 ± 4.0 nm for 0 RPM, 10 RPM and 30 RPM respectively. The fiber diameter decreases for the thrombi formed in the presence of flow. Both the 10 and 30 RPM have decreased fiber diameters compared to the 0 RPM ($p < 0.001$ and $p < 0.001$). Between 10 and 30 RPM no statistical difference was found (p=0.223).

RPM showed increased density of the fibers compared to the 0 RPM thrombi (Figure 3.5). The 0 RPM thrombus, displayed on the left, also shows a randomly aligned network, while for the 10 and 30 RPM thrombi a clear direction in the alignment of the fibers can be found.

To calculate the fiber density the surface area coverage of the thrombi was extracted with ImageJ, as discussed in Section 2.4.1. The surface area coverage of each μm in the first 11 μm of the thrombus can be found in Figure 3.6a. The figure shows the average surface area coverage of five stacks made of each thrombus. The fiber density shows small fluctuations in density when imaging deeper in the thrombus, both decreasing and increasing in nature. The density of the 10 RPM thrombi (shown in different shades of red) are similar and lie together closely. A large difference in surface area between the 0 RPM thrombi was noticed (shown in different shades of blue). Two of the 0 RPM thrombi have a surface area coverage of below 20% while the other two are around 30% which is closer to the 10 and 30 RPM thrombi. Additional graphs, which display each shear rate and image stack individually can be found in Appendix E.

Overall the fiber density of the thrombus is increased (Figure 3.6b) for the thrombi formed in the presence of flow. There is a statistical difference between the 0 RPM and the 10 and 30 RPM groups (p=0.017 and p=0.007), while no statistical difference was found between 10 and 30 RPM (p=0.323).

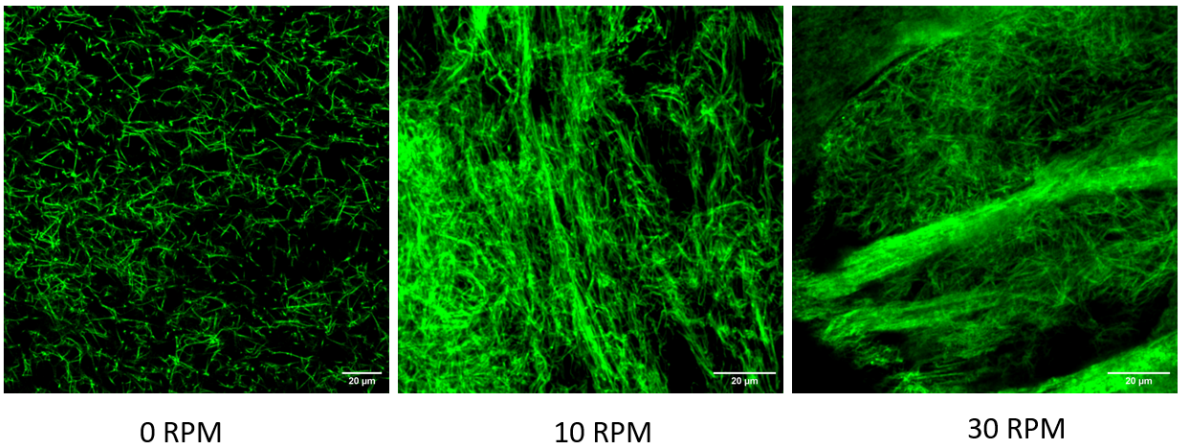

Figure 3.5: Confocal images of the thrombi formed in the Chandler loop at 0, 10 and 30 RPM. The static thrombi (0 RPM) show a randomly aligned network, while both the 10 and 30 RPM thrombi show fiber alignment. Visually, there seems to be an increase in fiber density for the 10 and 30 RPM thrombi compared to the 0 RPM thrombi.

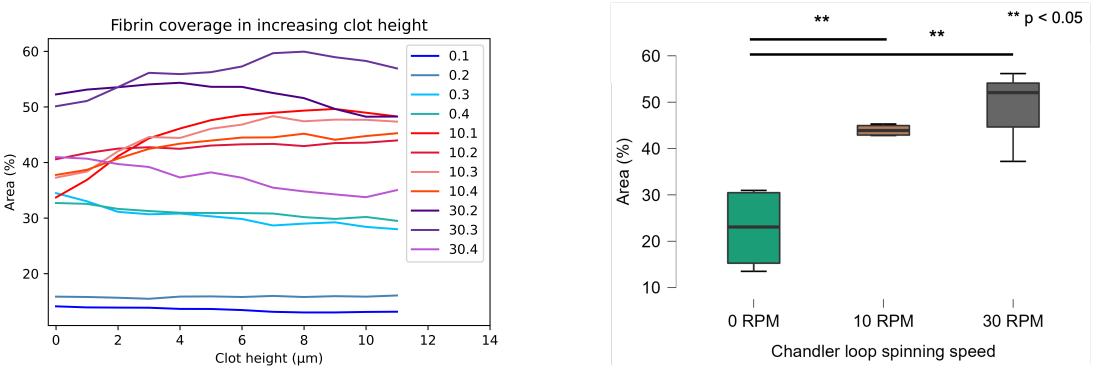

(a) (b)

Figure 3.6: a) The average surface area coverage of the fibrin fibers through the first 11 μm of the thrombus is shown. Of each condition (0, 10 and 30 RPM) four thrombi were imaged and labelled accordingly. Thus the first 0 RPM thrombus was labelled 0.1 and the second 0.2, while the first 10 RPM thrombus was labelled 10.1, etc. The graph shows that the surface area coverage of fibrin fibers has some small fluctuations when imaging deeper in the thrombus. b) Boxplot of the surface area coverage by fibrin fibers. The average density of the fibrin fibers increases in the presence of flow. Both the 10 RPM and 30 RPM have an increased fiber density compared to the 0 RPM (p=0.017 and p=0.007). Between 10 and 30 RPM no statistical difference was found (p=0.323).

3.1.4. Pore size

In addition to the density, the pore size of the samples was extracted from the confocal images. The histograms (Figure 3.7a) show the number and size of the pores found in the thrombi. Both 0 and 10 RPM thrombi had an equal number of stacks processed (n=20), while the 30 RPM had significantly fewer images (n=4) which therefore shows a decreased number of pores compared to the 0 and 10 RPM thrombi. All three histograms show that the bulk of the pores is between 0 and 1 μm. The 0 RPM thrombi have a larger range of pores, which can range up to 5 μm, while the 10 and 30 RPM thrombi range up to 3 μm. The average pore sizes found are 1.4 $\pm$ 0.22 μm, 0.65 $\pm$ 0.010 μm and 0.59 $\pm$ 0.038 μm for 0 RPM, 10 RPM and 30 RPM respectively (Figure 3.7b). The pore size decreases for the thrombi formed in the presence of flow. There is a statistical

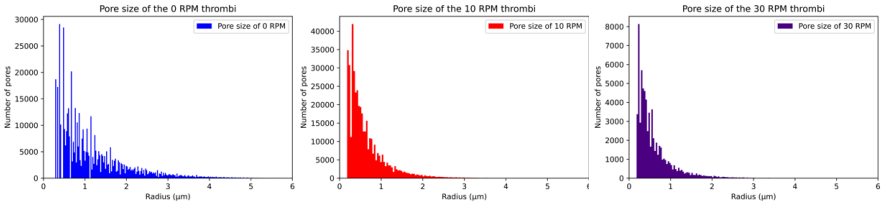

(a)

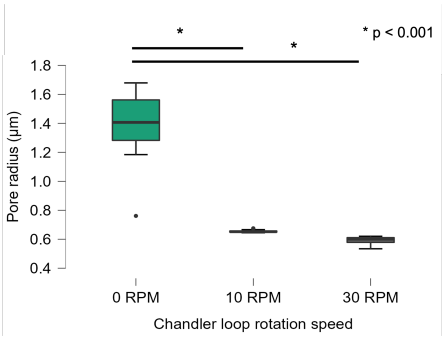

(b)

Figure 3.7: a) Histograms of the frequency at which certain pore sizes were found in the 0, 10 and 30 RPM thrombi. The bulk of the pores lies between 0 and 1 μm for all three shear rates. The 0 RPM thrombi have a larger range of pores, which can range up to 5 μm, while the 10 and 30 RPM thrombi range up to 3 μm. b) Boxplot of the pore sizes found in the thrombi. The average pore sizes found are 1.4 $\pm$ 0.22 μm, 0.65 $\pm$ 0.010 μm and 0.59 $\pm$ 0.038 μm for 0 RPM, 10 RPM and 30 RPM. The pore size decreases in the presence of flow. Both the 10 RPM and 30 RPM have an increased fiber density compared to the 0 RPM ($p < 0.001$ and $p < 0.001$). Between 10 and 30 RPM no statistical difference was found (p=0.132).

difference between the 0 RPM and the 10 and 30 RPM groups ($p < 0.001$ and $p < 0.001$), while no statistical difference was found between 10 and 30 RPM ($p=0.132$).

3.1.5. Compression testing

The thrombus tangent stiffness was calculated from the first 20-40% strain and the last 75-80% strain of the first loading curve during compression testing (Figure 3.8a). The mean tangent stiffness values for all shear rates are shown in Table 3.2. During the compression, all samples from 0, 10 and 30 RPM stiffen for higher strains. Both stiffness ranges showed that the 30 RPM sample had an increased stiffness compared to the 0 and 10 RPM samples (Figures 3.8b and 3.8c). There is a statistical difference between the 30 RPM and both the 0 and 10 RPM groups at the two strain ranges (20-40%, $p = 0.008$ and $p < 0.001$; 75-80%, $p = 0.015$ and $p < 0.001$). No statistical difference was found between 0 and 10 RPM for the 20-40% strain region ($p=0.132$) while for the 75-80% region a statistical difference was found between 0 and 10 RPM ($p=0.025$). The linear fit of these tangent moduli can be found in Appendix F.1.

Multiple compression cycles were recorded to obtain the change in viscous energy dissipation during consecutive loading and unloading cycles. The hysteresis graphs showed that the stress-strain curves for each consecutive cycle are of similar shape and size. An example of a hysteresis stress-strain curve is displayed in

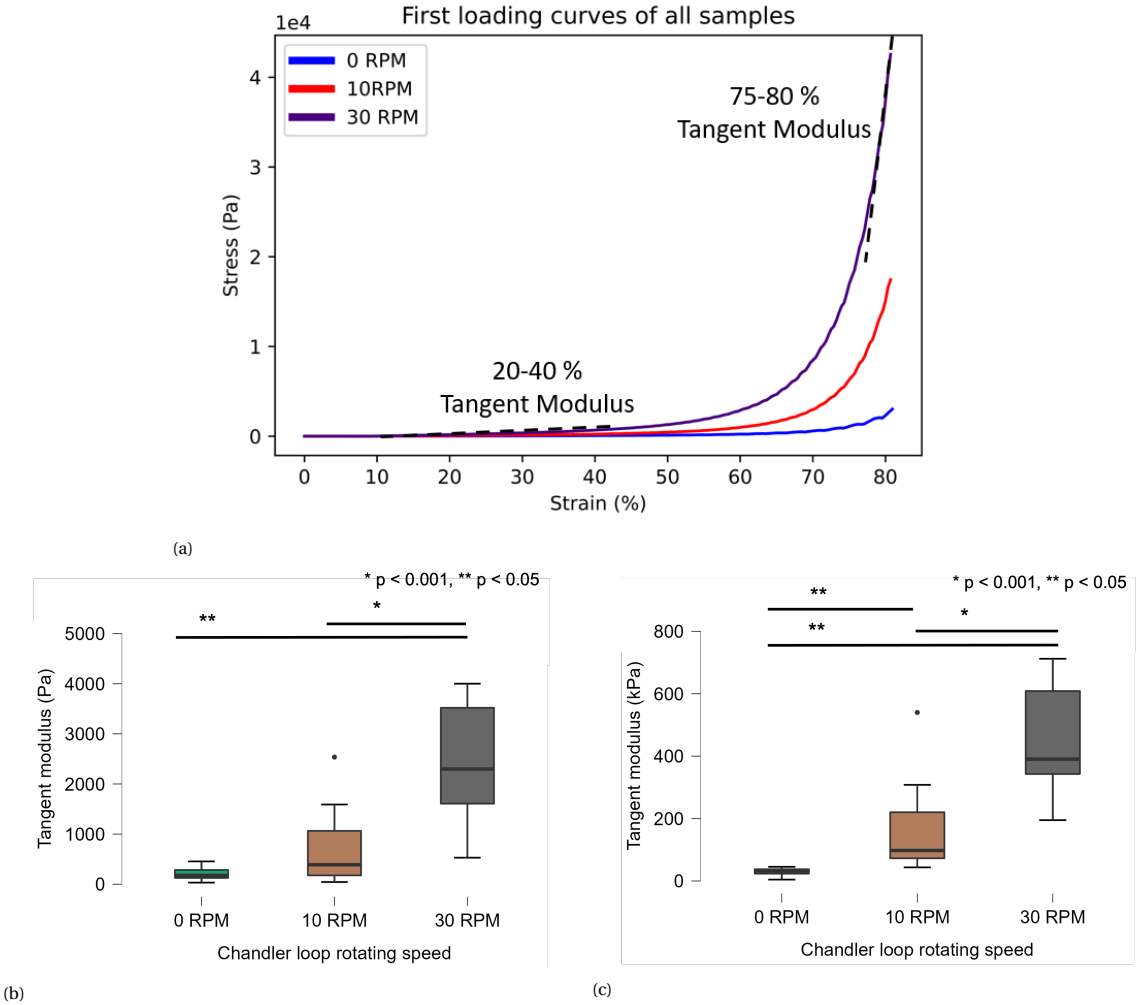

Figure 3.8: a) Representative curve of the first loading curve for the 0, 10 and 30 RPM thrombi. The tangent moduli are computed for 20-40% strain and 75-80% strain. b) The average stiffness moduli of the first 20-40% are 0.21 ± 0.15, 0.77 ± 0.88 and 2.4 ± 1.3 kPa for 0, 10 and 30 RPM, respectively. c) For the last 75-80% the average tangent stiffness moduli are 29 ± 15, $1.8 \times 10^2 \pm 1.7 \times 10^2$ and $4.4 \times 10^2 \pm 1.8 \times 10^2$ kPa for 0, 10 and 30 RPM, respectively. Both stiffness ranges showed that the 30 RPM sample has an increased stiffness compared to the 0 and 10 RPM samples (20-40%, $p = 0.008$ and $p < 0.001$; 75-80%, $p = 0.015$ and $p < 0.001$). No statistical difference was found between 0 and 10 RPM for the 20-40% strain region ($p=0.499$) while for the 75-80% region a statistical difference was found between 0 and 10 RPM ($p=0.025$).

Figure 3.9a, while each individual hysteresis curve can be found in Appendix F.2. After the first loading cycle, the consecutive cycles had a decreased area under the curve indicating changes in the network structure. The area difference between the consecutive curves was small and therefore most changes took place during the first compression. The area decrease per cycle is reported in Appendix F.3. Furthermore, the decrease in viscous energy between the first and final compression was computed (Figure 3.9b). Between the samples no statistical difference ($p = 0.137$, $p = 0.323$ and $p = 0.06$) was found for the amount of viscous energy that was dissipated (Figure 3.9b).

Table 3.2: Mean stiffness values for the first 20-40% and final 75-80% strain.

Rotation speed (RPM)	20-40% Stiffness	75-80% Stiffness
0	0.21 ± 0.15 kPa	29 ± 15 kPa
10	0.77 ± 0.88 kPa	$1.8 \times 10^2 \pm 1.7 \times 10^2$ kPa
30	2.4 ± 1.3 kPa	$4.4 \times 10^2 \pm 1.8 \times 10^2$ kPa

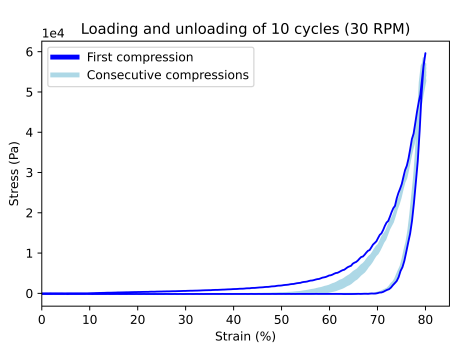

(a)

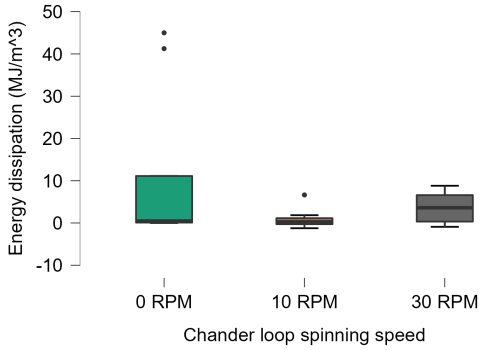

(b)

Figure 3.9: a) Loading and unloading curves of a 30 RPM thrombus. The thrombus was compressed for 10 consecutive cycles, the first cycle is displayed in blue and the nine consecutive cycles in light blue. Due to the similarity of the consecutive cycles individual lines for each cycle cannot be distinguished. b) The decrease in viscous energy between the first and last cycle is due to the dissipation of energy during the consecutive compressions. Between the samples no statistical difference ($p = 0.137$, $p = 0.323$ and $p = 0.06$) in energy dissipation between the first and last cycle was found.

3.1.6. Micro-indention

Micro-indentation, with a cantilever stiffness of 0.40 N/m and tip radius of 103 μm, was done on two 30 RPM samples. Since the 30 RPM samples were the sturdiest and easiest to handle, indentation measurements were started on those samples. On the first sample, three indentations were done and on the second sample six indentations. The difference in indentation attempts was due to troubles during the experiments, which are discussed below. Between indentations, the probe was moved at least twice the diameter of the indenter-tip (206 μm). Before indenting the probe was placed 10 nm above the sample surface, either by hand or with the "find surface" feature in the Chiaro software. Finding the surface of the sample was challenging, as for each indentation the probe was already in contact with the sample. An example of an indentation can be found in Figure 3.10. It shows the loading (blue line), unloading (green line) and the five-second hold (dark blue line) between loading and unloading. During loading and unloading the probe was displaced 15 μm in ten seconds. Furthermore, during indentation noise negatively impacted the

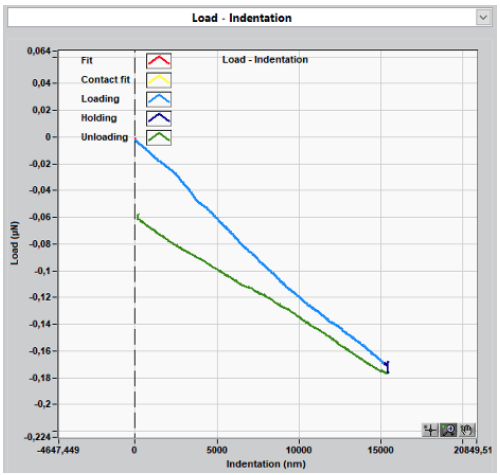

Figure 3.10: Example of an indentation done with the Chiaro micro-indenter. The blue line is the loading curve, which holds after a displacement of 15 μm for five seconds. The green line represents the unloading curve.

recording of the load, making the measurement expendable. Finally, only three indentations were used to calculate the stiffness of the thrombi (Table 3.3). The overall stiffness ranged between 58 and 2.8×10^2 Pa. Within the two indentations on the same sample similar stiffness' were found (i.e. 2.8×10^2 Pa and 2.7×10^2 Pa).

Table 3.3: Mean stiffness values for the Chiaro micro-indentations.

Rotation speed (RPM)	Sample nr.	Indent nr.	Stiffness (Pa)
30	1	1	78
30	2	1	2.8×10^2
30	2	2	2.7×10^2

,

4

Discussion

In this thesis, plasma thrombi formed in the presence and absence of flow were analysed. The thrombi were formed at rotational speeds of 0, 10 and 30 RPM which represent shear rates of roughly 0, 100 and 300 s^{-1}, respectively. With quantification of the micro-structure, i.e fiber thickness, pore size and fiber density, the effects of flow on the fibrin network were investigated. Furthermore, by analysing the mechanical properties of the thrombi, we aimed to link the structural changes in the fibrin network to the elasticity of the thrombus. The results can be summarised in five main findings. Firstly, with the aid of confocal microscopy an increase in fibrin fiber density for thrombi formed in the presence of flow (i.e. flow thrombi) compared to thrombi formed in the absence of flow (i.e. static thrombi), was found. Secondly, the pore size decreased for flow thrombi compared to static thrombi. Thirdly, SEM showed that flow thrombi consist of regions with differences in alignment, fiber density and fiber diameter, while static thrombi are more uniform in nature. Moreover, a decrease in fiber diameter was found for the thrombi formed in the presence of flow. Lastly, unconfined compression testing on the thrombi showed an increase in stiffness for the thrombi formed at 30 RPM (i.e. $\pm$ 300 s^{-1}) compared to 0 and 10 RPM.

Of the three micro-structural properties is the diameter the most popular and often used parameter to describe fibrin networks. In our study, we found fiber diameters of 94 $\pm$ 1.7 nm, 51 $\pm$ 4.1 nm and 54 $\pm$ 4.0 nm for 0, 10 and 30 RPM, respectively. Studies which reported a value for the fiber diameter were interested in the effects of fibrinogen defects on the fibrin network or interested in the effect of factor FXIII, which initiates cross-linking of fibrin fibers [64–69]. Their reported values range between 21 and 400 nm, with Collet et al. reporting different values for coarse, less dense (376 $\pm$ 104 nm) and fine denser thrombi (299 $\pm$ 70 nm) [64]. Furthermore, Abou-Saleh et al. and De Vries et al. reported fiber diameters of 150-200 nm and 200-400 nm, respectively [67, 68]. Both studies report fiber diameter values substantially larger than our findings. Both made use of different imaging techniques (viz. confocal microscopy and atomic force microscopy), which could be an explanation for the difference in values. Wufus et al., Sendeven et al. and Hethersaw et al. all used SEM imaging to determine fiber diameter [65, 66, 69]. Wufus et al. found fiber diameters of 21-24 nm, while Stendeven et al. and Hethershaw et al. found diameters between 74 and 142 nm. All studies were done on statically formed fibrin networks, though Wufus et al. followed a different protocol, by making fibrin gels (i.e. fibrinogen diluted in buffer) instead of networks formed from plasma. Stendeven et al. and Hethershaw et al. both used plasma to form the fibrin networks. This difference could explain the variation in the size of the reported diameters. The fiber diameter of our static thrombi fit with the range reported by Stendeven et al. and Hethersaw et al., which are also the closest to our experimental setup.

Studies by Campbell et al. and Gersh et al. reported fiber diameter for thrombi in the presence of flow [70, 71]. Our study has found that fiber diameter decreases in flow thrombi, which is the exact opposite of Campbell et al.'s outcome. They reported similar fiber diameters for static thrombi, though their reported fiber diameter for flow thrombi was four times as large. Gersh et al.'s outcome is in line with our findings, which were that no significant difference in diameter was found between flow thrombi. Gersh et al. also found significantly larger fiber diameters compared to our study. Campbell et al. formed flow thrombi at low shear rates (0-100 s^{-1}) by perfusing PFP over a tilted coverslip. On the coverslip surface, human dermal fibroblasts were cultured to mimic extravascular TF-bearing cells and thereby triggering the extrinsic pathway of the coagulation cascade. They reported an average diameter value of 79 nm for static thrombi and an increased diameter of 226 nm for flow thrombi. Furthermore, they report morphological differences between

flow and static thrombi. Besides a difference in anisotropy, they report that the network of the flow thrombi consisted of both thick aggregated fibers and a finer network of fibers connecting the thick fibers. Gersh et al.'s study used shear rates of 0, 5 and 20 s^{-1} to form flow thrombi on top of an activated platelet surface. They reported no significant difference in fiber diameter between flow thrombi formed at 5 (210 nm) and 20 s^{-1} (190 nm). No comparison was made with the static control group as those were prepared with the addition of exogenous thrombin, whose concentration is known to influence fiber diameters. Our study, Campbell et al.'s study and Gersh et al.'s study, all use other methods of forming flow thrombi and have different triggers for coagulation. Campbell et al. triggered coagulation with TF, following the extrinsic pathway of the coagulation cascade. Gersh et al. triggered the intrinsic pathway, just like our study, though the network was formed on a layer of activated platelets. These differences may be the reason for the incoherent findings between the studies. Moreover, both Campbell et al. and Gersh et al. manually quantified the fiber diameters while in our study the automatic plugin DiameterJ was used, which does not take into account the coalescence of fibers. The coalesced fibers are treated as branching points and therefore not measured by the plugin, while Campbell et al. clearly state that the coalesced fibers are treated as one thick fiber. Furthermore, a recently published systematic review paper by De Vries et al. also found that DiameterJ underestimates the fiber diameter compared to the manual measurements. The 10 and 30 RPM thrombi having more coalesced fibers compared to the 0 RPM are therefore more subjective to DiameterJ's underestimation of the diameter.

Noted was the similarity of the fiber diameter curves for the 10 and 30 RPM thrombi, which are almost identical. A reason for the similarity in transition points between the three conditions is the way DiameterJ determines the fiber diameters. During the calculation, the distance of the centerline to the fiber edge is converted to a greyscale value. Then DiameterJ counts how often a certain grey value is found and converts the grey value back to diameter values. It then returns the diameter sizes (in nm) and the number of times the diameter is found. This conversion to greyscale is the reason why the curves only have hits for certain diameter values and explains why all three curves have the same transition points.

We found that the density of the flow thrombi increases compared to static thrombi. During the formation of the plasma thrombi in the spinning Chandler loop, it was observed that after fibrin starts to form, it accumulates at the forward meniscus of the loop. The accumulation of fibrin at the forward meniscus was also observed by Gardner et al. in their experiments with WB [30]. Though their formation started with a platelet plug, they report first the formation of fibrin which is then swept towards the forward meniscus. The accumulation of the fibrin compacts the thrombus, decreasing the thrombus in size and increasing its density. When comparing the thrombi size of the static and flow thrombi a clear decrease in size was seen. Therefore, it is hypothesised that the increased density of flow thrombi is caused by thrombus compaction at the forward meniscus of the Chandler loop.

Noted was the large difference in density between the 0 RPM thrombi (Figure 3.6). Two of the thrombi have a surface area coverage of 30%, while the other two are around 15%. When looking at the coverage of each individual stack (Appendix E) the same development can be seen, as for two of the stacks the surface area coverage is around 15% and for the other two around 30%. Such large differences are not seen for 10 RPM, whose coverage lies together closely. A possible explanation for the differences in coverage in the 0 RPM thrombi is the fragility of the thrombi. During cutting the static thrombi were easily deformed and stretched if not handled carefully, while the flow thrombi were more sturdy and less likely to deform during cutting. Stretching of the thrombus could explain the decreased surface area in the 0 RPM thrombi.

Moreover, important to clarify is the reason for changing the imaging settings for the flow thrombi compared to the static thrombi. We hypothesise that due thrombus compaction and a decrease in diameter size of the fibrin fibers resulted in completely saturated images for both 10 and 30 RPM. With the altered settings (viz. increased zoom) the 10 RPM could be clearly visualised, though the 30 RPM images were very hazy and difficult to make. Therefore, the analysis of both the fiber density and the pore size of the network had fewer data points and is less accurate due to the hazy nature of the images. Even though an increase in density was found compared to 0 RPM, we cannot exclude that there is an increase in density between the 10 and 30 RPM as well.

Our findings, which were that pore size decreases in the presence of flow, are in line with the increased density for the flow thrombi, as a denser packed network has less space for pores. Pore size analyses on fibrin networks are often done with SEM imaging or by doing liquid permeation studies [27, 29, 72]. Similar to the fiber density, studies found a decrease in network porosity for thrombi formed at high fibrinogen concentrations and decreased pore sizes in thrombi from stroke and infarction patients. Pore size evaluation with confocal microscopy is not a widely adopted evaluation method. Furthermore, evaluation of both density and pore sizes of flow thrombi is not yet found in literature.

Unconfined compression of both the static and thrombi formed in the presence of flow showed stiffening of the network at higher strains. During compression individual fibrin fibers start to bend in the direction of compression. And as the space between fibers is decreasing, the fibers re-orientate, intertwining the network further. The re-orientation and further entangling of the network make the fibrin harder to deform [73]. Kim et al., who followed the compression of fibrin networks with confocal microscopy, captured the bending and buckling of the fibrin fibers during compression [73]. They found that after buckling of fibers the whole network architecture aligns in a plane normal to the compression direction. Consequently, further compression of the network becomes harder due to entropic resistance to fiber extension. The strain stiffening behaviour described by Kim et al. was also found by Liang et al. and our study [74]. Besides strain-stiffening all thrombi showed a viscoelastic response. The fibrin network consisting of large polymerised fibers shows elastic behaviour in the buckling and bending of fibers which is reversible. The time-dependent part of the compression is caused by the temporary connections between fibers that are pushed into contact. The dissociation of these connections requires energy, which is dissipated. The area between the curves (i.e. the viscous energy dissipation) decreased after the first compression cycle, indicating alterations in the fibrin network. For the remaining nine cycles the viscous energy dissipation stayed roughly the same. Liang et al. also report a decrease in viscous energy dissipation during the first cycle and roughly the same viscous energy dissipations for the consecutive cycles [74]. They found that during the first compression cycle some of the new connections between fibers are not dissociated during unloading. They report that compressed networks have increased crossings and more bundled fibers.

In short, in our study we found that flow changes the structure of a fibrin network. Thrombi formed in the presence of flow (i.e. 10 and 30 RPM) had a decrease in fiber diameter, an increase in fiber density and a decrease in pore size. Between 10 and 30 RPM, no statistical differences were found in the fibrin network structure. With unconfined compression testing an increased stiffness of the 30 RPM thrombi compared to the 0 and 10 RPM thrombi was found. Even though no statistical difference was found in the structure of the flow thrombi, a clear increase in stiffness was found for the 30 RPM thrombi compared to the 10 RPM thrombi. As mentioned before, we cannot exclude that the density of the fibrin networks of 10 and 30 RPM increases, potentially explaining the difference in stiffness between the 10 and 30 RPM thrombi. Furthermore, a large variance between the stiffness measurements was found for the thrombi formed at 10 RPM. As the 10 RPM thrombi got stuck in the Chandler loop during formation, part of the thrombus was formed statically. While only the part of the thrombus that was formed in the presence of flow (i.e. denser head of the 10 RPM thrombi) was used for compression testing, the cessation of fluid flow has impacted the thrombi. Depending on when the thrombus got stuck and thus depending on how long the thrombus was subjected to fluid flow the thrombus' stiffness is different.

To further couple the microscopic features of the fibrin network to the mechanical properties of the thrombus, micro-indentation was performed. Multiple indentations were performed on two 30 RPM samples, which resulted in a total of three stiffness measurements. Two of the three indentations were done on two different positions on the same sample. The measurements being in close range of each other shows promise for the local assessment of mechanical properties of the fibrin network. To properly assess the local stiffness of the thrombi the micro-indentation process needs more exploration and practice. Only a small number of measurements were made due to difficulties with finding the surface and therefore the measured indentations started with the tip of the probe in contact with the sample. The probe used for the Chiaro might have been too stiff to be able to detect a deflection when indenting in the soft sample and therefore missing the first contact with the sample. The softer probes available had a tip radius of 3 μm, which is too small to measure the fibrin network as it would fit between pores potentially measuring between the fibers instead of the network itself. With the inclusion of local stiffness assessments, further coupling of the structural differences and mechanical properties in the fibrin networks is possible.

4.1. Limitations and recommendations

This study has several limitations. Firstly, the flow profile in the Chandler loop changes considerably during thrombus formation. As a large clump is formed in the tubing the flow will adjust and start to flow around the thrombus, changing the flow profile and shear rate. To improve control of the shear rate and also introduce a wider variety of shear rates a tapered flow chamber was designed (Appendix A). With a more controlled and larger range of shear rates, a better distinction between venous and arterial shear rates can be made. As of yet, the plasma thrombi formed in the chamber cannot be removed after formation, making mechanical testing impossible. To improve the adherence of fibrin to the surface of the coverslip, which is the removable

part of the chamber, micro-patterning could be used. By roughening and increasing the surface area more adhesion points could improve fibrin adherence. Furthermore, by coating the micro-patterned surface with, for example platelet receptors or thrombogenic proteins, fibrin adherence could be further improved and at the same time trigger coagulation locally.

Secondly, both imaging techniques are subjected to a bias by the operator. Even though the images were taken at random positions an implicit bias could have impacted the image locations. The implicit bias could be decreased by adding operators who separately image the same sample set. Furthermore, as discussed, the settings of the confocal microscope needed to be altered, to be able to image the thrombi formed in the presence of flow, thereby decreasing the consistency of the experiment. To improve the uniformity of the imaging settings some more preliminary experiments focused on zoom, laser power and concentration of fluorophore could be done. Moreover, the samples used for SEM imaging in this study are separate samples not used in the other analysis methods. This can be improved by dehydrating the disk used for confocal and micro-indentation after these experiments. Even though the thrombi shrink during dehydration, we expect that there will still be enough material left for SEM imaging.

Fourthly, in the calculation of the stress and strain, both the cross-sectional area and the thrombus height are assumed to be constant. While during compression the height of the thrombus decreases after the first cycle, altering both thrombus height and cross-sectional area. To assess how prominent this decrease in initial height is, the disk height after compression could be measured.

Finally, some further recommendations are given. In the present study, the thrombi's stiffness is measured in the direction of flow, while SEM imaging showed fiber alignment and thus anisotropy of the sample. Compression tests perpendicular to the direction of the flow could be added, though there is only limited material available (three disks) for testing. Furthermore, besides using PFP to form thrombi in the Chandler loop, WB and platelet rich plasma (PRP) can be used to see the influence of RBCs and platelets on the fibrin network in both static and flow thrombi. And with the addition of platelets and RBCs the thormbus formation should be carried out at a physiological temperature of 37°C [75]. Moreover, the middle part of the thrombus was used for structural and mechanical analysis, though the tail and the head of the thrombus should be included in the analysis as well. By including the head and tail of the thrombus, the variation in a singular thrombus can also be translated to structural and mechanical differences. Finally, to further expand the structural analysis, the size and frequency of branching points of a fibrin network could be investigated.

5

Conclusion

To summarise, this study assessed the influence of fluid flow on the structure and mechanical response of plasma thrombi. Plasma thrombi were formed in the presence and absence of flow inside the Chandler loop at 0, 10 and 30 RPM to create shear rates of roughly 0, 100 and 300 s^{-1}. An increased fiber diameter was found for the thrombi formed in the presence of flow compared to thrombi formed in the absence of flow. Furthermore, the density increased and the pore size decreased for flow thrombi compared to static thrombi. Lastly, the stiffness of the plasma thrombi was increased for the thrombi formed at 30 RPM compared to 0 and 10 RPM. These findings demonstrate that the fibrin network is structurally and mechanically altered when the thrombi are formed in the presence of flow. With the addition of a tapered flow chamber and the inclusion of local stiffness measurements, thrombi can be formed at a controlled shear rate and structural differences can be coupled mechanical properties on the micro-scale.

Bibliography

[1] "The top 10 causes of death," accessed on 10-02-2021. [Online]. Available: https://www.who.int/news-room/fact-sheets/detail/the-top-10-causes-of-death

[2] A. M. Wendelboe and G. E. Raskob, "Global burden of thrombosis," Circulation Research, vol. 118, no. 9, pp. 1340–1347, Apr. 2016. [Online]. Available: https://doi.org/10.1161/circresaha.115.306841

[3] E. N. Marieb and K. Hoehn, Human Anatomy & Physiology. Pearson Education Limited, 2019.

[4] W. E. Winter, S. D. Flax, and N. S. Harris, "Coagulation testing in the core laboratory," Laboratory Medicine, vol. 48, no. 4, pp. 295–313, Nov. 2017. [Online]. Available: https://doi.org/10.1093/labmed/lmx050

[5] A. J. Gale, "Continuing education course #2: Current understanding of hemostasis," Toxicologic Pathology, vol. 39, no. 1, pp. 273–280, Nov. 2010. [Online]. Available: https://doi.org/10.1177/0192623310389474

[6] R. V. Kruchten, J. M. E. M. Cosemans, and J. W. M. Heemskerk, "Measurement of whole blood thrombus formation using parallel-plate flow chambers – a practical guide," Platelets, vol. 23, no. 3, pp. 229–242, Apr. 2012. [Online]. Available: https://doi.org/10.3109/09537104.2011.630848

[7] K. Broos, H. B. Feys, S. F. D. Meyer, K. Vanhoorelbeke, and H. Deckmyn, "Platelets at work in primary hemostasis," Blood Reviews, vol. 25, no. 4, pp. 155–167, Jul. 2011. [Online]. Available: https://doi.org/10.1016/j.blre.2011.03.002

[8] O. Repetto and V. D. Re, "Coagulation and fibrinolysis in gastric cancer," Annals of the New York Academy of Sciences, vol. 1404, no. 1, pp. 27–48, Aug. 2017. [Online]. Available: https://doi.org/10.1111/nyas.13454

[9] J. Rivera, M. L. Lozano, L. Navarro-Nunez, and V. Vicente, "Platelet receptors and signaling in the dynamics of thrombus formation," Haematologica, vol. 94, no. 5, pp. 700–711, Mar. 2009. [Online]. Available: https://doi.org/10.3324/haematol.2008.003178

[10] S. M. Schoenwaelder, A. Ono, W. S. Nesbitt, J. Lim, K. Jarman, and S. P. Jackson, "Phosphoinositide 3-kinase p110β regulates integrin αIIbβ3 avidity and the cellular transmission of contractile forces," Journal of Biological Chemistry, vol. 285, no. 4, pp. 2886–2896, Jan. 2010. [Online]. Available: https://doi.org/10.1074/jbc.m109.029132

[11] H. H. Versteeg, J. W. M. Heemskerk, M. Levi, and P. H. Reitsma, "New fundamentals in hemostasis," vol. 93, no. 1, pp. 327–358, Jan. 2013. [Online]. Available: https://doi.org/10.1152/physrev.00016.2011

[12] S. Palta, R. Saroa, and A. Palta, "Overview of the coagulation system," Indian Journal of Anaesthesia, vol. 58, no. 5, p. 515, 2014. [Online]. Available: https://doi.org/10.4103/0019-5049.144643

[13] J. W. Weisel and R. I. Litvinov, "Mechanisms of fibrin polymerization and clinical implications," Blood, vol. 121, no. 10, pp. 1712–1719, Mar. 2013. [Online]. Available: https://doi.org/10.1182/blood-2012-09-306639

[14] A. Duttaroy, "Blood coagulation and fibrinolysis." accessed on 08-07-2022. [Online]. Available: https://slideplayer.com/slide/5897692/

[15] A. Kushner, W. P. West, and L. S. Pillarisetty, Virchow Triad, 2nd ed. Treasure Island: StatPearls [Internet].

[16] B. H. Thompson, K. T. Tan, and E. J. van Beek, "Venous thrombosis and pulmonary thromboembolic disease," in Comprehensive Vascular and Endovascular Surgery. Elsevier, 2009, pp. 807–841. [Online]. Available: https://doi.org/10.1016/b978-0-323-05726-4.00049-4

[17] G. Alkarithi, C. Duval, Y. Shi, F. L. Macrae, and R. A. Ariëns, "Thrombus structural composition in cardiovascular disease," Arteriosclerosis, Thrombosis, and Vascular Biology, vol. 41, no. 9, pp. 2370–2383, Sep. 2021.

[18] I. N. Chernysh, C. Nagaswami, S. Kosolapova, A. D. Peshkova, A. Cuker, D. B. Cines, C. L. Cambor, R. I. Litvinov, and J. W. Weisel, "The distinctive structure and composition of arterial and venous thrombi and pulmonary emboli," Scientific Reports, vol. 10, no. 1, Mar. 2020. [Online]. Available: https://doi.org/10.1038/s41598-020-59526-x

[19] J. Zalewski, L. Lewicki, K. Krawczyk, M. Zabczyk, R. Targonski, P. Molek, J. Nessler, and A. Undas, "Polyhedral erythrocytes in intracoronary thrombus and their association with reperfusion in myocardial infarction," Clinical Research in Cardiology, vol. 108, no. 8, pp. 950–962, Feb. 2019. [Online]. Available: https://doi.org/10.1007/s00392-019-01425-x

[20] L. D. Meglio, J.-P. Desilles, V. Ollivier, M. S. Nomenjanahary, S. D. Meglio, C. Deschildre, S. Loyau, J.-M. Olivot, R. Blanc, M. Piotin, M.-C. Bouton, J.-B. Michel, M. Jandrot-Perrus, B. Ho-Tin-Noé, and M. Mazighi, "Acute ischemic stroke thrombi have an outer shell that impairs fibrinolysis," Neurology, vol. 93, no. 18, pp. e1686–e1698, Sep. 2019. [Online]. Available: https://doi.org/10.1212/wnl.0000000000008395

[21] S. Staessens, F. Denorme, O. Francois, L. Desender, T. Dewaele, P. Vanacker, H. Deckmyn, K. Vanhoorelbeke, T. Andersson, and S. F. D. Meyer, "Structural analysis of ischemic stroke thrombi: histological indications for therapy resistance," Haematologica, vol. 105, no. 2, pp. 498–507, May 2019. [Online]. Available: https://doi.org/10.3324/haematol.2019.219881

[22] H. Hund, N. Boodt, N. A. Terreros, A. Taha, H. A. Marquering, A. C. G. M. van Es, R. P. H. Bokkers, G. J. L. à Nijeholt, C. B. Majoie, D. W. Dippel, H. F. Lingsma, H. M. M. van Beusekom, and A. van der Lugt and, "Quantitative thrombus characteristics on thin-slice computed tomography improve prediction of thrombus histopathology: results of the MR CLEAN registry," European Radiology, Apr. 2022. [Online]. Available: https://doi.org/10.1007/s00330-022-08762-y

[23] R. Cahalane, N. Boodt, A. C. Akyildiz, J. anne Giezen, M. Mondeel, A. van der Lugt, H. Marquering, and F. Gijsen, "A review on the association of thrombus composition with mechanical and radiological imaging characteristics in acute ischemic stroke," Journal of Biomechanics, vol. 129, p. 110816, Dec. 2021. [Online]. Available: https://doi.org/10.1016/j.jbiomech.2021.110816

[24] P. Jolugbo and R. A. Ariëns, "Thrombus composition and efficacy of thrombolysis and thrombectomy in acute ischemic stroke," Stroke, vol. 52, no. 3, pp. 1131–1142, Mar. 2021. [Online]. Available: https://doi.org/10.1161/strokeaha.120.032810

[25] A. Chandrashekar, G. Singh, J. Garry, N. Sikalas, and N. Labropoulos, "Mechanical and biochemical role of fibrin within a venous thrombus," European Journal of Vascular and Endovascular Surgery, vol. 55, no. 3, pp. 417–424, Mar. 2018. [Online]. Available: https://doi.org/10.1016/j.ejvs.2017.12.002

[26] A. Undas and R. A. Ariëns, "Fibrin clot structure and function," Arteriosclerosis, Thrombosis, and Vascular Biology, vol. 31, no. 12, Dec. 2011. [Online]. Available: https://doi.org/10.1161/atvbaha.111.230631

[27] A. Daraei, M. Pieters, S. R. Baker, Z. de Lange-Loots, A. Siniarski, R. I. Litvinov, C. S. B. Veen, M. P. M. de Maat, J. W. Weisel, R. A. S. Ariëns, and M. Guthold, "Automated fiber diameter and porosity measurements of plasma clots in scanning electron microscopy images," Biomolecules, vol. 11, no. 10, p. 1536, Oct. 2021. [Online]. Available: https://doi.org/10.3390/biom11101536

[28] A. Undas, "Fibrin clot properties and their modulation in thrombotic disorders," Thrombosis and Haemostasis, vol. 112, no. 07, pp. 32–42, 2014. [Online]. Available: https://doi.org/10.1160/th14-01-0032

[29] B. Blombäck, K. Carlsson, B. Hessel, A. Liljeborg, R. Procyk, and N. Åslund, "Native fibrin gel networks observed by 3d microscopy, permeation and turbidity," Biochimica et Biophysica Acta (BBA) - Protein Structure and Molecular Enzymology, vol. 997, no. 1-2, pp. 96–110, Jul. 1989. [Online]. Available: https://doi.org/10.1016/0167-4838(89)90140-4

[30] R. A. Gardner, “An examination of the fluid mechanics and thrombus formation time parameters in a chandler rotating loop system,” J. Lab. Clin. Med., vol. 84, no. 4, pp. 494–508, Oct. 1974.

[31] H. Engelberg, “Studies with the chandler rotating loop. evidence that thrombin generation is responsible for the formation of the artificial in vitro thrombi,” Thromb. Diath. Haemorrh., vol. 22, no. 2, pp. 344–350, Nov. 1969.

[32] I. Provenzale, S. L. N. Brouns, P. E. J. van der Meijden, F. Swieringa, and J. W. M. Heemskerk, “Whole blood based multiparameter assessment of thrombus formation in standard microfluidic devices to proxy in vivo haemostasis and thrombosis,” Micromachines, vol. 10, no. 11, p. 787, Nov. 2019. [Online]. Available: https://doi.org/10.3390/mi10110787

[33] F. Swieringa, C. C. Baaten, R. Verdoold, T. G. Mastenbroek, N. Rijnveld, K. O. van der Laan, E. J. Breel, P. W. Collins, M. D. Lancé, Y. M. Henskens, J. M. Cosemans, J. W. Heemskerk, and P. E. van der Meijden, “Platelet control of fibrin distribution and microelasticity in thrombus formation under flow,” Arteriosclerosis, Thrombosis, and Vascular Biology, vol. 36, no. 4, pp. 692–699, Apr. 2016. [Online]. Available: https://doi.org/10.1161/atvbaha.115.306537

[34] A. B. Chandler, “In vitro thrombotic coagulation of the blood; a method for producing a thrombus,” Lab. Invest., vol. 7, no. 2, pp. 110–114, Mar. 1958.

[35] H. A. Stringer, P. van Swieten, H. F. Heijnen, J. J. Sixma, and H. Pannekoek, “Plasminogen activator inhibitor-1 released from activated platelets plays a key role in thrombolysis resistance. studies with thrombi generated in the chandler loop.” Arteriosclerosis and Thrombosis: A Journal of Vascular Biology, vol. 14, no. 9, pp. 1452–1458, Sep. 1994. [Online]. Available: https://doi.org/10.1161/01.atv.14.9.1452

[36] L. A. Robbie, S. P. Young, B. Bennett, and N. A. Booth, “Thrombi formed in a chandler loop mimic human arterial thrombi in structure and RAI-1 content and distribution,” Thromb. Haemost., vol. 77, no. 3, pp. 510–515, Mar. 1997.

[37] K. S. Sakariassen, L. Orning, and V. T. Turitto, “The impact of blood shear rate on arterial thrombus formation,” Future Science OA, vol. 1, no. 4, Nov. 2015. [Online]. Available: https://doi.org/10.4155/fso.15.28

[38] S. Gogia and S. Neelamegham, “Role of fluid shear stress in regulating VWF structure, function and related blood disorders,” Biorheology, vol. 52, no. 5-6, pp. 319–335, Feb. 2016. [Online]. Available: https://doi.org/10.3233/bir-15061

[39] N. Boodt, P. R. S. van Schauburg, H. M. Hund, B. Fereidoonnezhad, J. P. McGarry, A. C. Akyildiz, A. C. van Es, S. F. D. Meyer, D. W. Dippel, H. F. Lingsma, H. M. van Beusekom, A. van der Lugt, and F. J. Gijsen, “Mechanical characterization of thrombi retrieved with endovascular thrombectomy in patients with acute ischemic stroke,” Stroke, vol. 52, no. 8, pp. 2510–2517, Aug. 2021. [Online]. Available: https://doi.org/10.1161/strokeaha.120.033527

[40] W. Li, J. Feng, Y. Wang, Q. Shi, G. Ma, S. Aglyamov, K. V. Larin, G. Lan, and M. Twa, “Micron-scale hysteresis measurement using dynamic optical coherence elastography,” Biomed. Opt. Express, vol. 13, no. 5, pp. 3021–3041, May 2022. [Online]. Available: http://opg.optica.org/boe/abstract.cfm?URI=boe-13-5-3021

[41] N. Antonovaite, M. Berardi, K. Bielawski, and N. Rijnveld, “Fiber-optics based nanoindenters for studying the mechanics of diseases,” 2020. [Online]. Available: http://rgdoi.net/10.13140/RG.2.2.19720.85761

[42] D. Chavan, T. C. van de Watering, G. Gruca, J. H. Rector, K. Heeck, M. Slaman, and D. Iannuzzi, “Ferrule-top nanoindenter: An optomechanical fiber sensor for nanoindentation,” Review of Scientific Instruments, vol. 83, no. 11, p. 115110, Nov. 2012. [Online]. Available: https://doi.org/10.1063/1.4766959

[43] “Piuma nanoindenter: User manual,” 2020, accessed on 02-06-2021. [Online]. Available: https://www.optics11life.com/wp-content/uploads/2020/10/Piuma-user-manual-v3.4.pdf

[44] S. V. Beekmans and D. Iannuzzi, "A metrological approach for the calibration of force transducers with interferometric readout," Surface Topography: Metrology and Properties, vol. 3, no. 2, p. 025004, Apr. 2015. [Online]. Available: https://doi.org/10.1088/2051-672x/3/2/025004

[45] "Piuma nanoindenter: User manual," 2016, accessed on 3-06-2021.

[46] S. V. Beekmans and D. Iannuzzi, "Characterizing tissue stiffness at the tip of a rigid needle using an opto-mechanical force sensor," Biomedical Microdevices, vol. 18, no. 1, Feb. 2016. [Online]. Available: https://doi.org/10.1007/s10544-016-0039-1

[47] J. Field and M. Swain, "A simple predictive model for spherical indentation," Journal of Materials Research, vol. 8, no. 2, pp. 297–306, Feb. 1993. [Online]. Available: https://doi.org/10.1557/jmr.1993.0297

[48] "Pythagorean theorem," accessed on 15-06-2021. [Online]. Available: https://mathworld.wolfram.com/PythagoreanTheorem.html

[49] "Bestand:spherical cap.svg," accessed on 15-06-2021. [Online]. Available: https://nl.m.wikipedia.org/wiki/Bestand:Spherical_Cap.svg

[50] C. L. Chiu, V. Hecht, H. Duong, B. Wu, and B. Tawil, "Permeability of three-dimensional fibrin constructs corresponds to fibrinogen and thrombin concentrations," BioResearch Open Access, vol. 1, no. 1, pp. 34–40, Feb. 2012. [Online]. Available: https://doi.org/10.1089/biores.2012.0211

[51] O. Moreno-Arotzena, J. Meier, C. del Amo, and J. García-Aznar, "Characterization of fibrin and collagen gels for engineering wound healing models," Materials, vol. 8, no. 4, pp. 1636–1651, Apr. 2015. [Online]. Available: https://doi.org/10.3390/ma8041636

[52] B. Hochreiter, A. Pardo-Garcia, and J. Schmid, "Fluorescent proteins as genetically encoded FRET biosensors in life sciences," Sensors, vol. 15, no. 10, pp. 26 281–26 314, Oct. 2015. [Online]. Available: https://doi.org/10.3390/s151026281

[53] A. D. Elliott, "Confocal microscopy: Principles and modern practices," Current Protocols in Cytometry, vol. 92, no. 1, Dec. 2019. [Online]. Available: https://doi.org/10.1002/cpcy.68

[54] "Cf dyes. what started it all? part 2. the chemistry of fluorescence," accessed on 22-11-2021. [Online]. Available: https://biotium.com/blog/cf-dyes-what-started-it-all-part-2-the-chemistry-of-fluorescence/

[55] M. Ahn, T. Kim, H. Yoo, I. Song, and D. Gweon, "Simultaneous imaging of confocal fluorescence and raman spectrum," in Confocal, Multiphoton, and Nonlinear Microscopic Imaging III, T. Wilson and A. Periasamy, Eds. SPIE, Jul. 2007. [Online]. Available: https://doi.org/10.1117/12.726688

[56] M. Tare, O. Puli, and A. Singh, "Drosophila adult eye model to teach scanning electron microscopy in an undergraduate cell biology laboratory." Population Data Information Service, pp. 174–180, Jan. 2009. [Online]. Available: https://doi.org/10.1161/01.atv.14.9.1452

[57] SciMed, "A brief introduction to sem (scanning electron microscopy)," accessed on 22-07-2022. [Online]. Available: https://www.scimed.co.uk/education/sem-scanning-electron-microscopy/

[58] N. S. Instruments, "Scanning electron microscopy," accessed on 22-07-2022. [Online]. Available: https://www.nanoscience.com/techniques/scanning-electron-microscopy/#:~:text=A%20scanning%20electron%20microscope%20(SEM,the%20surface's%20topography%20and%20composition.

[59] Microscopewiki, "Scanning electron microscope (sem)," accessed on 22-07-2022. [Online]. Available: https://microscopewiki.com/scanning-electron-microscope/

[60] M. Molteni, D. Magatti, B. Cardinali, M. Rocco, and F. Ferri, "Fast two-dimensional bubble analysis of biopolymer filamentous networks pore size from confocal microscopy thin data stacks," Biophysical Journal, vol. 104, no. 5, pp. 1160–1169, Mar. 2013. [Online]. Available: https://doi.org/10.1016/j.bpj.2013.01.016

[61] S. Münster and B. Fabry, "A simplified implementation of the bubble analysis of biopolymer network pores," Biophysical Journal, vol. 104, no. 12, pp. 2774–2775, Jun. 2013. [Online]. Available: https://doi.org/10.1016/j.bpj.2013.05.016

[62] N. A. Hotaling, K. Bharti, H. Kriel, and C. G. Simon, "DiameterJ: A validated open source nanofiber diameter measurement tool," Biomaterials, vol. 61, pp. 327–338, Aug. 2015. [Online]. Available: https://doi.org/10.1016/j.biomaterials.2015.05.015

[63] J. G. Yoon and J. Song, "Adopting automated image analysis tool for fibrin network: Can we obtain clot properties for practical application?" International Journal of Laboratory Hematology, vol. 39, no. 5, pp. e121–e123, May 2017. [Online]. Available: https://doi.org/10.1111/ijlh.12689

[64] J. P. Collet, D. Park, C. Lesty, J. Soria, C. Soria, G. Montalescot, and J. W. Weisel, "Influence of fibrin network conformation and fibrin fiber diameter on fibrinolysis speed," Arteriosclerosis, Thrombosis, and Vascular Biology, vol. 20, no. 5, pp. 1354–1361, May 2000. [Online]. Available: https://doi.org/10.1161/01.atv.20.5.1354

[65] K. F. Standeven, P. J. Grant, A. M. Carter, T. Scheiner, J. W. Weisel, and R. A. Ariëns, "Functional analysis of the fibrinogen aα thr312ala polymorphism," Circulation, vol. 107, no. 18, pp. 2326–2330, May 2003. [Online]. Available: https://doi.org/10.1161/01.cir.0000066690.89407.ce

[66] E. L. Hethershaw, A. L. C. L. Corte, C. Duval, M. Ali, P. J. Grant, R. A. S. Ariëns, and H. Philippou, "The effect of blood coagulation factor XIII on fibrin clot structure and fibrinolysis," Journal of Thrombosis and Haemostasis, vol. 12, no. 2, pp. 197–205, Feb. 2014. [Online]. Available: https://doi.org/10.1111/jth.12455

[67] R. H. Abou-Saleh, S. D. Connell, R. Harrand, R. A. Ajjan, M. W. Mosesson, D. A. M. Smith, P. J. Grant, and R. A. Ariëns, "Nanoscale probing reveals that reduced stiffness of clots from fibrinogen lacking 42 n-terminal bβ-chain residues is due to the formation of abnormal oligomers," Biophysical Journal, vol. 96, no. 6, pp. 2415–2427, Mar. 2009. [Online]. Available: https://doi.org/10.1016/j.bpj.2008.12.3913

[68] J. J. de Vries, D. Laan, F. Frey, G. H. Koenderink, and M. P. de Maat, "A systematic review and comparison of automated tools for quantification of fibrous networks," Sep. 2022. [Online]. Available: https://doi.org/10.1101/2022.09.08.507154

[69] A. Wufsus, N. Macera, and K. Neeves, "The hydraulic permeability of blood clots as a function of fibrin and platelet density," Biophysical Journal, vol. 104, no. 8, pp. 1812–1823, Apr. 2013. [Online]. Available: https://doi.org/10.1016/j.bpj.2013.02.055

[70] R. A. Campbell, M. M. Aleman, L. D. Gray, M. R. Falvo, and A. S. Wolberg, "Flow profoundly influences fibrin network structure: Implications for fibrin formation and clot stability in haemostasis," Thrombosis and Haemostasis, vol. 104, no. 12, pp. 1281–1284, 2010. [Online]. Available: https://doi.org/10.1160/th10-07-0442

[71] K. C. Gersh, K. E. Edmondson, and J. W. Weisel, "Flow rate and fibrin fiber alignment," Journal of Thrombosis and Haemostasis, vol. 8, no. 12, pp. 2826–2828, Dec. 2010. [Online]. Available: https://doi.org/10.1111/j.1538-7836.2010.04118.x

[72] E. J. Dunn, R. A. Ariëns, M. de Lange, H. Snieder, J. H. Turney, T. D. Spector, and P. J. Grant, "Genetics of fibrin clot structure: a twin study," Blood, vol. 103, no. 5, pp. 1735–1740, Mar. 2004. [Online]. Available: https://doi.org/10.1182/blood-2003-07-2247

[73] O. V. Kim, R. I. Litvinov, J. W. Weisel, and M. S. Alber, "Structural basis for the nonlinear mechanics of fibrin networks under compression," Biomaterials, vol. 35, no. 25, pp. 6739–6749, Aug. 2014. [Online]. Available: https://doi.org/10.1016/j.biomaterials.2014.04.056

[74] X. Liang, I. Chernysh, P. K. Purohit, and J. W. Weisel, "Phase transitions during compression and decompression of clots from platelet-poor plasma, platelet-rich plasma and whole blood," Acta Biomaterialia, vol. 60, pp. 275–290, Sep. 2017. [Online]. Available: https://doi.org/10.1016/j.actbio.2017.07.011

[75] L. Herfs, F. Swieringa, N. Jooss, M. Kozlowski, F. C. Heubel-Moenen, R. van Oerle, P. Machiels, Y. Henskens, and J. W. Heemskerk, "Multiparameter microfluidics assay of thrombus formation reveals increased sensitivity to contraction and antiplatelet agents at physiological temperature," Thrombosis Research, vol. 203, pp. 46–56, Jul. 2021. [Online]. Available: https://doi.org/10.1016/j.thromres.2021.04.014

[76] T. Sochi, "Non-newtonian rheology in blood circulation," juni 2014. [Online]. Available: https://arxiv.org/pdf/1306.2067.pdf#:~:text=While%20the%20plasma%20is%20essentially,viscoelasticity%2C%20yield%20stress%20and%20thixotropy.

[77] H. Bruus, Theoretical Microfluidics, ser. Oxford Master Series in Physics. London, England: Oxford University Press, Nov. 2007.

[78] M. Rossi, R. Lindken, B. P. Hierck, and J. Westerweel, "Tapered microfluidic chip for the study of biochemical and mechanical response at subcellular level of endothelial cells to shear flow," Lab on a Chip, vol. 9, no. 10, p. 1403, 2009. [Online]. Available: https://doi.orer/10.1039/b822270n

[79] T. V. Colace, G. W. Tormoen, O. J. McCarty, and S. L. Diamond, "Microfluidics and coagulation biology," Annual Review of Biomedical Engineering, vol. 15, no. 1, pp. 283–303, Jul. 2013. [Online]. Available: https://doi.org/10.1146/annurev-bioeng-071812-152406

[80] R. G. Bacabac, T. H. Smit, S. C. Cowin, J. J. V. Loon, F. T. Nieuwstadt, R. Heethaar, and J. Klein-Nulend, "Dynamic shear stress in parallel-plate flow chambers," Journal of Biomechanics, vol. 38, no. 1, pp. 159–167, Jan. 2005. [Online]. Available: https://doi.org/10.1016/j.jbiomech.2004.03.020

[81] Studyguide for fundamentals of heat and mass transfer by incropera, Frank P., ISBN 9780470501979. Cram101, Jul. 2012.

[82] B. Rehm, D. Consultant, A. Haghshenas, A. S. Paknejad, and J. Schubert, "Situational problems in MPD," in Managed Pressure Drilling. Elsevier, 2008, pp. 39–80. [Online]. Available: https://doi.org/10.1016/b978-1-933762-24-1.50008-5

[83] B. Guo and A. Ghalambor, "Transportation," in Natural Gas Engineering Handbook. Elsevier, 2005, pp. 219–262. [Online]. Available: https://doi.org/10.1016/b978-1-933762-41-8.50018-6

[84] N. Westerhof, N. Stergiopulos, M. I. M. Noble, and B. E. Westerhof, "Turbulence," in Snapshots of Hemodynamics. Springer International Publishing, Sep. 2018, pp. 23–25. [Online]. Available: https://doi.org/10.1007/978-3-319-91932-4_4

[85] T. V. Colace, J. Jobson, and S. L. Diamond, "Relipidated tissue factor linked to collagen surfaces potentiates platelet adhesion and fibrin formation in a microfluidic model of vessel injury," Bioconjugate Chemistry, vol. 22, no. 10, pp. 2104–2109, Sep. 2011. [Online]. Available: https://doi.org/10.1021/bc200326v

[86] S. M. de Witt, F. Swieringa, R. Cavill, M. M. E. Lamers, R. van Kruchten, T. Mastenbroek, C. Baaten, S. Coort, N. Pugh, A. Schulz, I. Scharrer, K. Jurk, B. Zieger, K. J. Clemetson, R. W. Farndale, J. W. M. Heemskerk, and J. M. Cosemans, "Identification of platelet function defects by multi-parameter assessment of thrombus formation," Nature Communications, vol. 5, no. 1, Jul. 2014. [Online]. Available: https://doi.org/10.1038/ncomms5257

A

Appendix: Tapered flow chamber

To follow the formation of thrombi in the presence of flow, with a more controlled way of inducing a shear rate and a larger range of shear rates, a tapered flow chamber was designed. In this Appendix the design of the flow chamber and the preliminary experiments done with the flow chamber are discussed.

A.1. Design of the tapered flow chamber

Parallel plate flow chambers are a recognised and well-established method of visualising haemostatic and thrombus dynamics. They are able to control hemodynamic conditions by mimicking in vivo blood flow, while only requiring small volumes of blood [32]. Presently, parallel plate flow chambers are linear in shape and require multiple flow rates and thus multiple experiments to establish various shear rates. A tapered flow chamber, in which thrombus formation has not been studied yet, will allow for thrombus formation with a single flow rate and thus a single experiment. This will significantly reduce the analytical variation between the various shear rates, as inadvertent differences during the preparation of the plasma and during the setup of the device are eliminated. In this section, the rheology of parallel plate flow chambers and the design of the tapered parallel plate flow chamber will be discussed.

Blood, the fluid pumped through the circulatory system of humans, is usually referred to as whole blood in biomedical sciences. Whole blood, consisting of RBCs, while blood cells (WBCs) and platelets, behave as a non-Newtonian fluid due to the high concentration of RBCs. Aggregate formation and elasticity of the RBCs are responsible for the non-Newtonian behaviour. With the removal of RBCs, the remaining blood plasma can be described as a Newtonian fluid [76]. In a Newtonian fluid, the viscosity is independent of the shear rate and there is a linear relationship between shear stress and shear rate, shown in Equation A.1:

$$\tau = \eta \gamma, \tag{A.1}$$

in which the shear stress (τ) is given in Pa, the viscosity in (η) in Pa s and the shear rate (γ) in s^{-1}. The motion of viscous fluids are described by the non-linear differential equation of Navier-Stokes. The equation has analytical solutions for multiple cases, one being the Poiseuille flow. The Poiseuille flow is a pressure-driven, steady-state laminar fluid flow of a Newtonian fluid in a long channel. By imposing a pressure difference between the inlet and outlet, a fluid flow is guided through the channel [77]. The fluid flow in parallel plate flow chambers being laminar in nature, due to the small size of the chambers, allows for the use of the analytical solution of the Poiseuille flow to model the velocity profile and shear stress in the flow chamber.

Parallel plate flow chambers with a large width-to-height ratio can be modelled as two infinitely large parallel plates [77, 78]. This reduces the laminar velocity profile to a simple parabola, shown in Equation A.2:

$$v(z) = \frac{\Delta P}{2\eta L}(h - z)\, z, \tag{A.2}$$

in which the velocity (v) is given in m/s, the pressure difference (ΔP) in Pa and the chamber length (L), height (h) and distance from the lower chamber wall (z) in m. With computation of the pressure difference with Equation A.3, the velocity profile for various widths of a parallel plate flow chamber can be visualised (Figure A.1).

$$\Delta P = \frac{12\,Q\,\eta\,L}{h^2\,w}, \tag{A.3}$$

in which the flow rate (Q) is given in m^3/s.

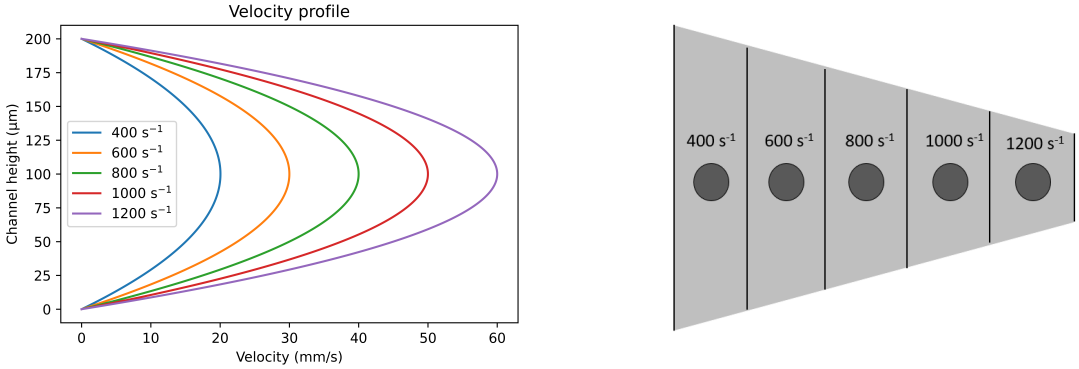

Figure A.1: a) Velocity profiles in the tapered parallel plate flow chamber at the position of the five micro-spots applied in the flow chamber. b) Visualisation of the five micro-spots inside a tapered parallel plate flow chamber, corresponding to the flow profiles in a.

The flow and shear conditions inside the flow chamber are controlled by the infusion rate (i.e. flow rate) and the chamber geometry [79]. The shear stress is given in Equation A.4:

$$\tau_w = \frac{6\,\eta\,Q}{w\,h^2}. \tag{A.4}$$

By combining Equation A.1 and Equation A.4 the shear stress can be converted into shear rates (Equation A.5):

$$\gamma = \frac{6\,Q}{w\,h^2}, \tag{A.5}$$

which will be used to classify the shear rate of the positions of the micro-spots inside the flow chamber throughout this thesis [78, 80].

The design of the tapered flow chamber (Figure A.1b) has been based on a parallel plate flow chamber (Maastricht flow chamber), designed by Maastricht Instruments and on the tapered microfluidic chip designed by Rossi et al. [32, 78]. The former consists of a rectangular duct engraved in a block made of polymethyl methacrylate (PMMA), which is closed by clamping a coverslip on the bottom of the block. The latter uses a rubber gasket with the shape of the duct, which is placed between a glass slide and a PMMA top. The glass coverslip in both chambers allows for visualisation of the inside of the flow chamber during experiments. The tapered parallel plate flow chamber used in this thesis is engraved in a PMMA block and will be clamped on a coverslip. The dimensions of the tapered duct are based on the following conditions:

- width of the duct cannot exceed or be too close to the borders of the glass coverslip
- length of the duct needs to fit five shear regions
- shear rate regions covers the shear rate in veins (15 - 200 s^{-1}), large arteries (300 - 800 s^{-1}) and in arterioles (450 - 1,600 s^{-1}) [37, 38]
- width to height ratio has to exceed 10 to allow for a quasi-two-dimensional flow [79]
- height of the duct has to minimise the increase of shear rate during thrombus growth but still be low enough to minimize the volume of fluid needed during an experiment

With regard to all these conditions the following dimensions were used for the duct: length 20 mm, height 200 μm, entrance width 2.89 mm and exit width 12.5 mm (Figure A.2). The chosen height of the duct allows for thrombus growth of 10 μm, with a maximum shear rate increase of 10%, while also only requiring 7.5 mL of plasma for 5 minutes of perfusion. Decreasing the height further would decrease the required volume of plasma, but would also significantly increase the shear rate change when a thrombus is formed in the

chamber. While increasing the chamber height would decrease the effect of the thrombus growth on the flow rate, it would also significantly increase the volume of plasma required for perfusion. Therefore, the chosen height of 200 μm was deemed optimal.

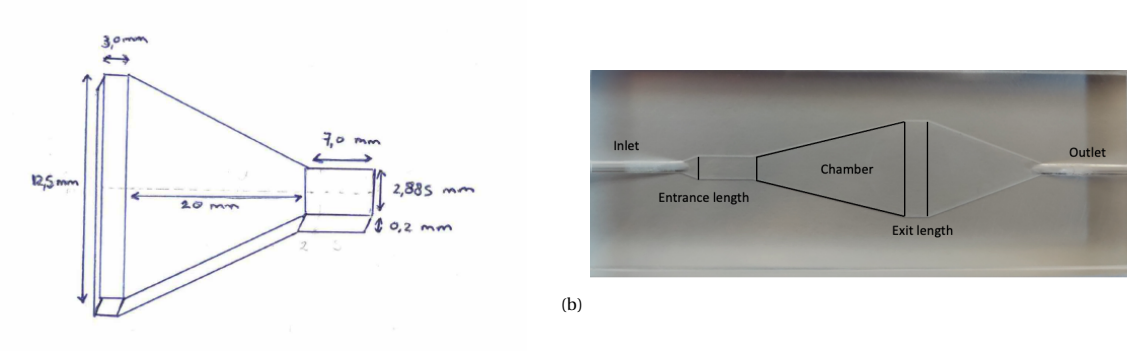

(a) (b)

Figure A.2: a) Sketch of the tapered duct which is engraved into the PMMA block. b) The tapered flow chamber duct engraved inside a PMMA block.

To make sure that the flow inside the tapered duct is fully developed laminar flow, rectangular ducts are added. The required length can be computed with Equation A.6:

$$L_{ent} = 0.0575\, R_e\, D_h, \tag{A.6}$$

in which the Re is the dimensionless Reynolds number and the D_h the hydraulic diameter of the duct [81]. The Reynolds number and the hydraulic diameter, which transforms non-circular ducts to an equivalent diameter of a square duct, are computed by Equations A.7 and A.8, respectively.

$$Re = \frac{\rho\, v\, D_h}{\eta}, \tag{A.7}$$

$$D_h = \frac{2\, w\, h}{w + h}, \tag{A.8}$$

in which ρ is the density (kg/m^3), v the fluid velocity m/s, η the viscosity kg/(ms) and the width (w) and height (h) are both given in m. The minimal entrance length found with Equation A.6 was 0.3 mm, but to be sure that flow is developed an entrance length of 7 mm and an exit length of 3 mm were taken, based on the report of Rossi et al. [78].

The Reynolds number (Equation A.7), which is the ratio of inertial forces to viscous forces is used to determine whether a flow is turbulent or laminar [82, 83]. As the blood flow in healthy vessels is laminar, the flow inside the flow chamber should be laminar as well, which means that the Reynolds number should not exceed 2200 [84]. The Reynolds number for the parallel flow chamber ranges between 2.7 and 11, thus is laminar throughout the whole chamber.

An important part of studying the thrombus formation in the tapered flow chamber is the adherence of the thrombus to the glass coverslip. Through this coverslip the thrombus is imaged during formation and after perfusion, the coverslip can be removed from the flow chamber to further investigate the thrombus. A technique to selectively adhere thrombi to the surface of a flow chamber is micropatterning. Micro-spots or stripes of thrombogenic protein generate distinct regions in microfluidic channels, both preventing early on triggering and making sure the thrombi form at the regions of interest [85, 86]. To solely study the formation of the fibrin network under dynamic conditions, experiments with PFP are needed. However, as the platelets are excluded, the collagen will no longer function as a thrombogenic surface and as scaffolds for the thrombus to form on and hold onto. Preliminary experiments with collagen, TF, fibrinogen and fibrin surfaces were done, to find an appropriate scaffold for fibrin thrombi to adhere to. Below the details of the preliminary experiments done with the chamber are explained. Unfortunately, none of the experiments were satisfactory and as of yet the plasma thrombi cannot be removed from the flow chamber. Therefore, no measurements of the fiber thickness, pore size or micro-elasticity could be taken.

A.2. Preliminary experiments: Thrombus removal

To be able to do micro-indentation on fibrin thrombi, they need to be removed from the flow chamber. Since sticking the thrombus to the chamber will disrupt the structure of the fibrin during removal, multiple tests were done in a parallel plate flow chamber to allow for thrombus removal.

Firstly, micro-spots with 6 pM tissue factor were made by pipetting 1 μL on top of the coverslip. When left to dry, 5 consecutive spots were observed. PFP mixed with fibrinogen labelled Alexafluor 488 (0.025 mg/ml) was perfused over the tissue factor spots at 100 s^{-1}. At both shear rates coagulation was triggered and filled the whole chamber with fibrin, instead of selectively forming fibrin on the surface of the coverslip. When removing the coverslip the fibrin was stuck to the chamber and could not be removed without disruption of the network. As perfusion at 100 s^{-1} is a very low perfusion speed the Peclet number, which is the ratio of convective and diffusive transport, was estimated. As the Peclet number was close to 1, a shear rate of 500 s^{-1} was chosen for the remainder of the experiments. Unfortunately, after perfusion of PFP over 6 pM tissue factor spots at a shear rate of 500 s^{-1} the whole chamber was filled with fibrin again and the thrombus could not be removed.

Secondly, both collagen and tissue factor were used to create micro-spots, as collagen is often used in perfusion experiments with PRP. Collagen and tissue factor were either mixed and applied simultaneously or collagen was applied first and after an hour of incubation in a humid atmosphere, tissue factor was added. PFP was perfused over the micro-spots at 500 s^{-1} and for both methods, the whole chamber was filled with a fibrin network and the thrombus could not be removed without damaging the structure. Instead of sticking to just the micro-spots, the fibrin network would also stick to the chamber itself. As fibrin is a sticky component, the sticking of fibrin to the chamber makes sense.

Thirdly, to prevent fibrin to adhere on sites other than the micro-spots, the coverslip and chamber were incubated in isotonic blocking buffer (NaCl 136 mM, KCl 2.7 mM, $MgCl_2$ 2 mM, HEPES 5 mM, BSA 1% and glucose 0.1%) for 30 minutes after application of collagen-TF spots. After perfusion of PFP no fibrin had adhered anywhere in the system. The blocking buffer prevented fibrin to adhere to the coverslip and chamber. Most of the fibrin formed was flushed out during perfusion and collected in the collection tube at the end of the flow chamber. At the walls of the chamber, some fibrin formation could be observed, while no fibrin formation was found in the orderly fashion of the micro-spots. Therefore, the blocking buffer effectively prevents fibrin adherence, though prevents adherence on the micro-spots as well.

Fourthly, as the blocking buffer blocked the entire coverslip, regions of the coverslip were covered with tape, to create blocker-free strips on the coverslip. This way part of the coverslip will be left untreated and on these unblocked surfaces micro-spots were applied. After 30 minutes of submerging the coverslip in blocking buffer, the tape was removed and collagen and tissue factor spots were applied. Unfortunately, during perfusion of PFP at 500 s^{-1} the fibrin completely occluded the chamber again.

To improve fibrin binding to the collagen micro-spots, PFP was mixed 9:1 with freshly drawn PRP. The platelets, activated and sticking to collagen, will improve fibrin adherence, as their receptors bind fibrin. This way the platelets, which adhere to the collagen, can hold the fibrin network in place. After collagen-TF micro-spot application the coverslip was blocked with a blocking buffer. Additionally, the flow chamber was blocked with a blocking buffer to prevent fibrin attachment in the chamber. As with the PFP experiments the PRP was recalcified before addition to the syringe, allowing the plasma to start clotting. During perfusion of the plasma contact activation in the syringe clotted the contents of the syringe. The occlusion of the syringe halted perfused and then the stationary plasma clotted the full system. Clot material was found in both the chamber and the tubing leading up to the syringe. To prevent contact activation in further experiments, calcium is no longer added to the plasma before perfusion. Instead, it's added to the plasma flow right before the plasma is added to the chamber (Figure A.3c). This will prevent contact activation inside the syringe as the plasma is still calcium deficient. When using three inlets, the plasma no longer clots in the syringe and perfusion experiments could be done. After blocking of the chamber and the collagen-TF spotted coverslip, PRP was perfused at a shear rate of 500 s^{-1}. After perfusion only very small patches of platelets and very little fibrin. Almost all the clot formed ended up in the collection tube and not on the micro-spots. As these experiments have shown to be successful by our colleagues in Maastricht, collagen staining was done to check whether the collagen micro-spots are formed properly. These experiments can be found in Section A.3.

Besides collagen spots with PRP perfusion, fibrinogen micro-spots with PFP perfusion was tried. The fibrinogen micro-spots on the surface of the coverslip would be an adhesive surface the fibrin can coagulate on. Fibrinogen labelled with Alexafluor 647 (0.025 mg/ml) was applied to coverslips salinized with aminopropyltriethoxysilane. Then PFP with fibrinogen labelled with Alexafluor 488 was perfused through the chamber. The two different coloured Alexafluors were used to be able to distinguish between the applied fibrinogen

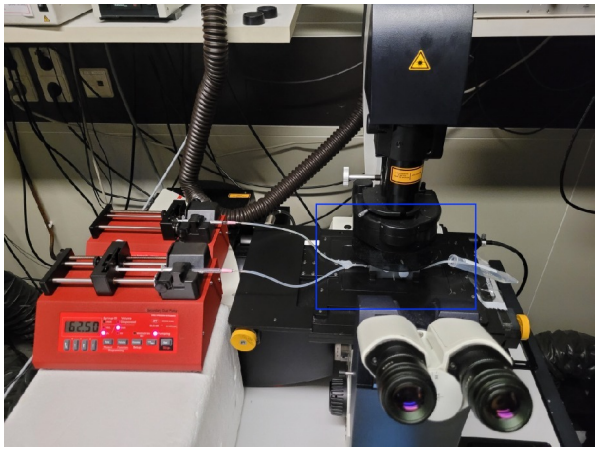

(a)

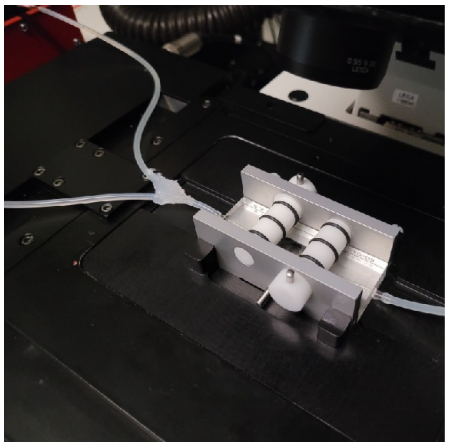

(b)

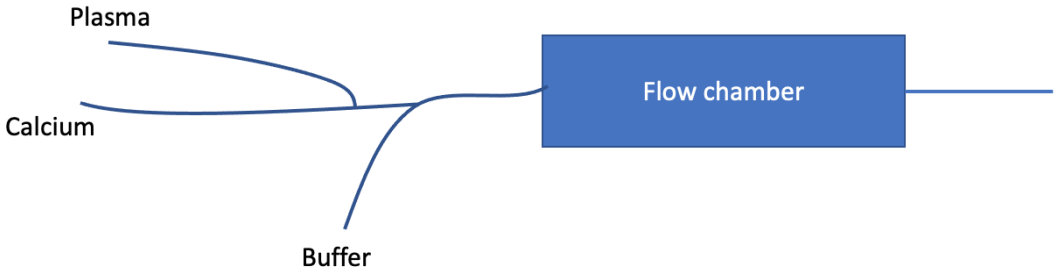

(c)

Figure A.3: a) The setup of the flow chamber. The two pumps were connected to the flow chamber, which was mounted on the microscope. At the end, a collection tube collected the fluid exiting the flow chamber. b) Close-up of the flow chamber mounted on the microscope. The inlet tubes were connected (one of the tubes was perforated and another tube was stuck on the hole to form a y-section) right before the entrance. The chamber was securely placed on the microscope lens, through which thrombus formation could be tracked. c) Schematic of the setup used for the flow chamber experiments with three inlets.

layer and plasma's fibrin. Right before entering the flow chamber the plasma was mixed with calcium and TF to obtain final concentrations of 17 mM and 5 pM, respectively. During the experiment the red fibrinogen (stained with 647) could only be found around the boundaries of the flow chamber, indicating that the fibrinogen is not stuck on the surface and does not function as an adhesive for thrombus formation.

Lastly, small fibrin micro-spots were made on the coverslip to function as a base for the fibrin formation. PFP was combined with 8 uL fibrinogen labelled Alexafluor 488 (0.025 mg/ml), Ca (17 nM) and TF (5 pM). Then micro-spots with fluid volumes of 1, 2, 4 and 6 μL were made. The micro-spots were incubated in a humid atmosphere for an hour. Some of the spots were directly used as micro-spots while other spots were transferred with a pipet and glued on another coverslip. The adherence of the spots was checked by perfusing buffer at increasing shear rates. The fibrin spots formed on the coverslip without glue were very loose and did not survive perfusion, while the glued spots firmly stayed in place. During imaging of the glued-on micro-spots, it was seen that the glue influences and disfigures the fibrin network and would not be a natural adhesion point for fibrin formation.

A.3. Preliminary experiments: Collagen staining

The microscopic coverslip on which the thrombogenic surface is deposited is very smooth. Therefore to ensure that the thrombogenic surface (i.e. collagen) adheres to the coverslip and stays adhered when exposed to various flow rates, staining protocols were done. Two staining protocols were tried: Martius Scarlet Blue (MSB) and Coomassie Brilliant Blue staining. For the former, the glasses were incubated at 56 °C in Bouin's fluid for an hour. After washing with demi-water the glasses were incubated in methyl blue for 5 minutes and then washed in 1% aqueous acetic acid. After staining the glasses only four glasses showed circular micro spots. The common factor between these slides was, that the tissue factor was applied either simultaneously with the collagen or after collagen incubation. All the coverslips subjected to flow did not show a micro spot pattern nor did the control group of collagen. The coverslips that did show micro-spots were further

investigated with a bright-field microscope. It was concluded that the collagen does not survive the washing steps in MSB staining, as the spots were more brown in colour than the expected blue for collagen and were not fiber-like in nature.

For the second staining with Coomassie Brilliant Blue, two groups of coverslips were prepared. The first group of coverslips were salinized with aminopropyltriethoxysylane prior to collagen application. Before salinization, the coverslips were washed in demi-water and ethanol and then submerged in a methanol hydrochloric acid (HCl) mixture (1:1) under continuous swerving for half an hour. After washing with demi-water and ethanol the coverslips were left to dry. Once dry collagen micro-spots were incubated on the coverslip at room temperature in a humid atmosphere for an hour. The other coverslips were decreased in 1 M HCl-ethanol mixture, rinsed with demi-water and dried overnight, before the collagen micro-spots were applied. After incubation, half the glasses were rinsed with saline. All the glasses were submerged in Coomassie dye for 20 minutes and then rinsed with HEPES buffer. After rinsing the glasses were inspected under the microscope and it was found that only very small amounts of the collagen stay adhered to the coverslip. Most of the collagen is already washed off when the coverslips are softly submerged in the dye. Therefore, the collagen does not stick to the surface of the coverslip and therefore the thrombi formed with PRP are not bound to the coverslip and cannot be taken out of the flow chamber

B

Appendix: Protocols

B.1. Chandler loop

1. Whole blood was spun at 2500g (acceleration 7) for 10 minutes.
2. Plasma layer was taken off and spun again at 2500g (acceleration 7) for 10 minutes.
3. Plasma layer is taken and used to form thrombi
4. Cut tubing, roughly 36.5 cm, so that they fit snugly around the rotating tube of the Chandler loop.
5. Cut small pieces of larger tubing, which will function as the latch between the two ends of the tubing.
6. Make sure you can easily mount and dismount the tubing before continuing with the experiment.
7. Add 964 μL PPP and 16 μL fibrinogen labelled Alexafluor 488 (0.025 mg/ml) in an eppendorf. If you want to spin multiple samples at the same time prepare the number of plasma samples before continuing with the next step.
8. Add 20 μL $CaCl_2$ (850 nM) to the eppendorf
9. Immediately transfer the contents of the Eppendorf (1000 μL) to a Chandler loop tube.
10. Repeat this for the number of tubes you want to make.
11. Start the Chandler loop at the required RPMs and let it spin for 60 minutes.
12. The thrombi are taken from the tubing (if one gets stuck use a plunger to softly push it out) and excess plasma is removed.
13. The thrombi are stored in HEPES buffer (pH 7.4) in the fridge (4 °C).

B.2. Preparing samples for SEM

Adapted from protocol made by J.J. De Vries, Hematology Department at the Erasmus Medical Centrum:

1. Rinse prepared samples with 1 ml cacodylate buffer (0.05M sodium cacodylate trihydrate, 0.2M HCl in dH20). Do this 3x 10 min on a shaker
2. Fix the sample in 1 ml of a 2% glutaraldehyde in cacodylate buffer mixture and shake for 2 hours at the shaker
3. Rinse samples with 1 ml cacodylate buffer, 3x 10 min on a shaker.
4. Start dehydration by adding 1 ml of the following mixtures per thrombus and shake the samples for the appropriate time:
    - 30% EtOH 10 min

- 50% EtOH “
- 70% EtOH 20 min. Can be left overnight at room temperature in a shaker.
- 80% EtOH “
- 90% EtOH “
- 95% EtOH “
- 100% EtOH 3 x 30 min

5. Incubate with hexamethyldisilazane (HDMS), without a shaker
   - Add 50% HMDS for 10 min (mix HDMS with EtOH 1:1)
   - Add 100% HMDS for 15 min
6. Open the lid and leave the thrombi in the fume hood overnight to allow the HDMS to evaporate.
7. Mount the sample on aluminium pin stubs with double-coated carbon tape. Make sure you stick it upside down, to prevent imaging the biofilm that forms during drying.
8. Sputter-coat with Au/Pd (80/20) to get a 15 nm layer.

B.3. Compression testing

Adapted from protocol made by R.C.H. Calahane (PhD), Cardiology Department at the Erasmus Medical Centrum:

1. Fill the water bath with HEPES buffer and warm the buffer to 37 °C
2. Connect the compression tester to the laptop and turn the laptop on.
3. Brush the formed bubbles away once the buffer is fully heated.
4. Cut the samples to 2 (10 and 30 RPM) and 1 mm (0 RPM) high disks
5. Photograph the surface area of the disk with a ruler in view, so that the surface area can be calculated with ImageJ later on.
6. Open the in advance written MEX file, which holds the compression protocol and write the data (PC -> Product).
7. Open Labview unconfined compression program and click run.
8. Tare the load cell.
9. Place the disk inside the water bath on the platform, which is positioned below the load cell.
10. Make an empty text file and select this as save location for the data.
11. Lower the load cell to the surface of the thrombus and wait for the load curve to flatten.
12. Start the compression test (make sure to use the 1 mm file for the 0 RPM thrombi and the 2 mm file for the 2 mm thrombi.)

B.4. Micro-indentation

1. Power up the system, by pressing the power buttons on the laptop, controller box and the OP1550 interferometer.
2. Start the Piuma Nanoindenter software on the laptop.
3. Mount the probe in the indentor head, always hold the plastic adapter and avoid touching the glass
4. Place the connector of the probe (green) in the sensor connector of the interferometer. Make sure you do not bend the will between the probe and connector, this will destroy the optical fiber.

5. Add the settings of the probe (stiffness and tip radius) in the Configure probe tab.
6. Submerge the probe in the medium you will do your experiment in.
7. On the interferometer go to quadrature menu and start scan.
8. If the quadrature scan was successful a sinusoid will show. If unsuccessfully a warning will pop up and you have to check the connection of the green connector to the interferometer.
9. Find the surface by pressing the "find surface" button.
10. When the surface is found the probe moves back 10 μm. Move the probe down 10 μm to make sure it is in contact with the surface.
11. When the probe is in contact with the surface press the "calibrate" button.
12. The software will measure a calibration factor which should be around the same value as the geo factor on the box of the probe.
13. Configure your indentation in the configure indentation menu. Fill in the displacement of the piezo and the time for the displacement for the indentation. Beware that if you use the find surface feature that your probe will start 10 μm above the sample.
14. Place your sample below the probe (make sure the probe cannot be damaged when placing your sample).
15. Find the surface of the sample with the "find surface" button or by manually observing the interferometer (i.e. a large step in the signal).
16. Wait 5 minutes (to make sure that there are no oscillatory vibrations in the probe).
17. Press "start indentation".

B.5. Thrombogenic surface preparation

Adapted from protocol made by C. Baaten and M. Nagdy, Clinical thrombosis and Haemostasis Department of Maastricht University.

1. Rinse the required number of coverslips in 1x 1M HCl-EtOH and 2x water and leave to dry overnight.
2. Spread 1 μL HORM Collagen (50 ug/mL) on the coverslips and incubate them in a humid atmosphere for 1 hour.
3. Rinse the coverslips with saline and let dry
4. Spread 1 μL TF (500 pM) on the collagen and incubate for 1 hour.
5. Rinse the coverslips with saline and keep them in HEPES buffer (pH 7.4) till use
6. Block the coverslips with blocking buffer (NaCl 136 mM, KCl 2.7 mM, MgCl2 2 mM, HEPES 5 mM, BSA 1% (1g per 100 ml) and glucose 0.1%, for 30 minutes
7. Wash the coverslips with saline and keep in HEPES buffer (pH 7.4) till use

B.6. Flow chamber assembly

1. Attach tubing to the inlet and the outlet of the flow chamber.
2. Place the flow chamber upside down and fill the inlet and duct with HEPES buffer (pH 7.4).
3. Place a coverslip on top of the flow chamber and softly remove excess buffer with a tissue.
4. Turn the flow chamber around, place it in the aluminium holder and tighten the screws.

5. Turn the holder around and check for air bubbles inside the duct. Tap the bubbles while softly adding some more buffer at the inlet.
6. Fill up the inlet construction (which has three tubes) with buffer.
7. Attach the syringe with $CaCl_2$ and with blood (or plasma) and push on the plunger till both are right before the y-section. Make sure they do not mix you our you start coagulation.
8. Place the chamber on the microscope, secure the syringes in the pumps and press start.

B.7. Static thrombus formation (on coverslips)

Adapted from protocol made by J.J. De Vries, Hematology Department at the Erasmus Medical Centrum:

1. Rinse the required number of coverslips in 1x 1M HCl-EtOH and 2x water and leave to dry overnight
2. Defrost and mix the PPP, to create a pooled stock.
3. Take 180 μL PPP and mix with 13.3 μL fibrinogen labelled Alexafluor 488 (0.025 mg/ml).
4. Add 0, 2 or 4 μL fibrinogen (5 g/L) to increase the fibrinogen levels in the samples.
5. Add 4 μL $CaCl_2$ (850 nM)
6. Add 2 μL thrombin (100 U/ml) and quickly pipet the plasma on the coverslip.
7. Incubate at humid atmosphere for an hour.
8. Store the thrombi in HEPES buffer (pH 7.4) and in the fridge (4 °C) till use.

C

Appendix: Preliminary experiments

C.1. Static thrombus formation and micro-indentation

Static thrombi on coverslips, superfrost slides and plastic petri-dishes were made to get familiar with and learn how to work with a micro-indenter. Furthermore, the measurements could be used as a baseline measurement for the flow chamber experiments. By adding 0, 2 and 4 μL 5 g/L fibrinogen to the plasma samples, thrombi with varying fibrinogen concentrations were created. After the addition of thrombin, the plasma was pipetted on a coverslip, superfrost slide or in a petri-dish. In less than half a minute the thrombi became opaque, but to make sure the thrombi were fully formed, they were incubated for an hour in a humid atmosphere. After an hour the thrombi were submerged in HEPES buffer and kept in the fridge till the next day.

The next day, multiple attempts of operating and obtaining measurements with the Piuma micro-indentor were done. The softer probe (0.20 N/m, 55 μm tip) was only able to test the tissue in air, while the stiffer probe (0.48 N/m, 104 μm tip) works in both air and a buffer solution. The softer probe did not calibrate properly in buffer and was therefore not usable in buffer. Moreover, the Piuma was situated on the 23rd floor of the EMC faculty tower, which induces some vibrations in the device. Found was that the Piuma worked better early in the morning or late in the afternoon when fewer people are present in the building. Sometimes during measurements, an odd sinusoid would disturb the signal and would only disappear after a waiting time of 30 to 60 minutes. Moreover, when the Piuma was facing the wall with the door, the noise in the signal was decreased. Finding the surface of the thrombus proved to be difficult, as often the measurement already starts inside the tissue. Out of 10 tries, only two measurements were deemed appropriate.

C.2. Chandler loop

Before the final experiments a set of preliminary experiments were done to find the best way of handling the samples and to determine which clotting factor to use. Found was that if the spinning of the Chandler loop was stopped, the thrombi would get stuck in the tubing and would no longer experience flow. Therefore, the tubes would have to be spun separately or there would need to be enough time before coagulation to fit multiple tubes on the loop. The addition of tissue factor triggers the coagulation cascade within 3 minutes, making it difficult to prepare multiple tubes and place them around the Chandler loop. Furthermore, as our interest is to form a fibrin network in the presence of flow, it was decided that activation with calcium would give the loop enough time to establish a flow in the tubes and make sure that the thrombus is formed in the presence of flow.

C.3. Difference between inclusion criteria for determining pore size

To filter out overlapping circles two inclusion and discarding methods were tested. The first was proposed by Molteni et al. while the other is a modification of said procedure [60]. For both procedures, the circles were sorted from largest to smallest and the largest circle in the list was accepted as the first included circle. Then the next circle in the sorted list (i.e large to small) would be compared to all circles in the included list and added to the included circle list (i.e will be growing with each addition) if the following criterion is true: if the centre of the smaller circle lies inside one of the larger circles of the included list the circles are

largely overlapping and the smaller circle is not included. This criterion is true when the distance between the centres of the circle is smaller than the maximum between the two circles' radii. This filtering method proposed by Molteni et al. filters out largely overlapping circles (Figure C.1a). The method greatly decreases the overlap of the circles, but cannot filter three or four circles that significantly overlap. Therefore, another filtering method was tested, which only includes the circle if the sum of both radii is larger than the distance between the two centres of the circles. This will ensure that there is no overlap between the circles (Figure C.1b). As shown in the graph the distribution and the fit of the data is similar and therefore either method would be appropriate. Finally, the inclusion and discarding method proposed by Molteni et al. was used.

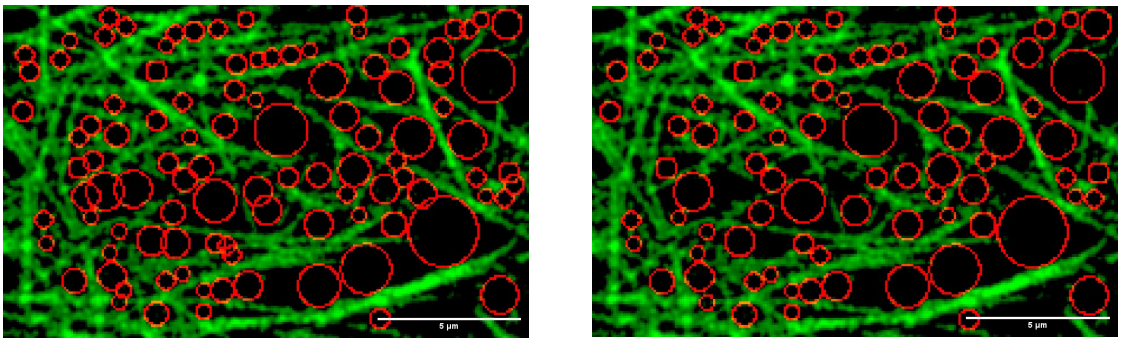

(a) (b)

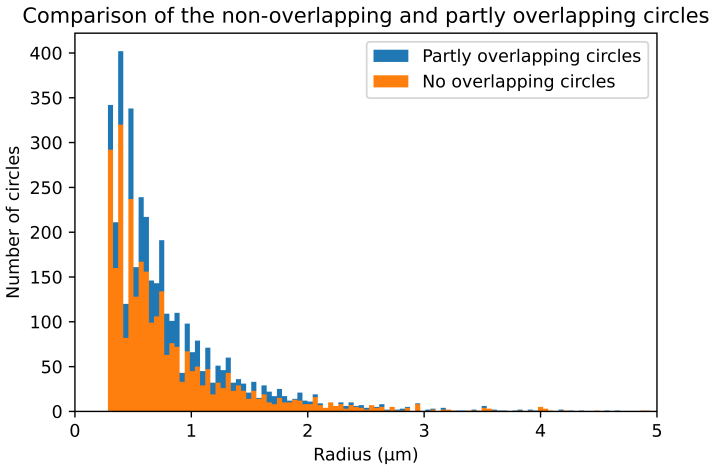

(c)

Figure C.1: a) Circles found in a fibrin network after the inclusion and discarding criterion from Molteni et al. [60]. The circles are allowed to overlap as long as the centres of the circles are outside of the other circle. This filtering process cannot filter three or four circles that are largely overlapping. b) Circles found in a fibrin network after the adapted inclusion and discarding criterion. Here circles are not allowed to overlap. Both images are a zoomed-in part of an image with a larger area. c) Comparison of the partly overlapping and not overlapping circles. The total number of circles found for both cases was 3985 for the partly overlapping circles and 2880 for the not overlapping circles.

D

Appendix: Codes

D.1. Compression testing (Matlab and Python)

Adopted from R.C.H. Calahane (PhD), Cardiology Department at the Erasmus Medical Centrum:

D.1.1. First loading curve

```
%written by Manouk Mondeel / Rachel Cahalane / Adapted by Hanneke Crielaard / Adapted by E.D. Hazekamp

%% 1. Load data and assign variables
%clear previous work
clc
clear all
close all;

saveFolder = 'D:\Thesis\Compression test matlab\0RPM';

T = readtable('D:\Thesis\Compression test matlab\0RPM\1.1.txt'); %load data from text file
timestamp = T{:,1};
force = T{:,2};

timeSec = seconds(timestamp - timestamp(1));
time = round(timeSec,3);

PlotFigures(time,force,'Time (s)','Force (N)',saveFolder)
%load("0RPM.mat")
%PlotFigures(xvar,yvar,labelx,labely,saveFolder)

%% 2. Crop data for first loading cycle
%% Select beginning and starting points from figure(1) using zoom and data points
PlotFigures(time,force,'Time (s)','Force (N)',saveFolder)

%% Find peaks endTime
[peakValues, indexes] = findpeaks(force, 'MinPeakHeight', 0.03);
tValues = time(indexes);
peak = tValues(1);

start = peak - 8;
%% Crop data
%select start of first loading curve and end of first loading curve
startTime = 0;
endTime = peak;
startIdx = find(time==[[startTime]]); %search for index of start point
endIdx = find(time==[[endTime]]); %search for index of end point
newtime =time(startIdx:endIdx)-time(startIdx); %zero the time
newforce = force(startIdx:endIdx)-force(startIdx); %zero the force

%% 3. Convert data
```

```
displacement=newtime.*(0.8/9); %time to displacement (where the compression test speed
    is 0.8/9 for 1 mm sample and 1.6/9 for 2 mm sample)
Strain=displacement./1; %displacement to strain using gauge length 2mm or 1 mm
Stress=newforce./(0.0004*0.0001); %Area of the clot in cm2
PlotFigures(Strain, Stress,'Strain','Stress (Pa)', saveFolder)

%% 4. Write all data to excel file
WriteToExcel('Strain', Strain ,'A','D:\Thesis\Compression test matlab\0RPM\
    First_loading_curve_1.1.xlsx');
WriteToExcel('Stress (Pa)', Stress ,'B','D:\Thesis\Compression test matlab\0RPM\
    First_loading_curve_1.1.xlsx');
```

D.1.2. Stiffness calculation

```
%written by Manouk Mondeel / Rachel Cahalane / Adapted by Hanneke Crielaard / Adapted
    by E.D. Hazekamp
% Read data
clc
clear all
close all;

T = readtable('D:\Thesis\Chiaro\30.2.2.xlsx', 'sheet', 'Blad1'); %load data from text
    file
%R = 103E-6; %this till line 19 was for the Chiaro, comment 20 and 21 and uncomment 8
    till 19 do stiffness caluclation for the Chiaro
%h = 15000E-9;
%a = sqrt((2*R*h) - (h*h));
%Area = pi * a * a;
%indent=T{:,3};
%[M,I] = max(indent);
%indent=T{1:I,3};
%load=T{1:I,2};
%stress=load/Area;
%stress= (3*(load/100000))/(2*pi*a*a);
%strain=-(indent-M)/M;

strain=T{:,1};
stress=T{:,2};
new_strain=rmmissing(strain);
new_stress=rmmissing(stress);

plot(new_strain,new_stress);

%% Limit to 0-40% Strain
startIdx = 1; %search for index of start point
%endIdx = 26; %search for index of end point

n=0.75; %find the index of the closest number to 10% strain
[val,idx]=min(abs(new_strain-n));
endIdx = idx;

lowstrain = new_strain(startIdx:endIdx);
lowstress = new_stress(startIdx:endIdx);

plot(lowstrain,lowstress);
xlabel('Strain')
ylabel('Stress')
legend({'Data'})
% Tools > Basic Fitting > Select linear fit > Record x slope and R2 value
% into 'Stiffness and Fit excel sheet'

%% Limit to 75-80% Strain
n=0.4; %find the index of the closest number to 10% strain
[val,idx]=min(abs(new_strain-n));
startIdx = idx;

%startIdx = 189; %search for index of start point
endIdx = length(new_strain); %search for index of end point

highstrain = new_strain(startIdx:endIdx);
```

```
highstress = new_stress(startIdx:endIdx);

plot(highstrain,highstress);
xlabel('Strain')
ylabel('Stress')
legend({'Data'})
% Tools > Basic Fitting > Select linear fit > Record x slope and R2 value
% into 'Stiffness and Fit excel sheet'
```

D.1.3. Hysteresis curves

```
%written by Manouk Mondeel / Rachel Cahalane / Adapted by Hanneke Crielaard

%% 1. Load data and assign variables
%clear previous work
clc
clear all
close all;

saveFolder = 'D:\Thesis\Compression test matlab\10RPM';

T = readtable('D:\Thesis\Compression test matlab\10RPM\1.1.txt'); %load data from text
    file
timestamp = T{:,1};
force = T{:,2};

timeSec = seconds(timestamp - timestamp(1));
time = round(timeSec,3);

PlotFigures(time,force,'Time (s)','Force (N)',saveFolder)
%PlotFigures(xvar,yvar,labelx,labely,saveFolder)

%% 2. Crop the data
% Select beginning and starting points from figure(1) using zoom and data points
startTime = 0;
endTime = 163.003000000000;
startIdx = find(time==[[startTime]]); %search for index of start point
endIdx = find(time==[[endTime]]); %search for index of end point
endIdx = 4076; %ik wil toch steeds hetzelfde eindpunt voor alle metingen
newtime=time(startIdx:endIdx)-time(startIdx); %zero the time
newforce= force(startIdx:endIdx)-force(startIdx); %zero the force
Stress=newforce./(0.0568*0.0001); %Area of the clot in cm2
PlotFigures(newtime,Stress,'Time (s)','Stress (Pa)',saveFolder)
%PlotFigures(xvar,yvar,labelx,labely,saveFolder)
% Save stress-time image

%% 3. Plot hysteresis curves (10 cycles)

[pks,locs]=findpeaks(Stress,'MinPeakProminence', 5500);%identify stress peaks above a
    value

    def1=0:(80/(locs(1,1)-1)):80-(80/(locs(1,1)-1));
    def2=[80:-(80/((locs(2,1)-locs(1,1)-1)/2)):0,0:(80/((locs(2,1)-locs(1,1)-1)/2))
    :80-(80/((locs(2,1)-locs(1,1)-1)/2))];
    def3=[80:-(80/((locs(3,1)-locs(2,1))/2)):0,0:(80/((locs(3,1)-locs(2,1)-1)/2))
    :80-(80/((locs(3,1)-locs(2,1)-1)/2))];
    def4=[80:-(80/((locs(4,1)-locs(3,1))/2)):0,0:(80/((locs(4,1)-locs(3,1)-1)/2))
    :80-(80/((locs(4,1)-locs(3,1)-1)/2))];
    def5=[80:-(80/((locs(5,1)-locs(4,1))/2)):0,0:(80/((locs(5,1)-locs(4,1)-1)/2))
    :80-(80/((locs(5,1)-locs(4,1)-1)/2))];
    def6=[80:-(80/((locs(6,1)-locs(5,1))/2)):0,0:(80/((locs(6,1)-locs(5,1)-1)/2))
    :80-(80/((locs(6,1)-locs(5,1)-1)/2))];
    def7=[80:-(80/((locs(7,1)-locs(6,1))/2)):0,0:(80/((locs(7,1)-locs(6,1)-1)/2))
    :80-(80/((locs(7,1)-locs(6,1)-1)/2))];
    def8=[80:-(80/((locs(8,1)-locs(7,1))/2)):0,0:(80/((locs(8,1)-locs(7,1)-1)/2))
    :80-(80/((locs(8,1)-locs(7,1)-1)/2))];
    def9=[80:-(80/((locs(9,1)-locs(8,1))/2)):0,0:(80/((locs(9,1)-locs(8,1)-1)/2))
    :80-(80/((locs(9,1)-locs(8,1)-1)/2))];
    def10=[80:-(80/((locs(10,1)-locs(9,1))/2)):0,0:(80/((locs(10,1)-locs(9,1)-1)/2))
    :80-(80/((locs(10,1)-locs(9,1)-1)/2))];
```

```
    def11=80:-(80/((locs(10,1)-locs(9,1)-1)/2)):0;
    deformation=[def1,def2,def3,def4,def5,def6,def7,def8,def9,def10,def11]';

    %% delete final zero value from deformation vector
    % double click on 'deformation', delete last 0 row in the 4028 line,
    % run section

    stressstrain=[deformation, Stress(1:(length(deformation)))];
    PlotFigures(stressstrain(:,1), stressstrain(:,2), 'Strain (%)', 'Stress (Pa)',
    saveFolder)

% Save hysteresis curve image

%% 5. Write all stress-time data to excel file
WriteToExcel('time (s)', newtime ,'A','D:\Thesis\Compression test matlab\10RPM\
    hysterisis_1.1.xlsx');
WriteToExcel('stress (Pa)', Stress ,'B','D:\Thesis\Compression test matlab\10RPM\
    hysterisis_1.1.xlsx');
writematrix(deformation,'hysterisis_def_1.1.csv')
```

D.1.4. Viscous energy from the hysteresis curves

```
"""
@author: E.D. Hazekamp
"""

import csv
import numpy as np
from matplotlib import pyplot as plt
import scipy.integrate
import scipy.optimize
import math

Energy2 =[ ]

cycles = np.linspace(0,9,10)
j = ['1','2']
k = ['1','2','3','4']

bestand = np.genfromtxt(r'D:\Thesis\Compression test matlab\0RPM\hysterisis_1.1.csv',
    delimiter=",")
Strain = (bestand[1:,2]) #for all 0RPM samples
Strain = np.multiply(Strain,100)

for l in k:
    for i in j:
        bestand = np.genfromtxt(r'D:\Thesis\Compression test matlab\0RPM\hysterisis_'+
    l + '.'+ i +'.csv', delimiter=",")
        Time = (bestand[1:,0])
        Stress = (bestand[1:,1])
        bestand = np.genfromtxt(r'D:\Thesis\Compression test matlab\0RPM\
    hysterisis_def_'+ l + '.'+ i +'.csv', delimiter=",")
        Strain = (bestand[0:])

        Energy =[]

        begin = 0
        x = np.where(Strain == 0)
        begin = x[0]
        old = 0
        for m in begin:
            diff = m - old
            old = m
            if diff == 1:
                f = np.where(begin == m)
                begin = np.delete(begin, f)

        x = np.where(Strain == 80)
        half = x[0]

```

```
46
47          for g in cycles:
48              maxload = half[int(g)]
49              start = begin[int(g)]
50
51              plt.plot(Strain[start:maxload],Stress[start:maxload],c='blue')
52              end = begin[int(g+1)]
53              plt.plot(Strain[maxload:end],Stress[maxload:end],c='red')
54              plt.show()
55              Area1 = scipy.integrate.cumulative_trapezoid(Stress[start:maxload],Strain[
    start:maxload])
56              Area2 = scipy.integrate.cumulative_trapezoid(Stress[maxload:end],Strain[
    maxload:end])
57              Area = sum(Area1) - sum(Area2)
58              Energy = np.append(Energy,Area)
59
60          Energy2 = np.append(Energy2,[Energy])
61          plt.show()
62
63  with open(r'D:\Thesis\Compression test matlab\0RPM\Energy.csv', 'w', encoding='UTF8')
        as f:
64      writer = csv.writer(f)
65      writer.writerow(Energy2)
66
67  Energy2 = []
68  print('finished 0 RPM')
69
70  for l in k:
71      for i in j:
72          bestand = np.genfromtxt(r'D:\Thesis\Compression test matlab\10RPM\hysterisis_'+
     l + '.'+ i +'.csv', delimiter=",")
73          Time = (bestand[1:,0])
74          Stress = (bestand[1:,1])
75          bestand = np.genfromtxt(r'D:\Thesis\Compression test matlab\10RPM\
    hysterisis_def_'+ l + '.'+ i +'.csv', delimiter=",")
76          Strain = (bestand[0:])
77
78          Energy =[]
79
80          begin = 0
81          x = np.where(Strain == 0)
82          begin = x[0]
83          old = 0
84          for m in begin:
85              diff = m - old
86              old = m
87              if diff == 1:
88                  f = np.where(begin == m)
89                  begin = np.delete(begin, f)
90
91          x = np.where(Strain == 80)
92          half = x[0]
93
94          for g in cycles:
95              maxload = half[int(g)]
96              start = begin[int(g)]
97              plt.plot(Strain[start:maxload],Stress[start:maxload],c='blue')
98              end = begin[int(g+1)]
99              plt.plot(Strain[maxload:end],Stress[maxload:end],c='red')
100             plt.show()
101             Area1 = scipy.integrate.cumulative_trapezoid(Stress[start:maxload],Strain[
    start:maxload])
102             Area2 = scipy.integrate.cumulative_trapezoid(Stress[maxload:end],Strain[
    maxload:end])
103             Area = sum(Area1) - sum(Area2)
104             Energy = np.append(Energy,Area)
105
106         Energy2 = np.append(Energy2,[Energy])
107         plt.show()
108
109 with open(r'D:\Thesis\Compression test matlab\10RPM\Energy.csv', 'w', encoding='UTF8')
```

```
    as f:
    writer = csv.writer(f)
    writer.writerow(Energy2)

Energy2 = []
print('finished 10 RPM')

for l in k:
    for i in j:
        bestand = np.genfromtxt(r'D:\Thesis\Compression test matlab\30RPM\hysterisis_'+
 l + '.'+ i +'.csv', delimiter=",")
        Time = (bestand[1:,0])
        Stress = (bestand[1:,1])
        bestand = np.genfromtxt(r'D:\Thesis\Compression test matlab\30RPM\
    hysterisis_def_'+ l + '.'+ i +'.csv', delimiter=",")
        Strain = (bestand[0:])

        Energy =[]

        begin = 0
        x = np.where(Strain == 0)
        begin = x[0]
        old = 0
        for m in begin:
            diff = m - old
            old = m
            if diff == 1:
                f = np.where(begin == m)
                begin = np.delete(begin, f)

        x = np.where(Strain == 80)
        half = x[0]

        for g in cycles:
            maxload = half[int(g)]
            start = begin[int(g)]

            plt.plot(Strain[start:maxload],Stress[start:maxload],c='blue')
            end = begin[int(g+1)]
            plt.plot(Strain[maxload:end],Stress[maxload:end],c='red')
            plt.show()
            Area1 = scipy.integrate.cumulative_trapezoid(Stress[start:maxload],Strain[
    start:maxload])
            Area2 = scipy.integrate.cumulative_trapezoid(Stress[maxload:end],Strain[
    maxload:end])
            Area = sum(Area1) - sum(Area2)
            Energy = np.append(Energy,Area)

        Energy2 = np.append(Energy2,[Energy])
        plt.show()

with open(r'D:\Thesis\Compression test matlab\30RPM\Energy.csv', 'w', encoding='UTF8')
    as f:
    writer = csv.writer(f)
    writer.writerow(Energy2)
```

D.2. Fibrin surface area coverage (ImageJ)

Adapted from the macro made by J.J. De Vries, Hematology Department at the Erasmus Medical Centrum:

```
//@author: E.D. Hazekamp

open("D:/Thesis/04-01-22/04-01-22-100s-4.lif");
stacklist = getList("image.titles");
Array.print(stacklist);

for (i=0;i<stacklist.length;i++){
  selectWindow(stacklist[i]);
  run("Duplicate...", "duplicate");
  rename("pre" + i);
```

```
  run("Duplicate...", "duplicate");
  run("Gaussian Blur...", "sigma=2 stack");
  setAutoThreshold("Default dark");
  //run("Threshold...");
  setAutoThreshold("Otsu dark");
  //run("Threshold...");
  setOption("BlackBackground", false);
  run("Convert to Mask", "method=Default background=Dark calculate");
  imageCalculator("AND create stack", "pre" + i,"pre" + i + "-1");
  selectWindow("Result of pre" + i);
  setAutoThreshold("Default dark");
  //run("Threshold...");
  setThreshold(5, 255);
  setThreshold(5, 255);
  run("Set Measurements...", "area mean standard min centroid stack redirect=None
    decimal=3");
  run("Analyze Particles...", "size=5-Infinity pixel display clear summarize stack");
  selectWindow("Summary of Result of pre" + i);
  saveAs("Results", "D:/Thesis/04-01-22/100s-4-image" + i + 1 +"/density_and_intensity.
    csv");
  close("density_and_intensity");
  close("pre" + i);
  close("pre" + i + "-1");
  close(stacklist[i]);
}

stacklist = getList("image.titles");
Array.print(stacklist);

for(i=0;i<stacklist.length;i++){
  selectWindow(stacklist[i]);
  run("Gaussian Blur...", "sigma=2 stack");
  run("Enhance Contrast", "saturated=0.35");
  run("Apply LUT", "stack");
  nummer = i+1;
  run("Stack to Images");
  imagelist = getList("image.titles");
  Array.print(imagelist);
  imagelist = Array.slice(imagelist,stacklist.length - nummer,imagelist.length);
  Array.print(imagelist);
  for (j=0;j<imagelist.length;j++) {
        selectWindow(imagelist[j]);
        title = j+1;
        if (title <10) {
          title = "0" + title;
          saveAs(".jpg", "D:/Thesis/04-01-22/100s-4-image" + nummer + "/"  + title);
          }
        else {saveAs(".jpg", "D:/Thesis/04-01-22/100s-4-image" + nummer + "/"  + title)
    ;
        }
  close(imagelist[j]);
  }
}
//close("*");
```

D.3. Bubble analysis (Matlab)

```
%@author: E.D. Hazekamp

directories = { 'D:\Thesis\04-01-22\100s-4-image1' 'D:\Thesis\04-01-22\100s-4-image2'};
     %fill in directories
for b = 1:length(directories)
    directory = directories{b}; %present directory
    commafiles = dir(directory); %list with files in directory
    files = {commafiles.name}.'; %only the names of the files
    count = 0; %starts at 0, to keep track of number of times to go through the loop
    allradii = zeros(4096,length(files)); %create a matrix of zeros large enough to fit
     radius data
    R = 1:length(files); %first row has numbers of images
```

```
    allradii(1,:) = R; %insert first row in the matrix
    tic %start tracking time
    for  a = 1:length(files)
        if contains(files(a),".jpg")
            I = imread(append(directory,"\", files(a)));
            Igray = rgb2gray(I); %Convert the image into grayscale
            BW = imbinarize(Igray);
            %figure
            %imshowpair(I,BW,'montage'); %Display the original image next to the binary
     version.

            %bubbele calculation
            [bubble_radii, bubble_coord]=find_bubbles(BW);

            %extracting the right size of the image
            s = size(BW);
            xsize = s(1,1); % length of the image (number of rows)
            ysize = s(1,2); % width of the image (number of colums)

            %removing all bubbles that are party outside the image for x
            number = 0; %tracking how many loops have been made
            for j =1:length(bubble_coord)
                j = j - number; %adjust j for when values are removed in the matrix
                if j > length(bubble_coord)
                    break; %stop the loop when all data points have been evaluated
                end
                X1 = bubble_coord(j,1) - bubble_radii(j); % x coordinate of the
    leftmost pixel in the bubble
                X2 = bubble_coord(j,1) + bubble_radii(j); % x coordinate of the
    rightmost pixel in the bubble
                if  X1 < 1 %remove bubble when outside the left boundary of the image
                    bubble_coord(j,:) = [];
                    bubble_radii(j) = [];
                    number = number + 1; % if a value is removed the next loop needs to
     check the same j, all values move up a space
                elseif X2 > xsize %remove bubble when outside the right boundary of the
     image
                    bubble_coord(j,:) = [];
                    bubble_radii(j) = [];
                    number = number + 1; % if a value is removed the next loop needs to
     start at the same j, all values move up a space
                end

            end

            %removing all bubbles that are party outside the image for x,
            %same process as for x
            number = 0;
            for i =1:length(bubble_coord)
                i = i - number;
                if i > length(bubble_coord)
                    break;
                end
                Y1 = bubble_coord(i,2) - bubble_radii(i);
                Y2 = bubble_coord(i,2) + bubble_radii(i);
                if  Y1 < 1
                    bubble_coord(i,:) = [];
                    bubble_radii(i) = [];
                    number = number + 1;
                elseif Y2 > ysize
                    bubble_coord(i,:) = [];
                    bubble_radii(i) = [];
                    number = number + 1;
                end

            end

            %removing overlapping bubbles
            combined = [bubble_radii, bubble_coord]; %combine the data
            sorted = sortrows(combined,"descend"); %sort the data from large radius to
    small
```

```
75              included = sorted(1,:); %add the first radius
76              centerdist = norm(included(1,2:3) - sorted(2,2:3)); %find distance between
    two bubble centre points
77              for n = 2:length(sorted)
78                  if sorted(n,1) < 2 %%in case you want to remove small bubbles
79                      break;
80                  end
81                  for o = 1:length(included)
82                      s = size(included);
83                      centerdist = norm(included(o,2:3) - sorted(n,2:3));
84                      %maximum = max(included(o,1),sorted(n,1)); %largely overlapping
    bubbles are removed
85                      maximum = included(o,1) + sorted(n,1); %all overlapping bubbles are
     removed
86                      if centerdist < maximum %bubble is not included
87                          break;
88                      end
89                      if o == s(1,1) %new bubble is not overlapping any already included
    bubbles and can be included
90                          break;
91                      end
92                  end
93                  if centerdist > maximum %adding of the bubble to the list
94                          p = s(1,1) + 1;
95                          included(p,:) = sorted(n,:);
96                  end
97              end
98
99              % Making circles in the original images, for checking purposes
100             for p = 1:length(included)
101                 xCenter = included(p,3); %width of the image
102                 yCenter = included(p,2);
103                 radius = included(p,1);
104                 theta = linspace(0, 2*pi, round(4 * pi * radius)); % Define angles
105                 % Get x and y vectors for each point along the circumference.
106                 x = radius * cos(theta) + xCenter;
107                 y = radius * sin(theta) + yCenter;
108
109                 % Write those (x,y) into the image with level 255.
110                 for k = 1 : length(x)
111                     row = round(y(k));
112                     col = round(x(k));
113                     I(row, col) = 255;
114                  end
115              end
116
117             %create the control image
118              figure
119              imshow(I);
120              no = string(a - count); %number of image as text
121              saveas(gca,fullfile(directory + "/Bubble",no),'png'); %save the image to a
    bubble map inside the directory where the images came from
122              close
123              disp(string(strcat('Calculating done! It took ',num2str(toc),' seconds')))
    %how long it took to make the bubble image
124              no = a - count; %number of image
125              allradii(2:length(included)+1,no) = included(:,1); %put the included radii
    in the previously made zeroes matrix
126          else count = count + 1; %keep track of the loop
127          end
128     end
129     writematrix(allradii,fullfile(directory + "/Bubble","radius.csv")) %save all the
    radii to csv in bubble map
130 end
```

E

Appendix: Additional data on Image analysis

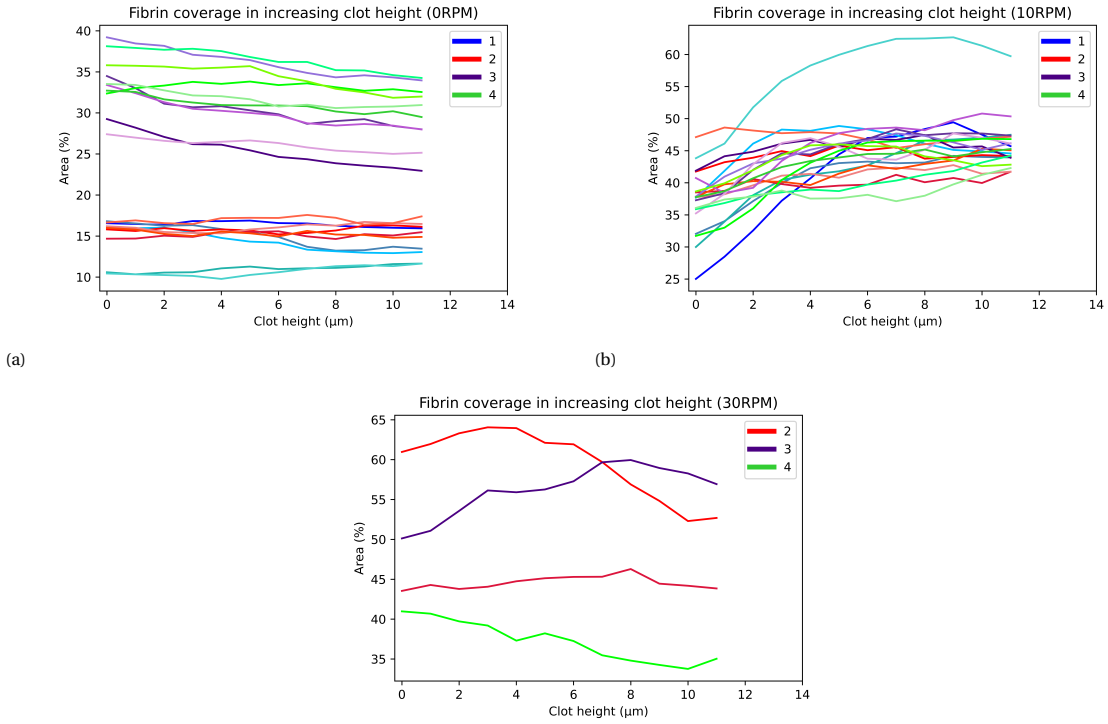

Figure E.1: The surface area coverage of the fibrin fibers through the first 11 μm of the thrombi. The 0 RPM (a) and 10 RPM (b) both have 4 samples, which stacks have been displayed in a different shade of the same colour. The 30 RPM only has 4 stacks in total, of which only thrombus number 2 had two stacks made.

F

Appendix: Additional data on compression testing

F.1. Stiffness fit

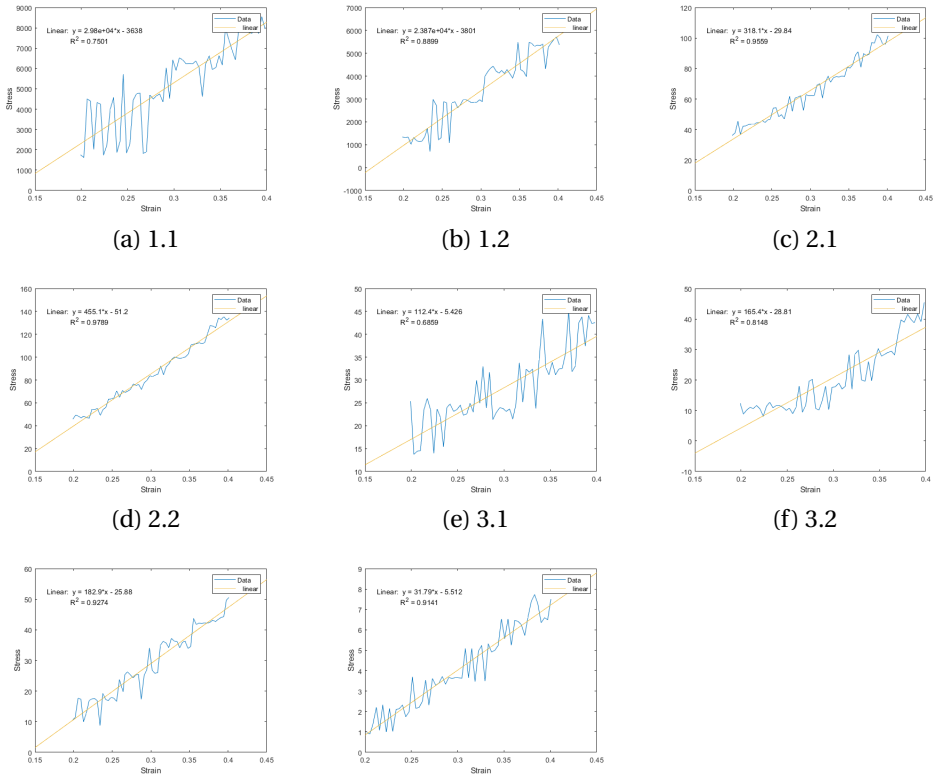

(a) 1.1 (b) 1.2 (c) 2.1

(d) 2.2 (e) 3.1 (f) 3.2

(g) 4.1 (h) 4.2

Figure F.1: Linear fit of the first loading curve of the 0 RPM samples, which was used to extract the tangent modulus. All images are 20-40 % strain. Two disks of four thrombus samples were compressed and named accordingly.

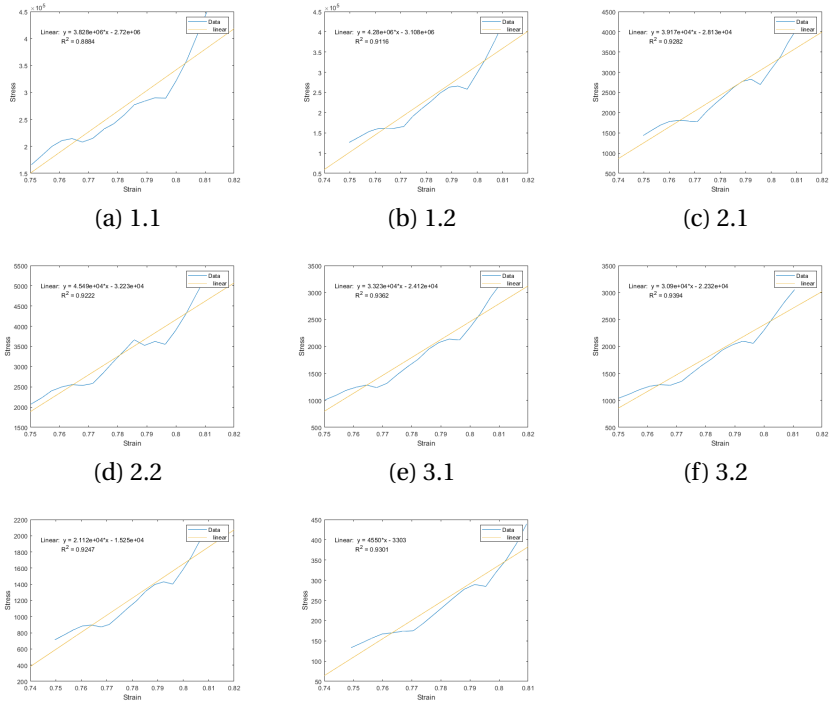

(a) 1.1 (b) 1.2 (c) 2.1

(d) 2.2 (e) 3.1 (f) 3.2

(g) 4.1 (h) 4.2

Figure F.2: Linear fit of the first loading curve of the 0 RPM samples, which was used to extract the tangent modulus. All images are 75-80 % strain. Two disks of four thrombus samples were compressed and named accordingly.

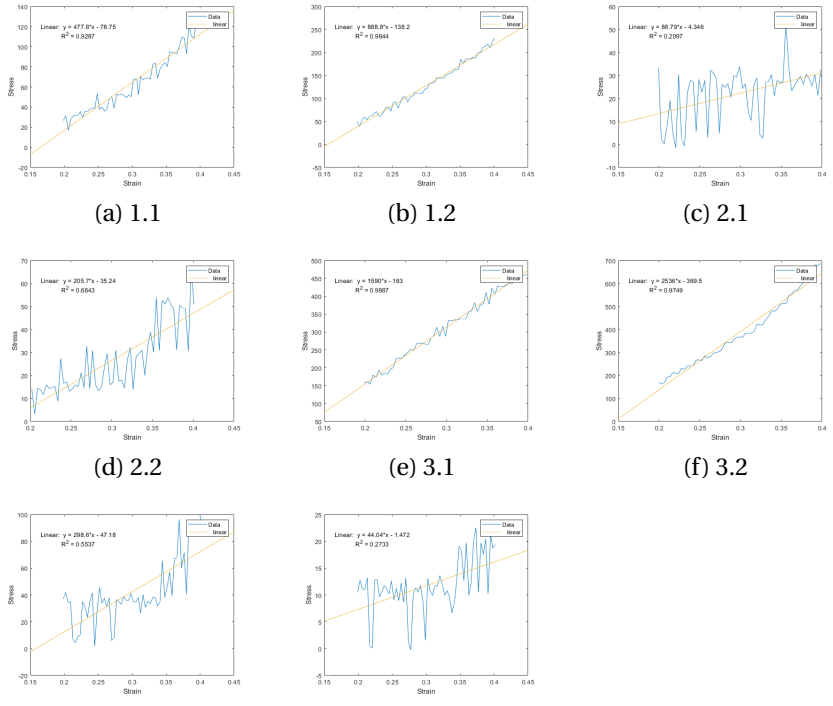

(a) 1.1 (b) 1.2 (c) 2.1

(d) 2.2 (e) 3.1 (f) 3.2

(g) 4.1 (h) 4.2

Figure F.3: Linear fit of the first loading curve of the 10 RPM samples, which was used to extract the tangent modulus. All images are 20-40 % strain. Two disks of four thrombus samples were compressed and named accordingly.

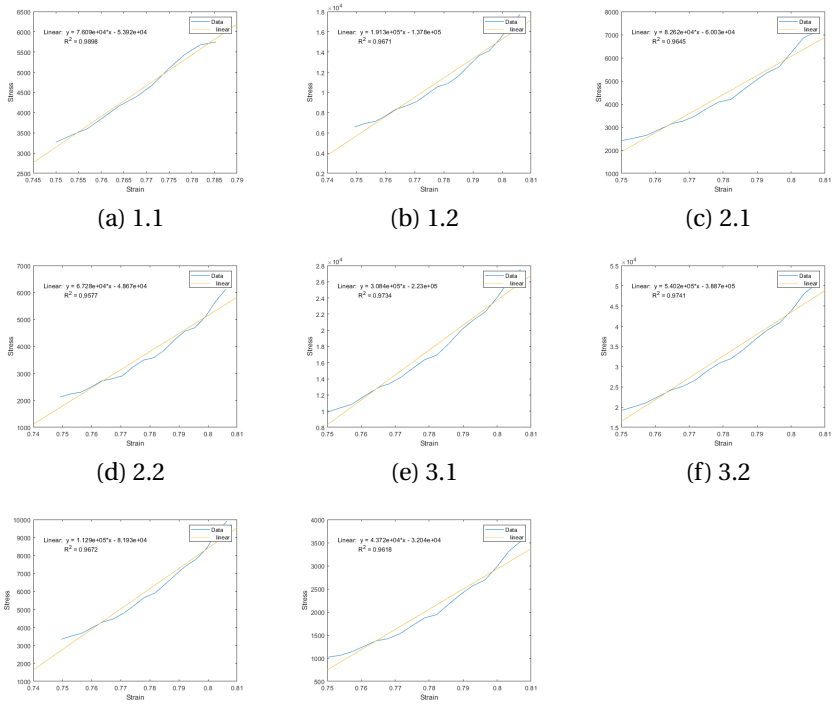

(a) 1.1 (b) 1.2 (c) 2.1

(d) 2.2 (e) 3.1 (f) 3.2

(g) 4.1 (h) 4.2

Figure F.4: Linear fit of the first loading curve of the 10 RPM samples, which was used to extract the tangent modulus. All images are 75-80 % strain. Two disks of four thrombus samples were compressed and named accordingly.

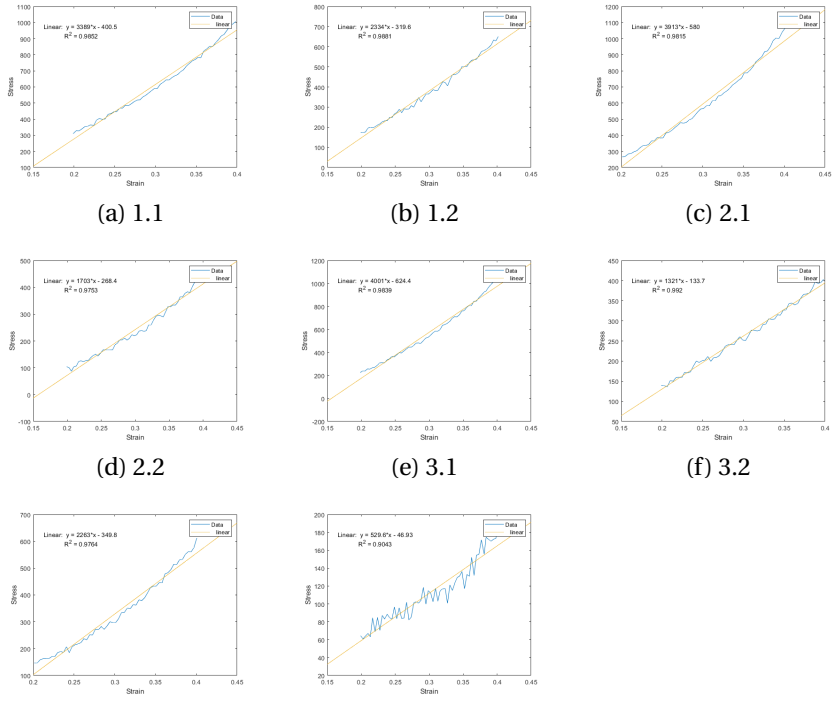

(a) 1.1 (b) 1.2 (c) 2.1

(d) 2.2 (e) 3.1 (f) 3.2

(g) 4.1 (h) 4.2

Figure F.5: Linear fit of the first loading curve of the 30 RPM samples, which was used to extract the tangent modulus. All images are 20-40 % strain. Two disks of four thrombus samples were compressed and named accordingly.

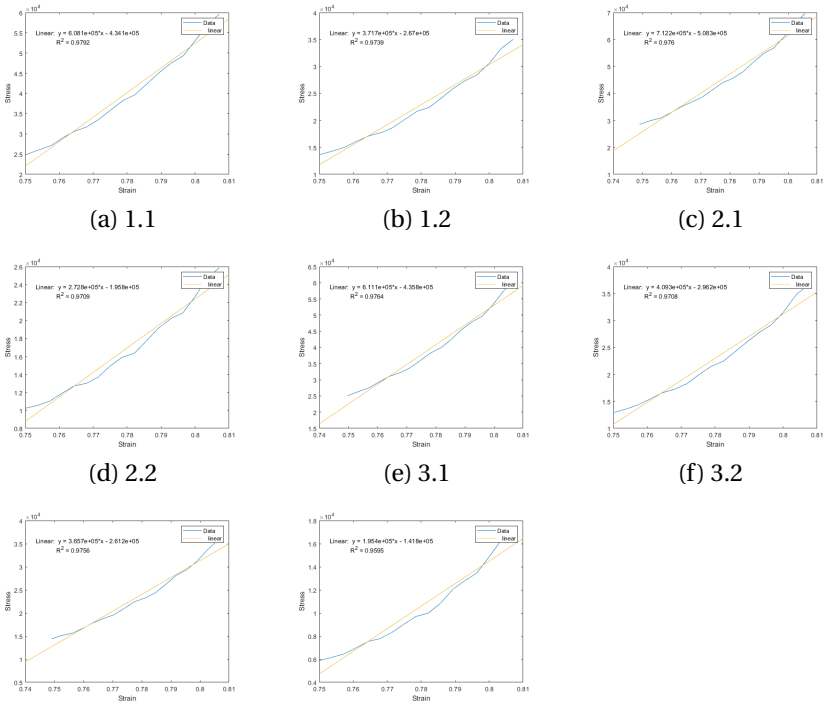

(a) 1.1 (b) 1.2 (c) 2.1

(d) 2.2 (e) 3.1 (f) 3.2

(g) 4.1 (h) 4.2

Figure F.6: Linear fit of the first loading curve of the 30 RPM samples, which was used to extract the tangent modulus. All images are 75-80 % strain. Two disks of four thrombus samples were compressed and named accordingly.

F.2. Hysteresis curves

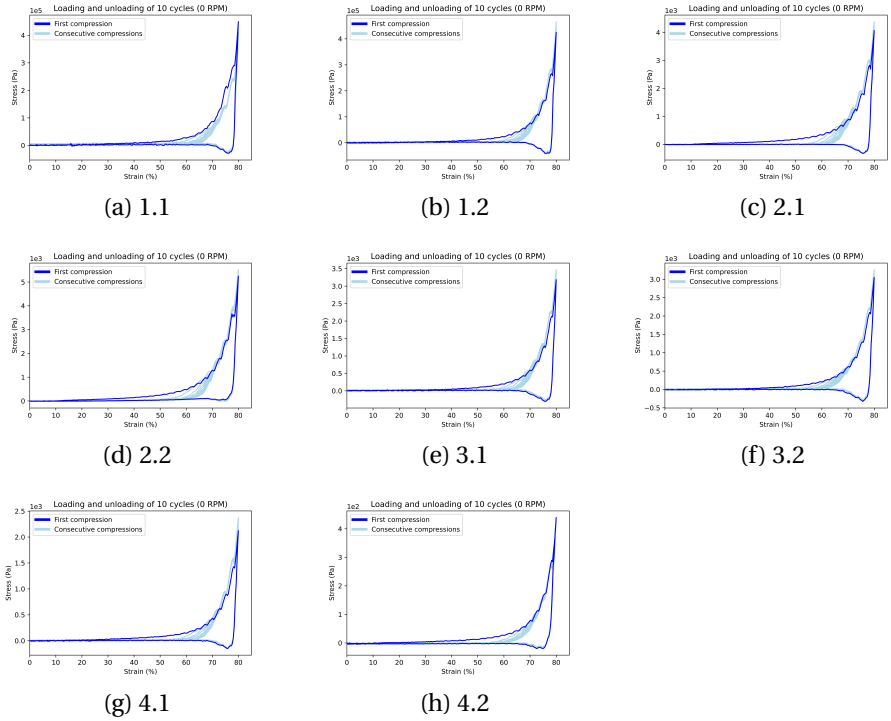

(a) 1.1 (b) 1.2 (c) 2.1

(d) 2.2 (e) 3.1 (f) 3.2

(g) 4.1 (h) 4.2

Figure F.7: Loading and unloading curves of the 0 RPM chandler loop clots. The pieces were cut to 1 mm and compressed 80% for 10 cycles. Two disks of four thrombus samples were compressed and named accordingly.

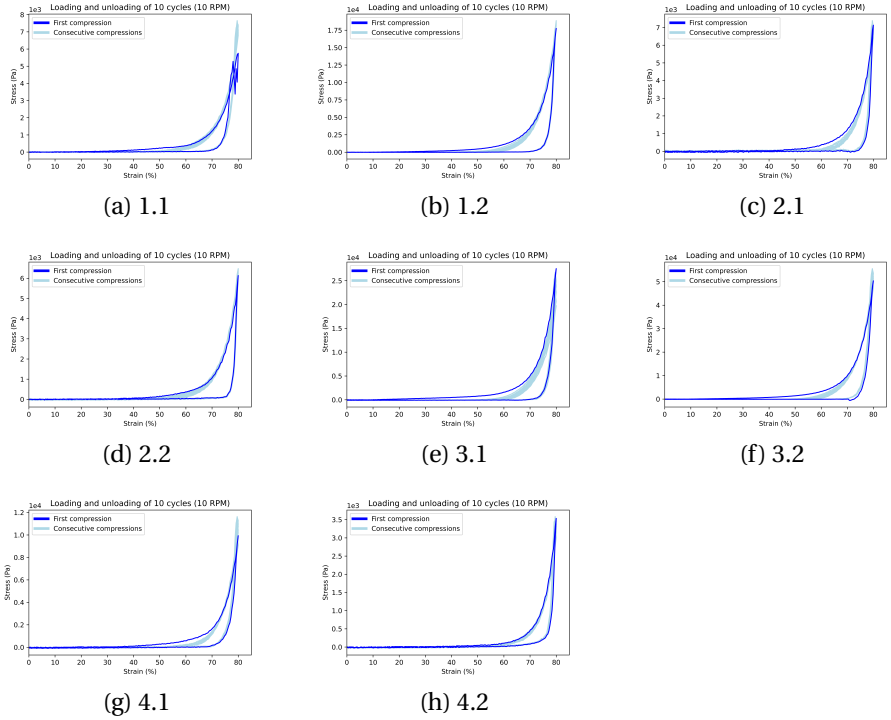

(a) 1.1 (b) 1.2 (c) 2.1

(d) 2.2 (e) 3.1 (f) 3.2

(g) 4.1 (h) 4.2

Figure E.8: Loading and unloading curves of the 10 RPM chandler loop clots. The pieces were cut to 1 mm and compressed 80% for 10 cycles. Two disks of four thrombus samples were compressed and named accordingly.

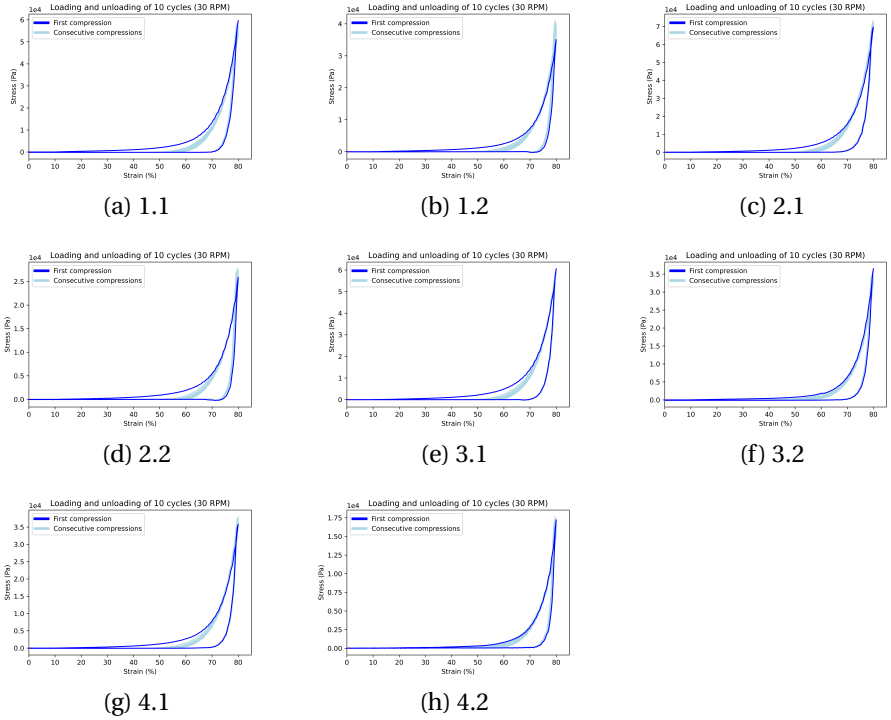

(a) 1.1 (b) 1.2 (c) 2.1

(d) 2.2 (e) 3.1 (f) 3.2

(g) 4.1 (h) 4.2

Figure E.9: Loading and unloading curves of the 30 RPM chandler loop clots. The pieces were cut to 1 mm and compressed 80% for 10 cycles. Two disks of four thrombus samples were compressed and named accordingly.

F.3. Hysteresis energy dissipation

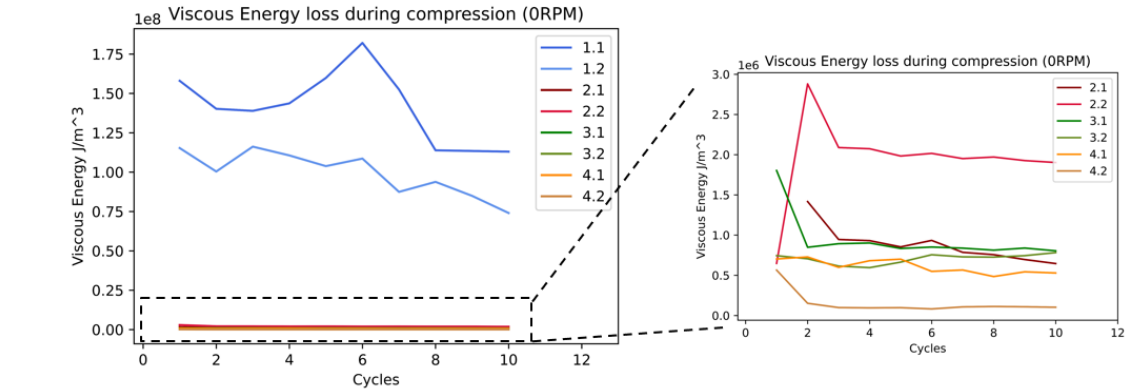

(a)

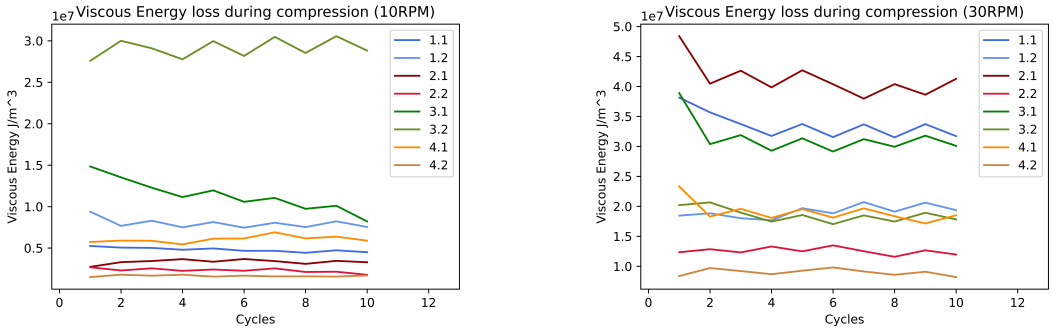

(b) (c)

Figure F.10: Viscous energy dissipation for 10 consecutive compression cycles. a) 0 RPM, b) 10 RPM and c) 30 RPM.

F.4. Chiaro

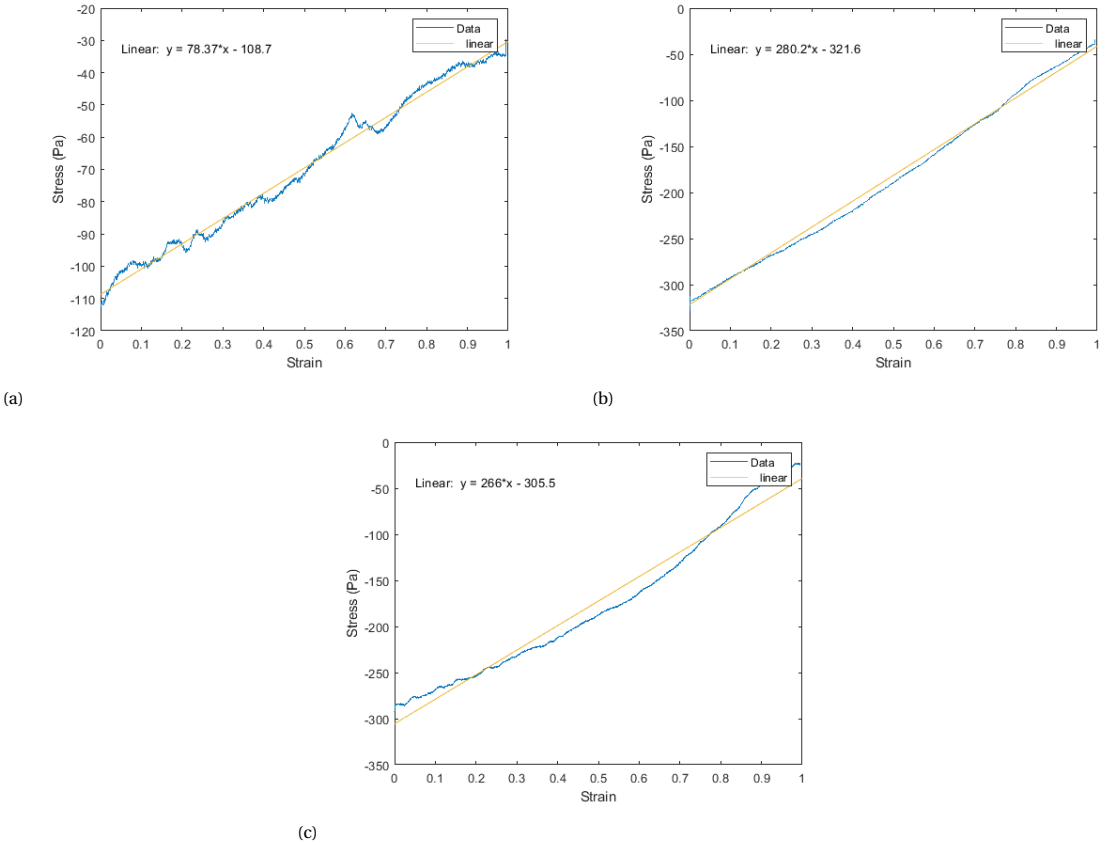

Figure F.11: Linear fit of the loading curve of the micro-indentation. a) 30.1.1, b) 30.2.1, c) 30.2.2.